ABSTRACT

Title of Document: PETROGENESIS OF PERALUMINOUS GRANITES FROM THE FOSDICK MOUNTAINS, MARIE BYRD LAND, WEST ANTARCTICA

Caitlin R. Brown, Master of Science, 2013

Directed By: Professor Michael Brown, Geology

Granites from the Fosdick Mountains, West Antarctica were analyzed for major and trace elements as well as Sr–Nd isotopes ratios in order to investigate the sources and processes associated with granite formation at a former convergent margin. U–Pb ages from zircon separates are consistent with previous results and yield ages of ~360 Ma and ~100Ma. Major and trace elements indicate that paragneiss and orthogneiss samples are the high-grade equivalents of the Swanson Formation and the Ford Granodiorite site. Granites produced from the Devonian–Carboniferous melting event are derived primarily from the Ford Granodiorite suite while granites produced from the Cretaceous melting event are derived from melting of the Ford Granodiorite suite or mixing between the two putative sources. Cretaceous granites show evidence of early crystallized minerals. There is no chemical evidence for a source other than the Ford Granodiorite suite or the Swanson Formation.

PETROGENESIS OF PERALUMINOUS GRANITES FROM THE FOSDICK MOUNTAINS, MARIE BYRD LAND, WEST ANTARCTICA

By

Caitlin R. Brown

Thesis submitted to the Faculty of the Graduate School of the
University of Maryland, College Park, in partial fulfillment
of the requirements for the degree of
Master of Science
2013

Advisory Committee:
Professor Michael Brown, Chair
Professor Richard J. Walker
Senior Research Scientist Philip M. Piccoli

Acknowledgements

I would like to thank my committee, Drs Michael Brown, Rich Walker, and Phil Piccoli for their guidance and patience. I would also like to thank Dr Igor Puchtel for his assistance in the clean lab and Dr Richard Ash for his assistance in the plasma lab. I would like to thank Professor Christine Siddoway and Christopher Yakymchuk for their input and collaboration with the project. This study was funded by NSF grant ANT0944615 and partially funded from a GSA graduate student grant.

Table of Contents

List of Tables

List of Figures

Chapter 1: Introduction

1.1 Background

The continental crust comprises about 39% of Earth's surface (Sawyer *et al.*, 2011). While the bulk composition of the crust is andesitic, it is highly differentiated and stratified, with a mafic lower crust that is depleted in incompatible trace elements and a complementary felsic upper crust enriched in incompatible elements (Rudnick and Gao, 2003). There are three dominant processes that can lead to the formation of felsic melts. One process is melting of a peridotite. However, melting experiments on peridotite produce melts that are less evolved than the bulk continental crust (e.g., Jaques and Green, 1980; Hirose, 1997), suggesting that this either is not the dominant mechanism, or is not the only mechanism that produces felsic melts. Another option is mixing of a mantle component with a crustal component, a process that occurs in continental arcs. The third method is reworking of the continental crust by partial melting of the lower and middle crust, and melt transfer and emplacement in the upper crust (Brown, 1994, 1995, 2007). Partial melting of the lower crust explains certain geochemical characteristics of the upper continental crust, including a large negative Eu anomaly, and the enrichment in SiO_2, K_2O and light rare earth elements (Rudnick and Gao, 2003). It is this enrichment of the upper crust in incompatible elements, water, and heat producing elements such as K, U, and Th, that leads to the long term stability of the continental crust. This process of partial melting and redistribution of melt occurs predominately in active tectonic settings—mostly in continental arcs associated with subduction and continental collision zones since the Early Proterozoic (Brown *et al.*, 1995).

Anatexis of the deep crust produces granite melts (*sensu lato*) that may migrate and become emplaced in shallower portions of the crust. Therefore, granites provide a geochemical window into the processes of partial melting in the deep crust, and the chemical differentiation of the continental crust. I-type granites, or granites derived from igneous sources, are particularly enigmatic. They are generally metaluminous to peraluminous, and are chemically similar to continental arc granitoids. While some more mafic I-type granites are thought to contain a mantle component (e.g., Villaseca *et al.*, 2009; Collins, 1996; Kemp *et al.*, 2007) and could represent crustal growth, generally I-type granites are felsic and could be derived by partial melting of the crust, representing crustal reworking rather than growth (Brown, 1994; Sawyer, 1998; Annen *et al.*, 2006). The migration and extraction of melt may lead to entrainment of peritectic minerals, or leave residual minerals in the source that can affect the chemical signature of the melts (Clemens and Stevens, 2012; Clemens *et al*., 2011). By determining how the chemistry of melts relates to entrainment of peritectic minerals, the connections between products of partial melting and their sources can be better understood.

Isotopic tracers are commonly used to identify sources in studies of granite petrogenesis (e.g., Vailleros *et al.*, 2011; Clemens and Stevens, 2012; Yang *et al.*, 2007). Assuming equilibrium melting, the isotope signature of the melt should reflect that of the source. However, it is rare that a granite has a similar isotope signature to a single source (e.g., Farina and Stevens, 2011; Clemens and Stevens, 2012). Most likely, this could be due to heterogeneous source compositions (Vailleros *et al.*, 2011; Farina and Stevens, 2011) such that the granite could be the product of melting of a spectrum of lithologies and will yield diverse isotope compositions. Furthermore, melt could interact with the crust during transport and/or host rocks during emplacement, and, therefore, the granite may represent a mixture of multiple sources (Knesel and Davidson, 1996; Yakymchuk *et al.*, 2013a). Also, a granite could represent mineral fractionation during melting of the source (e.g., Jung et al., 2000).

The isotope composition of the melt may also be affected by how quickly the melt was extracted from the source and whether chemical equilibrium between melt and residue was attained (Harris and Ayres, 1998; Barbero *et al.*, 1995). Accessory minerals are commonly hosted along grain boundaries or as inclusions within major rock-forming minerals. If the melt does not interact with included accessory minerals, then the isotopic signature of the melt may be determined by the accessory minerals located along grain boundaries (in addition to major rock-forming minerals such as feldspar). Therefore, the isotope signature of melts that have not interacted with all minerals present in the source may be strongly influenced by the distribution and microstructural location of accessory minerals throughout the rock (Rapp and Watson, 1986; Hogan and Sinha, 1991; Zeng *et al.*, 2005a, 2005b, 2005c; Clemens *et al.*, 2011; Harrison and Watson, 1983; Evans and Hanson, 1993).

This study focuses on characterizing the source rocks of granites produced during melting at granulite-facies conditions at the former convergent margin of Gondwana, with the intent to better understand the processes associated with granite production in a continental arc setting. In West Antarctica, the Fosdick Mountains expose a migmatite–granite complex in the form of a gneiss dome. The complex represents an exposure of the deep crust where melt production, transfer, and loss occurred (Korhonen *et al.*, 2010a, 2010b). In addition, the low grade protoliths of the migmatites exposed in the Fosdick complex crop out in the surrounding mountain ranges. Therefore, the Fosdick complex and surrounding mountain ranges offer an ideal location to study the processes associated with granite production in the lower continental crust and to test petrogenetic models of granite production along the former Gondwanan margin.

Chapter 2: Regional Geology

2.1 Gondwana

During the Paleozoic-Mesozoic, the Gondwana active convergent margin stretched from East Australia through Antarctica to the tip of South America (Fig 1a). West Antarctica and the Western Provinces of New Zealand made up Zealandia, a currently submerged continental fragment lying under the Southern Ocean (Tulloch et al., 2006). The margin was fragmented during a period of regional extension. Around 85 Ma, Zealandia separated from the Antarctic margin. A rapid shift from convergence to divergence between 110 and 100 Ma, that led to eventual rifting, is thought to be due to either ridge–trench interaction (Bradshaw *et al*., 1983; Luyendyk, 1995; Mukasa and Dalziel, 2000), collision of the Hikurangi plateau with the trench (Davy and Wood, 1994; Mortimer *et al*., 2006; Davy *et al*., 2008), horizontal stresses due to buoyancy from the mantle wedge (Rey and Müller, 2010), or the presence of a mantle plume (Weaver *et al*., 1994). However, among these alternatives the presence of a mantle plume seems least likely, based on the rapid shift from subduction to extension (Mukasa and Dalziel, 2000), the absence of regional uplift in in portions of West Antarctica long the margin at the time of break-up (LeMasurier and Landis, 1996), and the geochemistry of mafic rocks emplaced around this time (Saito *et al*., 2013).

2.2 Marie Byrd Land, West Antarctica

Marie Byrd Land lies along the eastern side of the Ross Sea (Fig 1b and 1c) and is one of the major crustal blocks of West Antarctica (Dalziel and Elliot, 1982). The Ford Ranges of Marie Byrd Land are made up of Paleozoic basement rocks and Paleozoic–Mesozoic intrusive rocks. The oldest exposed unit in the Ford Ranges is the Swanson Formation, a meta-turbidite sequence that has been correlated with other terranes, based on whole rock K–Ar ages and initial Sr isotope values. These terranes include the Robertson Bay group in North Victoria Land, the Stawell and Bendigo terranes in Australia, and the Greenland Group in New Zealand (Ireland *et al.*, 1998, Adams, 1986; Adams, 2004; Bradshaw *et al.*, 1983). U–Pb ages of 1000–500 Ma from detrital zircons derived from granite protoliths suggest sediment provenance from the Ross–Delamerian orogen (Pankhurst *et al.*, 1998). Based on K–Ar and whole rock Rb–Sr isochrons, the Swanson Formation underwent a period of regional metamorphism at c. 450 Ma that resulted in folded and cleaved slates of sub-greenschist to greenschist facies (Adams, 1986). These metasedimentary rocks were intruded by the Ford Granodiorite suite (FGD), which comprises calc-alkaline, I-type granodiorites, emplaced during the interval 375–345 Ma (Adams, 1987; Pankhurst *et al.*, 1998; Siddoway and Fanning, 2009; Tulloch *et al.*, 2009; Yakymchuk, unpublished) during an episode of magmatism that occurred across the East Gondwana margin. The magmatism is attributed to subduction (Borg *et al.*, 1987; Weaver *et al.*, 1991) or back-arc extension (Muir *et al.*, 1996; Tulloch *et al.*, 2009). Coeval plutonic rocks outside Marie Byrd Land include the Karamea batholith in

New Zealand and the Admirality Intrusives in Victoria Land, Antarctica (Allibone *et al.*, 2009; Borg, 1987).

The Byrd Coast granite intrudes both the Swanson Formation and the Ford Granodiorite suite, and was emplaced during a period of intracrustal extension and back-arc plutonism (Adams, 1987; Weaver *et al.*, 1992; Muir *et al.*, 1994; Storey *et al.*, 1999; Mukasa and Danziel, 2000). U–Pb geochronology of zircons from the Byrd Coast granite yield ages of 105–99 Ma (Yakymchuk *et al.*, 2013a), which are contemporaneous with ages from the Separation Point batholith in the Western Province of New Zealand. The age of emplacement of these plutons coincides with the transition from wrench deformation to oblique extension (Siddoway 2004; McFadden *et al.*, 2010a) that ultimately led to the breakup of the former active margin of Gondwana.

2.3 Fosdick migmatite–granite complex

The Fosdick migmatite–granite complex (Fig 1d), part of the northern Ford Ranges, was exhumed in the Cretaceous during a period of regional extension. The migmatite–granite complex forms an 80 km by 15 km elongate dome containing layered sequences of paragneiss, orthogneiss, granite, and cross-cutting mafic intrusions. The paragneisses and orthogneisses are inferred to be the high-grade metamorphic equivalents of the Swanson Formation and the Ford Granodiorite suite, respectively, based on geochemistry and the distribution of zircon U–Pb ages (Korhonen *et al.*, 2010b). The granites were emplaced during the later stages of high grade metamorphic events in the Devonian–Carboniferous and the Cretaceous

(Siddoway *et al*., 2004; Korhonen *et al*., 2010b), and emplacement of the cross-cutting mafic intrusions was broadly co-eval with the Cretaceous granites. The dome is bounded in the north by the inferred Balchen Glacier fault, a steep dextral strike-slip fault (Siddoway *et al*., 2004, 2005), and in the south by the South Fosdick detachment, a south-dipping, dextral oblique detachment zone (McFadden *et al*., 2010a).

The Fosdick complex may be separated into three major plutono–metamorphic units: one dominated by migmatitic paragneiss, a layered plutonic complex (also referred to as the orthogneiss complex by McFadden *et al*. (2010a, 2010b), and a leucogranite sheeted complex (Siddoway and Fanning, 2009; Korhonen *et al*., 2010a, 2010b; McFadden *et al*., 2010a, 2010b). The migmatitic paragneiss is exposed in the central and western portions of the Fosdick complex. It comprises stromatic metatexite migmatite with cm- to dm-scale compositional layering composed of alternating concordant garnet-bearing leucosomes and biotite–silimanite-dominated melanosomes (McFadden *et al*., 2010; Yakymchuk et al., 2013b). The layered plutonic complex is also located in central and western portions of the complex, and is composed of 10 m- to 100 m-thick sheets of migmatitic orthogneiss and m- to dm-thick granite, granodiorite, diorite, and minor m- to 10 m-thick paragneiss layers. The migmatitic paragneiss and layered plutonic complex are intruded by hornblende-bearing mafic dikes and sills. The leucogranite sheeted complex is exposed in the eastern Fosdick Mountains and is composed of 100 m-thick subhorizontal leucogranites interlayered with 1–10 m-thick migmatitic paragneiss and orthogneiss. Subhorizontal foliation is defined by biotite and sillimanite and is parallel to alternating layers of leucogranite sheets and gneisses. Mafic dikes strike NNW-SSE, yield $^{40}Ar/^{39}Ar$ ages of 143–96 Ma, and are generally folded and boudinaged (Siddoway *et al*., 2005; McFadden *et al*., 2010b; Saito *et al*., 2013).

The mafic dykes are characterized by enrichment of large-ion lithophile elements (LILE) relative to light REEs and high field strength elements (HFSE) and a negative Nb anomaly that are consistent with rocks formed in a subduction setting (e.g., Pearce and Parkinson, 1993). This suggests that the mafic dykes were not formed from a mantle plume, but derived by melting of sub-arc-mantle previously metasomatized by fluids from a down-going slab (Saito *et al*., 2013). The deformation of the mafic dikes records the change from transpression to transtension (Korhonen *et al*., 2010b). Zircon and titanite U–Pb ages determined from Cretaceous granites collected from steeply foliated domains at Mt Iphigene, as well as ages determined from Cretaceous granites collected from subhorizontal granites and leucogranites at Marujupu and Mt Ferranto, and ages determined from Cretaceous granites collected from diorite dikes at Mt Iphigene suggest that the shift from wrench tectonics to extension occurred within 5–10 Ma (Saito *et al*., 2013; McFadden *et al*., 2010a, 2010b; Korhonen *et al*., 2010a, 2010b). Monazite, titanite, and zircon U–Pb ages from syn- and post-tectonic granites intruding the South Fosdick detachment constrain dome emplacement to c. 107–96 Ma (Richard *et al*., 1994; McFadden *et al*., 2010). $^{40}Ar/^{39}Ar$ ages suggest rapid cooling from 105–94 Ma (Richard *et al*., 1994).

The Fosdick complex (Fig. 1d) preserves evidence of two high temperature metamorphic events, during the Devonian–Carboniferous and the Cretaceous. The

Devonian–Carboniferous event is primarily preserved in deeper structural levels of the gneiss dome exposed in the western and central Fosdick Mountains. U–Pb ages of monazites from the paragneisses date the melting event from 376 to 302 Ma, overlapping and slightly post-dating the emplacement of the Ford Granodiorite suite (Korhonen *et al*., 2012). Granite in shear bands that lack internal foliation, provides a minimum age of migmatization of 365–355 Ma (McFadden *et al*., 2010a). Sr–Nd systematics indicate that the Carboniferous granites preferentially preserve melts derived from the Ford Granodiorite suite, although one Carboniferous granite has chemical and isotopic characteristics that are consistent with derivation from the Swanson Formation (Korhonen *et al*., 2010b). Phase equilibrium modeling of garnet-bearing orthogneiss and paragneiss assemblages yield temperatures 820–870°C and pressures of 7.5–11.5kbar (Korhonen *et al*., 2010a). Forward modeling indicates that while the Ford Granodiorite suite would be capable of producing 2–3 vol. % melt at these *P–T* conditions, the Swanson Formation would have been a more fertile source, capable of producing up to 25 vol. % melt, a minimum of 70% of which must have been extracted to preserve the high-grade metamorphic mineral assemblages in the paragneisses (Korhonen *et al*., 2010a). Granites produced from the Swanson Formation may have been emplaced at a higher structural level than the melts produced from the Ford Granodiorite suite and have been lost to erosion, which could explain their rare occurrence in the complex (Korhonen *et al*., 2010b).

The Cretaceous event is primarily recorded by granites found in the southern and eastern Fosdick Mountains, which are inferred to be shallow crustal levels exposed by the domal structure (McFadden *et al*., 2010). Magmatism during the

Cretaceous may have been a two-stage process. The first stage involved the production of granites and leucogranites derived from a Ford Granodiorite suite source that were emplaced within the Fosdick complex during transpression in the interval c. 120–110 Ma (Korhonen *et al*., 2010b; McFadden *et al*., 2010; Yakymchuk, unpublished data). The second stage involved the production of granites, including the Byrd Coast Granite, by anatexis of the Ford Granodiorite suite and both residual and fertile Swanson Formation sources during transtension in the interval c. 109–102 Ma (Korhonen *et al*., 2010b; McFadden *et al*., 2010; Yakymchuk, unpublished data). U–Pb ages of zircons from leucosomes and granites yield ages in the range c. 120–101 Ma, consistent with monazite U–Pb ages from granites of 106–96 Ma (Richard *et al*., 1994). Phase equilibrium modeling indicates metamorphic temperatures of 830–870°C and pressures of 6–7.5kbar (Korhonen *et al*., 2010a). Forward modeling suggests that the metasedimentary protoliths could have produced up to 30 vol. % melt, while the paragneisses, depleted of melt during the Devonian–Carboniferous melting event, could have only produced up to 12 vol. % melt at the calculated P–T conditions during the Cretaceous (Korhonen *et al*., 2010a). Forward modeling indicates the Ford Granodiorite suite would have produced up to 5 vol. % melt and would not have been a fertile source at shallower crustal levels. Therefore, Cretaceous granites that show Sr–Nd signatures similar to the Ford Granodiorite suite are inferred to have a deeper crustal source (Korhonen *et al*., 2010a, 2010b). Granites and leucosomes from the sheeted leucogranite complex below the South Fosdick detachment have chemical signatures that suggest derivation from the Swanson Formation and its high-grade equivalent. Accumulation of these melts within the complex likely weakened the crust and led to the exhumation and formation of the Fosdick dome.

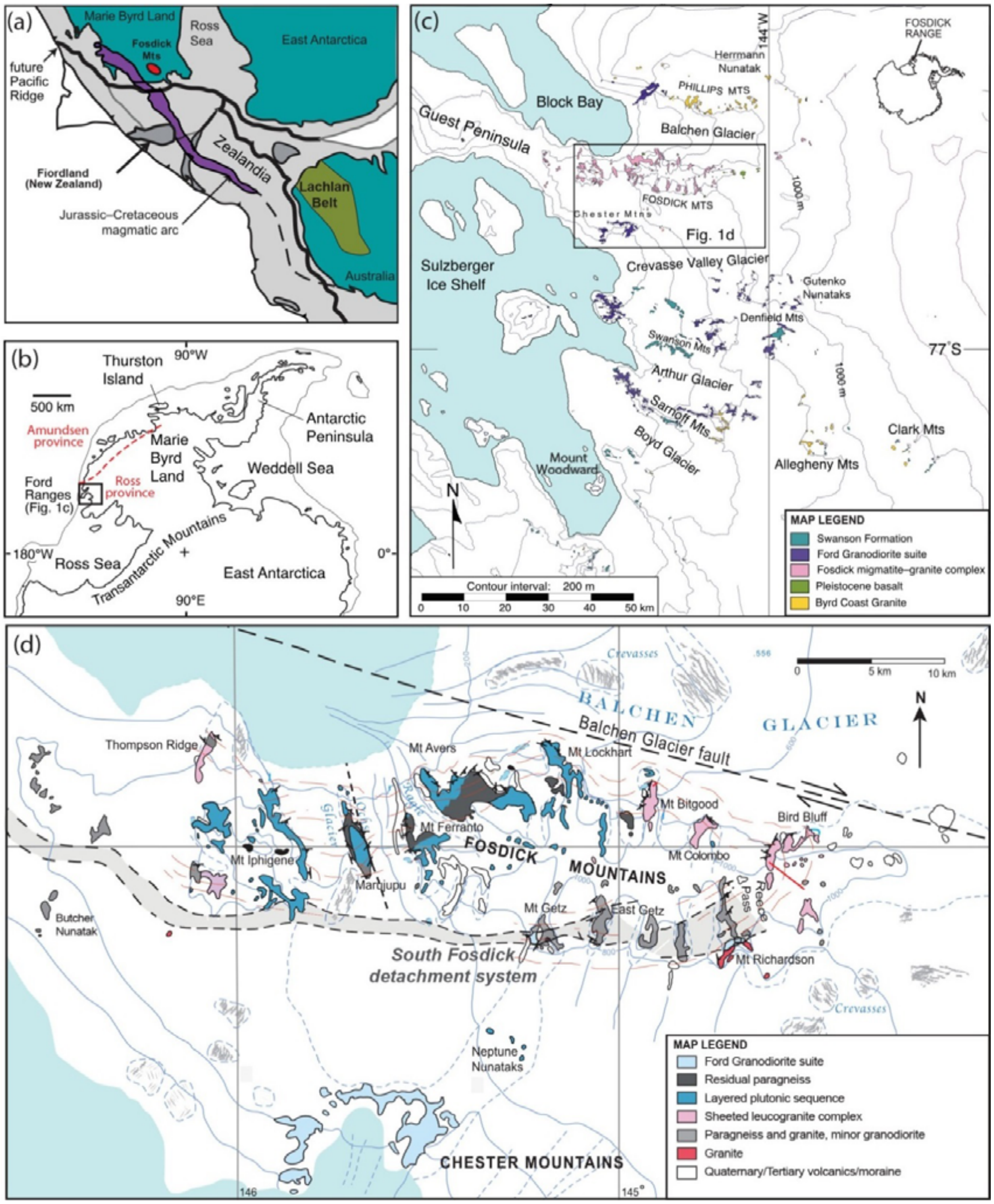

Figure 1. Regional geology modified after Yakymchuk *et al*., 2013a
(a) Reconstruction of West Antarctica at c. 95Ma (modified from Tulloch *et al*., 2006). (b) West Antarctica and Ford Ranges. (c) Geologic map of the Ford Ranges. (d) Geologic map of the Fosdick Mountains.

Chapter 3: Previous Results and Present Study

3.1 Previous results

Previous research on the Fosdick complex granites and their source rocks by Korhonen *et al.* (2010b) reported major oxide and trace element, rare earth element, and Sr–Nd isotope geochemistry. Results from this study indicated that granites produced during the Devonian–Carboniferous melting event were derived primarily by anatexis of an I-type granodiorite suite. Based on phase equilibria calculations, fluid-absent biotite breakdown melting of the Ford Granodiorite suite would have produced <5% melt at the pressures and temperatures within the complex. Therefore, Korhonen *et al.* (2010a) argued that the source of the granites would need to have been deeper than the exposed residual migmatites, in order to explain their volume at outcrop within the complex.

Devonian–Carboniferous granites derived from a metasedimentary source are not generally exposed in the complex, despite the metasedimentary rocks being a fertile source (Korhonen *et al.*, 2010a). The scarcity of these granites may be due to melt transfer to shallower crust than is exposed in the Fosdick complex. The Devonian–Carboniferous granites generally show high Sr and low Rb concentrations that that has been interpreted to reflect fluid-absent, biotite breakdown melting of the Ford Granodiorite suite (Korhonen et al 2010a, 2010b). Granites with low Sr and high Rb concentrations were interpreted to be derived from the metasedimentary source (Korhonen *et al.*, 2010b).

Cretaceous granites were derived from both the Ford Granodiorite suite and the Swanson Formation. Granites derived from the Swanson Formation show evidence of monazite remaining in the source during melting, based on low P_2O_5 content and elevated Sm/Nd ratios above the source. Monazite remaining in the source during melting and the presence of inherited zircon cores during the Cretaceous implies low water content in the melt, suggesting that the metasedimentary source may have been dehydrated prior to anatexis. The difference between the isotope composition of leucosomes and small-scale granites, and their source rocks, suggests that there was disequilibrium partitioning of elements between melt and residue, indicating that melt extraction exceeded the rate of accessory minerals dissolution.

3.2 This study

This study expands on the work done by Korhonen *et al*., (2010b) to test the validity of their petrogenetic models with a larger data set. Ultimately, these results could contribute to our understanding of granite petrogenesis and the differentiation of the continental crust in active convergent plate margins. In order to test the validity of the petrogenetic model set forth by Korhonen *et al.,* (2010b), U–Pb zircon ages of selected granites have been determined, and major and trace element concentrations and the Sr–Nd isotope composition of both the granites and their putative sources have been measured. U–Pb ages of zircons serve a two-fold purpose: (1) to expand the dataset of ages for these rocks in order to better constrain the timing of granite crystallization during each anatectic event, and (2) to provide age information for individual samples to be used to age-correct Sr and Nd isotope ratios to their crystallization ages. Whole-rock major element data and Sr–Nd isotope composition were used to characterize and determine the sources of the granites. Trace element compositions, including rare earth elements (REE), were used to assess the behavior of major rock-forming and accessory minerals during melting. The results from this study can be compared to other regions along the former convergent margin of Gondwana to determine if similar processes have occurred.

Chapter 4: Sample Descriptions

4.1 Swanson Formation

Samples 10CY-001 and 10CY-002 are low-grade metasedimentary rocks and were collected from two meters apart from each other in the Clark Mountains, within the Ford Ranges. 10CY-001 was collected from a layer that contained 1mm sized poikiloblasts of cordierite and 10CY-002 was collected from a 2–5 cm thick sandy layer. These two samples comprise fined-grained quartz and biotite that is aligned and surrounds cordierite poikiloblasts to 1 mm in diameter.

Thin section photos of this sample and subsequent samples are provided in appendix B.

Sample Y2-MD092 is low-grade metasedimentary rock collected from Mt Dolber, within the Ford Ranges. This sample is composed of contrasting layers of fine- and coarse-grained biotite and quartz. Biotite grains are variable in size but are less than 0.5 mm long, aligned, and have zircon inclusions. Fine-grained oxides are dispersed throughout the sample but there are higher concentrations of oxides along the edges of the fine-grained quartz and biotite layers.

Sample Y2-BR086 is a low-grade metasedimentary rock collected from Bailey Ridge, within the Ford Ranges. It is made up of fine grained biotite and quartz, with elongate muscovite and biotite grains, less than 0.5mm long, that surround poikiloblasts of cordierite.

Sample Y2-MP098 is a low-grade metasedimentary rock collected from Mt Passell, within the Ford Ranges. It is made up of fine-grained biotite with larger clasts of quartz. Some plagioclase feldspar is present.

4.2 Ford Granodiorite suite

Sample Y2-GP091 is a biotite–hornblende granodiorite collected from Greer Peak, within in the Ford Ranges. Sporadically distributed, chloritized, pleochroic brown to tan biotite grains 1–3 mm long contain inclusions of zircon and oxides, but similar-size, green, weakly, pleochroic green to light green hornblende grains only contain oxide inclusions. Twinned and zoned plagioclase grains 5–10 mm long are sericitized, whereas K-feldspar grains are smaller, up to 3mm long, but heavily sericitized. Quartz has undulatory extinction and sutured grain boundaries.

Sample Y2-SM095 is a biotite–hornblende granodiorite collected from Saunders Mountain, within the Ford Ranges. Sporadically distributed, chloritized, pleochroic brown to tan biotite grains 1–2 mm long contain inclusions of zircon and oxides. Pleochroic green to light green hornblende grains are a similar size. Twinned and zoned plagioclase grains 4–5 mm long are sericitized, whereas similar-size K-feldspar grains are heavily sericitized. Quartz shows undulatory extinction and sutured grain boundaries.

Sample Y2-HN097 a biotite–hornblende granodiorite collected from Hermann Nunatak, within the Ford Ranges. Sporadically distributed, chloritized pleochroic brown to tan biotite grains 2–3 mm long contain zircon, apatite, and oxide inclusions. Pleochroic green to light green hornblende grains are similar long. Twinned and zoned plagioclase grains up to 7 mm long are sericitized. K-feldspar grains are smaller, up to 3 mm long, and are heavily sericitized. Quartz grains have undulatory extinction and sutured grain boundaries.

Samples 51225-1 and 51225-2 are biotite granodiorites collected from the Chester Mountains, within the Ford Ranges. Sporadically distributed, pleochroic brown to tan biotite grains 1–2 mm long contain inclusions of apatite and zircon. Twinned and zoned plagioclase grains up to 3 mm long are sericitized. Potassium feldspar is present in the form of microcline grains up to 2 mm long that contain sillimanite inclusions. Small grains of muscovite are present. Quartz has undulatory extinction, subgrains, and sutured grain boundaries. Myrmekite is present.

Sample Y2-JU096 is a biotite–hornblende granodiorite collected from Mt June, within the Ford Ranges. Pleochroic brown to tan biotite grains are 2–3 mm long, and contain inclusions of apatite, zircon, and Fe–Ti oxides. Some grains of biotite are chloritized. Hornblende is less than 1 mm long. Twinned and zoned plagioclase grains up to 10 mm long are sericitized. Smaller, perthitic K-feldspar grains up to 5.5 mm long are also sericitized. Quartz has undulatory extinction and sutured grain boundaries. Apatite inclusions in biotite are up to 1 mm long.

Sample Y2-MS089 is a biotite granodiorite collected from Mt Swan, within the Ford Ranges. Pleochroic brown to tan biotite grains are 1–2 mm long, contain inclusions of zircon and apatite, and are chloritized. Plagioclase grains are up to 3 mm long and are heavily sericitized. Potassium feldspar grains are up to 6 mm long, has Carlsbad twinning, and sericitized. Some K-feldspar is present in the form of microcline. Quartz has undulatory extinction and sutured grain boundaries. Muscovite is present.

4.3 Paragneisses

Sample 10CY-010 was collected from Mt Bitgood, within the Fosdick Complex. Garnet is up to 3 mm in diameter and contains rounded inclusions of elongate, pleochroic brown to tan biotite grains up to 2 mm long, and zircon and monazite. Quartz grain size is variable from less than 1 mm in diameter to 6 mm long. Quartz has undulatory extinction and sutured grain boundaries.

Sample 10CY-015 was collected from Mt Bitgood, within the Fosdick Complex. It is a garnet- and biotite-bearing paragneiss. Garnet is anhedral, up to 4 mm in diameter and contains rounded inclusions of quartz. Elongate, pleochroic brown to tan biotite grains are up to 2 mm long and contain inclusions of zircon and monazite. Twinned plagioclase and K-feldspar grains up to 3 mm long are sericitized. Quartz has undulatory exaction and sutured grain boundaries.

Sample 10CY-021 was collected from Maigetter Peak, within the Fosdick Complex. Elongate, pleochroic brown to tan biotite grains are up to 2 mm long and contain inclusions of zircon and monazite. Sillimanite is present as fibrous bundles near biotite grain boundaries. Twinned plagioclase grains up to 2 mm long and K-feldspar grains up to 1 mm long are sericitized. Quartz has undulatory extinction and sutured grain boundaries. Myrmekite is present.

Sample 10CY-023 was collected from Maigetter Peak, within the Fosdick Complex. Elongate, pleochroic brown to tan biotite grains up to 2 mm long contain inclusions of zircon and monazite. Sillimanite is present as fibrous bundles near biotite grain boundaries. Twinned plagioclase grains up to 2 mm long and K-feldspar grains up to 1 mm long are sericitized. Quartz has undulatory exaction and sutured grain boundaries.

Sample 10CY-033 was collected from east Mt Avers, within the Fosdick Complex. Anhedral garnet up to 3 mm long is associated with biotite. Irregularly shaped pinitized cordierite is present. Elongate, pleochroic brown to tan biotite up to 2 mm long contains inclusions of zircon and monazite. Sillimanite is present in fibrous bundles near biotite grain boundaries. Twinned plagioclase up to 2 mm long and K-feldspar up to 1 mm long are sericitized. Quartz has undulatory extinction and sutured grain boundaries

Sample 10CY-041 was collected from east Mt Avers, within the Fosdick Complex. Anhedral garnet up to 2 mm in diameter has rounded quartz inclusions. Elongate biotite grains up to 3 mm long contains inclusions of zircon and monazite. Twinned plagioclase grains up to 5 mm long and K-feldspar grains up to 4 mm long are sericitized. Quartz has undulatory extinction and sutured grain boundaries. Myrmekite is present.

Sample Y1-BB013 was collected from Bird Bluff, within the Fosdick Complex. Generally unaltered cordierite grains 0.5–1.5 mm long contain inclusions of sillimanite and zircon, the latter with characteristic pleochroic halos. Elongate, pleochroic brown to tan biotite grains up to 2 mm long include zircon and monazite. Twinned plagioclase up to 5 mm long and K-feldspar grains up to 4 mm long are sericitized. Quartz has undulatory extinction and sutured grain boundaries. Myrmekite is present.

Sample Y1-CB080 was collected from Colombo, within the Fosdick Complex. Anhedral garnet up to7 mm in diameter contains rounded quartz inclusions. Anhedral cordierite is up to 3 mm in diameter. Elongate, pleochroic brown to tan biotite grains are up to 3 mm long and contain inclusions of zircon and oxides. Twinned plagioclase grains up to 5 mm in diameter are weakly sericitized. Quartz has undulatory extinction and sutured grain boundaries.

Sample Y1-IG057 was collected from Mt Iphigene, within the Fosdick Complex. Garnet is elongate, up to 6 mm long, and contains inclusions of sillimanite and quartz. Elongate, pleochroic brown to tan biotite up to 7 mm long is the dominant mineral, making up ~80% of the rock, defining a foliation; biotite contains inclusions of zircon and monazite. Sparsely distributed quartz grains are less than 1 mm in diameter.

Sample Y1-IG061 was collected from Mt Iphigene, within the Fosdick Complex. Garnet is up to 3 mm in diameter. Elongate, pleochroic brown to tan biotite grains are up 2 mm long and contain inclusions of zircons and monazite. Twinned plagioclase is sericitized. Quartz shows undulatory extinction and sutured grain boundaries.

Y1-LH077 was collected from Mt Lockhart, within the Fosdick Complex. Garnet up to 3 mm across is associated with pinitized cordierite. The foliation is defined by elongate, pleochroic brown to tan biotite grains up to 2 mm long that contain inclusions of zircon. Twinned plagioclase less than 1 mm in diameter and K-feldspar grains up to 2 mm long with rounded quartz inclusions are weakly sericitized. Quartz grains have undulatory extinction and sutured grain boundaries. Myrmekite is present.

Y1-MJ074 was collected from Marujupu, within the Fosdick Complex. Pinitized cordierite up to 4 mm long contains rounded inclusions of quartz. Elongate, pleochroic brown to tan biotite grains up to 2 mm long with zircon inclusions define a foliation. Twinned plagioclase grains up to 4 mm long and K-feldspar grains up to 7 mm long with rounded inclusions of quartz are sericitized. Quartz has undulatory exaction, sutured grain boundaries, and ranges in size from less than 1 mm in diameter to 3 mm in diameter.

3.4 Orthogneisses

Sample 10CY-035 was collected from Mt Avers, within the Fosdick Complex. Although a coarsely-spaced foliation is seen in hand sample, it is not apparent in thin section. Elongate, pleochroic brown to tan biotite up to 2 mm long contains zircon inclusions. Tabular twinned plagioclase grains up to 6 mm long contain rounded quartz inclusions and are weakly sericitized. Simply twinned perthitic K-feldspar up to 10 mm long has rounded quartz inclusions. Quartz grains show undulatory exaction and grain boundary migration. Myrmekite is present.

Sample Y1-AW039 was collected from west Mt Avers, within the Fosdick Complex. Elongate pleochroic brown to tan biotite grains up to 3 mm long define a weak foliation in thin section and contain inclusions of zircon and apatite. Twinned plagioclase and twinned K-feldspar grains are up to 5 mm long but are irregularly shaped. Quartz has undulatory extinction and sutured grain boundaries.

Sample Y1-AW049 was collected from west Mt Avers, within the Fosdick Complex. Elongate, pleochroic brown to tan biotite grains up to 2 mm long define a weak foliation and contain inclusions of zircon. Irregularly-shaped twinned plagioclase and K-feldspar grains are up to 4 mm long. Quartz has undulatory extinction and sutured grain boundaries.

4.5 Devonian–Carboniferous diatexites

Sample Y1-IG071 is a heterogeneous diatexite collected from Mt Iphigene, within the Fosdick Complex. Elongate, pleochroic brown to tan biotite grains are up to 2.5 mm long and contain zircon inclusions. Twinned plagioclase and twinned K-feldspar grains are up to 8 mm long and sericitized. Elongate grains of muscovite up to 1 mm long contain inclusions of plagioclase. Quartz has undulatory extinction and sutured grain boundaries.

Sample Y1-IG073 is a homogeneous diatexite collected from Mt Iphigene, within the Fosdick Complex. Elongate, pleochroic brown to tan biotite grains up to 2 mm long and contains zircon inclusions. Subhedral to anhedral twinned tabular plagioclase grains up to 5 mm long, have inclusions of rounded quartz, and are weakly sericitized. Anhedral K-feldspar grains are up to 4 mm long, have inclusions of rounded quartz, and are weakly sericitized. Quartz grains show undulatory exaction and have sutured grain boundaries.

4.6 Devonian–Carboniferous granites

Sample Y1-IG062 is a garnet–biotite granite from Mt Iphigene, within the Fosdick Complex. Garnet is euhedral, up to 1 mm in diameter and is associated with pleochroic green to light green biotite. Chloritized biotite grains up to 2 mm long contain zircon inclusions. Tabular twinned plagioclase up to 3 mm long with small inclusions of rounded quartz is sericitized. Tabular perthitic K-feldspar grains up to 10 mm long also contain small round inclusions of quartz and are sericitized. Quartz shows undulatory extinction and sutured grain boundaries. Myrmekite is present.

Sample C5-I26 is a cordierite–K-feldspar granite collected from Mt Iphigene, within the Fosdick Complex. Cordierite and cm-size K-feldspar are subhedral to euhedral. Quartz is optically uniform along grain boundaries (Siddoway and Fanning, 2009).

Sample C6-AW86-1 was collected from Mt Avers, within the Fosdick Complex. It is a K-feldspar granite with weak foliation defined by sparsely distributed biotite (Siddoway and Fanning, 2009).

Sample M5-G175 is a dark, medium-grained, equigranular biotite granodiorite collected from Mt Getz, within the Fosdick Complex (Siddoway and Fanning, 2009).

4.7 Cretaceous granites

Sample 10CY-039 is a biotite granite collected from east Mt Avers, within the Fosdick Complex. Pleochroic brown to tan biotite grains are up to 4 mm long, contain inclusions of rounded quartz, and are chloritized. Plagioclase grains are up to 5 mm long and strongly sericitized, K-feldspar grains are tabular, up to 7 mm long, twinned, and oriented. Quartz has undulatory exaction and sutured grain boundaries. Muscovite is present between grain boundaries.

Sample Y1-AE051 is a garnet–cordierite–biotite granite collected from east Mt Avers, within the Fosdick Complex. Anhedral garnet grains 5–11 mm in diameter contain inclusions of anhedral chloritized biotite and chlorite, and rounded quartz. Cordierite is 3–6 mm in diameter, occasionally associated with biotite, and frequently contains inclusions of rounded quartz and anhedral garnet. Elongate, pleochroic brown to tan grains of biotite up to 2 mm long contain inclusions of zircon. Tabular twinned plagioclase grains up to 7 mm long with inclusions of sillimanite are sericitized. K-feldspar grains up to 1 mm long are sericitized. Quartz grains show undulatory extinction and grain boundary migration. Muscovite occurs interstitially and myrmekite is present.

Sample Y1-AE064 is a garnet–biotite granite collected from east Mt Avers, within the Fosdick Complex. Garnet grains are anhedral to subhedral, are 2–5 mm in diameter, and contain inclusions of anhedral biotite and chlorite, and rounded quartz. Biotite is green pleochroic green to light green, up to 2 mm long, and is associated with garnet and chloritized when present as inclusions in garnet. Twinned plagioclase grains are 1–2 mm long. K-feldspar grains are up to 7 mm long, perthitic, sericitized, and have rounded quartz inclusions. Quartz has undulatory extinction and sutured grain boundaries. Muscovite is found interstitially. Myrmekite is present.

Sample Y1-AE033 is a garnet–cordierite granite collected from east Mt Avers, within the Fosdick Complex. Subhedral, garnet up to 3 mm in diameter contains inclusions of biotite, sillimanite, and rounded quartz. Irregularly shaped cordierite grains contain inclusions of quartz. Elongate, pleochroic brown to tan biotite grains up to 2 mm long are associated with garnet. Sillimanite is present in bundles along grain boundaries and included in garnet and feldspars. Anhedral twinned plagioclase grains up to 5 mm long contain inclusions of rounded quartz and sillimanite. Perthitic K-feldspar grains up to 8 mm long contain inclusions of rounded quartz and are sericitized. Quartz have undulatory extinction, have sutured grain boundaries, and are present as inclusions in feldspars and garnet. Muscovite is present as along grain boundaries and near cordierite grains. Myrmekite is present.

Sample Y1-AW038 It is a garnet-biotite bearing granite was collected from west Mt Avers, within the Fosdick Complex. Garnet grains are subhedral to euhedral, up to 5 mm in diameter, and contains inclusions of anhedral biotite and chlorite, and rounded quartz and frequently associated with biotite and chlorite grains. Pleochroic brown to tan biotite and chlorite are present both as elongate grains that are up to 3 mm long and contain zircon inclusions, and as anhedral grains infilling space between plagioclase grains and garnet. Tabular twinned plagioclase grains up to 4 mm long K-feldspar grains up to 5 mm long are both sericitized. Quartz has undulatory extinction and have sutured grain boundaries. Muscovite is present along grain boundaries. Myrmekite is present.

Sample Y1- IG052 is a garnet–cordierite–biotite granite collected from Mt Iphigene, within the Fosdick Complex. Anhedral garnet up to 7 mm in diameter contains inclusions of anhedral biotite and chlorite, and rounded quartz. Cordierite is anhedral and up to 2 mm long. Elongate grains of biotite up to 4 mm long are chloritized; they contain inclusions of zircon. Tabular twined plagioclase grains up to

4 mm long are sericitized. Tabular K-feldspar up to 6mm long is sericitized. Quartz has undulatory extinction and has sutured grain boundaries. Muscovite occurs interstitially. Myrmekite is present.

Sample Y1-IG070 is a garnet–biotite granite collected from Mt Iphigene, within the Fosdick Complex. Garnet grains are between 1 mm and 7mm in diameter. The larger, anhedral garnets contain inclusions of euhedral biotite and chlorite, and rounded quartz, whereas the smaller, euhedral garnets are surrounded by chloritized biotite. Chloritized biotite grains up 2 mm long contain zircon inclusions. Tabular twinned plagioclase grains and perthitic K-feldspar grains are up to 7 mm long and sericitized. Quartz grains have sutured grain boundaries and have undulatory extinction.

4.8 Cretaceous microgranite

Sample 10CY-024 is a biotite microgranite collected from Maigetter Peak, within the Fosdick Complex. Chloritized biotite grains up to 1 mm long contain zircon inclusions. Strongly sericitized, twinned plagioclase grains are up to 3 mm long. Perthitic K-feldspar grains have Carlsbad twinning and contain inclusions of plagioclase. Quartz has sutured grain boundaries and has undulatory extinction. Muscovite is present interstitially.

Chapter 5: Analytical Methods

5.1 U–Pb zircon analysis

Zircon grains were separated from whole rock samples using the rock crushing and mineral separation facilities at the University of Maryland. Samples were crushed using a steel mortar and pestle, passed through a 400 μm nylon mesh sieve, and run through a Franz Magnetic Separator. The non-magnetic fraction was subjected to a heavy liquid treatment of methylene iodide to separate quartz and feldspars from the heavy mineral fraction, then zircon grains were hand-picked to >90% purity. Separates were sent to the University of Arizona to be mounted following in-house procedures. To determine where to take the analyses, mounts were imaged at the University of Maryland NanoCenter using electron backscatter and cathodeluminescence (CL) imaging. U–Pb analysis was conducted at the University of Arizona LaserChron center using a Nu Plasma inductively coupled mass spectrometer (ICP-MS) with an Analyte G2 excimer laser, equipped with a HeLex ablation chamber, following procedures described by Gehrels *et al.* (2008). Preference was given to grains that were large and did not contain any inclusions or cracks.

Ages were calculated and U–Pb Terra-Wasserburg concordia graphs and probability histograms were constructed using Isoplot 4.1 (Ludwig, 2010). Terra-Wasserburg concordia diagrams were used because the curvature of the concordia plots that use ^{207}Pb/^{235}U and ^{206}Pb/^{238}U make determining ages younger than 1 Ga years less accurate than the Terra-Wasserburg concordia plot. Ages were corrected for elemental and isotopic fractionation using an in-house Sri Lankan zircon standard that yielded an average isotope dilution–thermal ionization mass spectrometer (ID–TIMS) age of 563.5 ± 3.2 Ma (Gehrels *et al.*, 2008). Final ages and systematic errors were propagated separately and added to the uncertainty of the weighted mean. Spot ages that were more than 10% discordant were discarded. Samples that showed a bimodal distribution of ages were re-assessed by creating unmixing plots using Isoplot (Ludwig, 2010; Sambridge and Compston, 1994), which determines the number of age components and the fraction of each age component. Box and whisker plots were created for all samples to determine which ages were within 2σ error. Those that fell outside of the whisker were determined to be outliers and were not considered in age calculations.

5.2 Major and trace element analysis

Major oxide and select trace elements were analyzed by X-ray fluorescence spectrometry (XRF) at Franklin and Marshall College. A PANanalytical 2404 X-ray fluorescence vacuum spectrometer equipped with a PW2540 X-Y sample handler was used following the procedures described by Boyd and Mertzman (1987).

Rare earth elements were analyzed by inductively coupled plasma mass spectrometry (ICP-MS) at the University of Maryland following sample preparation. USGS standards G-2, a granite standard, and MAG-1, a marine sediment standard, were used to calculate sample concentrations. Twenty milligrams of powdered sample, both unknowns and USGS standards G-2 and MAG-1, were dissolved in closed Savillex® Teflon beakers using 0.5 ml of 14M HNO_3 and 3mls of 29M HF. Samples were digested for 24 hours, dried down, and subjected to a second dissolution in 0.25 ml 12M $HClO_4$, 0.5 ml of 14M HNO_3 and 3 ml of 29M HF for 72 hours. The solution was dried down and then brought up in 6M HCl and dissolved for a further 24 hours. The dissolution in 6M HCl was repeated until the sample was fully dissolved, as evidenced by a clear solution. Samples were diluted by a factor of 100. One ml of a 20 ppb ^{115}In solution was added to the diluted sample to enable correction for instrumental drift. Indium was used due to its low abundance in samples and standards and negligible isobaric interferences.

Samples were analyzed for REE using a Finnigan Element 2 single collector ICP-MS; solutions were introduced into the plasma using an APEX desolvating nebulizer. Isotopes measured were ^{115}In, ^{139}La, ^{140}Ce, ^{141}Pr, ^{143}Nd, ^{147}Sm, ^{153}Eu, ^{158}Gd, ^{159}Tb, ^{163}Dy, ^{165}Ho, ^{167}Er, ^{169}Tm, ^{173}Yb, and ^{175}Lu.

Signals for samples and standards were corrected for instrumental drift by normalizing all data to the ^{115}In signal in the G-2 standard. Signals from the blank were subtracted from the In-normalized signal. Concentrations of each element in each sample were calculated based on the signal response of each isotope in a standard with well-established concentrations and a similar matrix to that of the samples. Granites, granodiorites and orthogneisses were corrected using USGS standard G-2, while metasedimentary and paragneiss samples were corrected using USGS standard MAG-1.

Uncertainties from counting statistics for samples and standards ranged from 1% to 6% with an average of 3.5%. Propagated uncertainties for concentrations ranged from 4% to 12%, with an average of 5%. Blanks were less than 0.1% of the signal for standards and less than 0.7% of the signal for samples.

For graphical representation, sample concentrations were normalized using the CI chondrite values from McDonough and Sun (1995).

5.3 Sr–Nd isotope analysis

To investigate granite petrogenesis, the Sr and Nd isotope systematics of 38 samples from varying locations from the Ford Ranges were determined. The rocks were prepared in a similar manner to Korhonen *et al.* (2010b). Samples were crushed in a steel mortar and pestle and powdered using a shatterbox with a ceramic insert. The resulting powders were dissolved as follows. Fifty milligrams of powder were dissolved in Savillex® Teflon beakers using 3 ml 29M HF, 0.5 ml 14M HNO_3 together with isotopic spikes enriched in ^{87}Rb, ^{84}Sr, ^{149}Sm, and ^{150}Nd using a closed digestion at 180–190ºC for 24 hours. Samples were dried and re-dissolved in 3 ml 29M HF, 0.5 ml 14M HNO_3, and 0.25 ml of 12M $HClO_4$ and digested for a further 72 hours at 180–190ºC, then dried. Finally, 2 ml of 6M HCl was added to the samples and digested at 180ºC for 24 hours and dried down. The digestion in 6M HCl was repeated until the resulting solution was clear. The samples were then dried and brought up in 2 ml of 2.5M HCl.

Rubidium, Sr and REEs were separated from each other using a primary cation exchange column filled with AG50Wx4 (200–400 mesh) resin. Samples were loaded in chloride form. Rubidium and Sr were eluted in 2.5M HCl while the REE were eluted from the column in 6M HCl. Rubidium cuts were dried and diluted in 2%

HNO_3. Strontium cuts were passed through a clean-up column filled with Eichrom™ Sr-spec resin and eluted in 0.05M HNO_3. The REE cuts from the primary column were passed through a second column filled with 0.225M 2-Methyllactic acid (MLA). Samarium and Nd were eluted in 0.225M MLA (pH = 4.67).

Strontium, Nd and Sm ratios were analyzed using a VG Sector 54 TIMS. Strontium cuts were loaded onto a single Re filament with a Ta-oxide activator, and analyzed in a multi-dynamic mode. Strontium isotopes were corrected for mass fractionation by normalizing the measured $^{87}Sr/^{86}Sr$ ratio to an $^{86}Sr/^{88}Sr$ ratio = 0.1194. The mass fractionation corrected and spike corrected $^{87}Sr/^{86}Sr$ ratio was normalized to an average SRM 987 $^{87}Sr/^{86}Sr = 0.710238$ (n = 30; appendix F) to correct for instrumental bias. Strontium blanks concentrations averaged 14.0 ng (n = 4) were less than 1% of the samples' Sr concentration.

Rubidium ratios were measured using a Nu Plasma multi-collector inductively-coupled mass spectrometer (MC-ICP-MS). Samples were diluted by a factor of 100 and were introduced into the plasma using an Aridus I desolvating nebulizer. A 50 ppb Rb SpecPure® plasma standard was introduced after every three sample analyses and was used to correct for instrumental fractionation and drift. Rubidium blanks averaged 8.04 ppm (n = 4) and were less than 1% of the Rb concentrations found in the samples. $^{87}Sr/^{86}Sr$ ratios were age corrected to 360 Ma and 100 Ma using the formula

$$\frac{^{87}\mathrm{Sr}}{^{86}\mathrm{Sr}} = \left(\frac{^{87}\mathrm{Sr}}{^{86}\mathrm{Sr}}\right)_t + \frac{^{87}\mathrm{Rb}}{^{86}\mathrm{Sr}}\ (e^{\lambda t} - 1)$$

where $\lambda = 1.3968 \times 10^{-11}\ yr^{-1}$ (Rotenberg *et al.,* 2012).

Neodymium and Sm were loaded on two Re filaments with phosphoric acid and loaded into the machine in a triple filament arrangement. Neodymium ratios were measured in dynamic mode and corrected for mass fractionation by normalizing the measured ^{143}Nd/^{144}Nd ratio to ^{146}Nd/^{144}Nd = 0.7219. The fractionation and spiked corrected ^{143}Nd/^{144}Nd ratio was normalized to an average Ames ^{143}Nd/^{144}Nd = 0.512126 (n = 33; appendix F) value to correct for instrumental bias. Samarium cuts were run in a static mode. Neodymium isotope ratios were age corrected to 360 Ma or 100 Ma using the formula

$$\frac{^{143}\mathrm{Nd}}{^{144}\mathrm{Nd}} = \left(\frac{^{143}\mathrm{Nd}}{^{144}\mathrm{Nd}}\right)_t + \frac{^{147}\mathrm{Sm}}{^{144}\mathrm{Nd}}\,(e^{\lambda t} - 1)$$

where $\lambda = 6.54 \times 10^{-12}\ \mathrm{yr}^{-1}$ (Lugmair and Marti, 1978). Samarium blanks averaged 0.311 ng (n = 3) while Nd blanks averaged 2.28 ng (n = 3). Both Sm and Nd blanks were less than 1% of sample Sm and Nd abundances.

5.5 Sr and Rb spike calibration

Strontium and Rb spike concentrations were re-calibrated prior to use. Ten mixtures of SpecPure Rb plasma standard and Rb isotopic spike (97.99% ^{87}Rb) in spike:standard ratios of 2:1, 2:2, 2:3, 2:4, and 2:5 were analyzed using the Nu Plasma MC-ICP-MS. Repeated analyses yielded an average Rb concentration of 106.0 ± 0.4 ppm. This spike was then diluted twice by mass. The first dilution was to 10.52 ppm and was used for sample analysis. The second dilution was to 0.148ppm and was used for blank analysis. Five mixtures of SpecPure® Sr plasma standard and SRM 988 (99.89% ^{84}Sr) in spike:standard ratios of 1:1, 1:1.5, 1:2, 1:2.5 and 1:3 were made.

Spike:standard mixtures were analyzed using a VG Sector 54 TIMS. Repeated analyses yielded an average Sr concentration of 8.085 ± 0.007 ppm that was also diluted twice by mass. The first dilution was to 0.9152 ppm that was used for sample analysis and the second dilution was to 0.00733 ppm and was used for blank analysis.

5.6 Standard Reproducibility

USGS G-2 granite standard was analyzed 7 times over a period of 12 months using ID-TIMS and ID-ICP-MS (appendix F). Repeat analyses yielded an average $^{87}Sr/^{86}Sr$= 0.709767 ± 0.000038 (n = 7) and an average $^{143}Nd/^{144}Nd$ = 0.512243 ± 0.000010 (n = 7). Rubidium concentrations for G-2 average 167.6 ppm and range from 162.9–174.2 ppm. Strontium concentrations average 488.8 ppm and range from 482.1–496.2 ppm. Rb/Sr ratios range from 0.3367–0.3511. Samarium concentrations for G-2 average 7.1 ppm and range from 7.0–7.3 ppm. Neodymium concentrations average 52.6 ppm and range from 52.2–53.2 ppm. Sm/Nd ratios range from 0.1344–0.1372.

Chapter 6: Results and Discussion

6.1 U–Pb geochronology results

In order to investigate the timing of melt crystallization, U–Pb isotopes were used to date zircon separates from granites and orthogneisses. These ages were used to correct Sr and Nd isotope ratios to their ages of crystallization. Of the 21 samples for which zircon was separated, 5 samples are from the Ford Granodiorite suite, 7 samples are granites, 5 samples are orthogneisses, 1 sample is a homogenous diatexite and 1 sample is a heterogeneous diatexite, and 1 sample is a microgranite. Ford Granodiorite locations are from both within and outside of the Fosdick complex. Orthogneisses, granites and diatexites were taken from locations on the west side of the mountain range, predominately from Mt Avers and Mt Iphigene, but also from Marujupu Peak. Locations of granite samples are provided in appendix A, individual spot U–Pb ratios and associated ages are given for each sample in appendix C, box and whisker plots are provided in appendix D, and concordia plots for each sample are provided in appendix E.

Four samples from the Ford Granodiorite suite (51225-1, 51225-2, Y2-GP091, and Y2-JU096) were collected from outside of the complex. One sample, Y1-AE035, was collected from Mt Avers, inside the Fosdick complex. These samples were chosen to increase the geographic distribution of zircon ages for the Ford Granodiorite suite. Zircons from the Ford Granodiorite suite are generally euhedral, prismatic and elongate. Samples 51225-1 and 51225-2 have oscillatory-zoned magmatic zircons with zoned magmatic cores. Zircons from Y2-JU096 and Y2-

GP091 are oscillatory zoned with cores that show mild evidence of recrystallization as evidenced by irregularly shaped zonation. Samples from Y1-AE035 are zoned and comprise a mix of euhedral, prismatic and elongate grains, and euhedral, stubby grains. Mean ages from this study for the Ford Granodiorite Suite range from 372.3 to 364.5 Ma and are consistent with published ages of 375–345 Ma (Adams, 1987; Pankhurst *et al*., 1998; Siddoway and Fanning, 2009; Tulloch *et al*., 2009; Yakymchuk, unpublished).

Orthogneiss samples are from Mt Iphigene (Y1-IG053), Mt Avers (Y1-AW039, Y1-AW049, 10CY-035, and Marujupu Peak (Y1-MJ075). Magmatic zircons from Y1-IG053 and from Y1-AW049 are stubby to elongate, prismatic, zoned, with a few grains showing bright cores that show evidence of recrystallization. Y1-IG053 and Y1-AW049 yield Devonian ages of 366.8 ± 6.2Ma and 361.2 ± 6.2, respectively. Zircons from sample 10CY-035 are elongate and prismatic, but have cores that show evidence of recrystallization that is surrounded by a darker zoned area which is then surrounded by very thin bright rim as seen in cathodoluminescence. Zircons from this sample also yield Devonian ages, but are characterized by a larger range of ages from 380–100 Ma, with three dominant populations at 360 Ma, 320 Ma and 100 Ma. The darker zoned areas from this sample give Devonian–Carboniferous ages while the brighter rims give Cretaceous ages, suggesting that this sample has a crystallization age of c. 100 Ma, but an inherited core that crystallized c. 360 Ma. Zircons from Y1-MJ075 are stubby to elongate and show evidence of recrystallization. These zircons have ages that range from 1520 to 100 Ma with a dominant population at 115.5 ± 3.7 (n = 7; MSWD = 2.2). Zircons from sample from Y1-AW039 are zoned, euhedral to anhedral and are a mix of elongate and stubby grains. Sample Y1-AW039 yields a generally uniform age of 368.5 ± 5.3 (n = 15; MSWD = 1.1). Generally the orthogneiss yields consistent Devonian ages with one sample yielding a Cretaceous age.

Samples Y1-IG071 and Y1-IG073 are from Mt Iphigene. The zircons from the homogeneous diatexite sample Y1-IG073, are euhedral to subhedral, prismatic, elongate with zoned cores that show evidence of recrystallization. The homogenous diatexite yields an age of 362.4 ± 5.7 Ma (n = 21; MSWD = 2.1). The zircons from the heterogeneous diatexite sample Y1-IG071, are euhedral to anhedral, prismatic, and elongate to stubby. Zoned inherited cores show evidence of recrystallization. The cores are surrounded by a darker zoned rim, which is surrounded by a thin, bright rim. The darker zoned rim is interpreted to be the age of protolith crystallization while the bright rim is interpreted to reflect the age the granite crystallized. Zircons from sample Y1-IG071 yield a range of ages from 800 to 100 Ma, with a dominant age population between 300 and 400 Ma.

The granites yielded two age populations at c. 360 Ma and c. 100 Ma. One granite from Mt Iphigene, sample Y1-IG062, has zircons that are zoned, predominantly prismatic and euhedral with a few that have bright zoned cores that show evidence of recrystallization. This granite was the only sample analyzed to yield a Devonian age of 363.2 ± 5.0 Ma (n = 12; MSWD = 1.7).

Other granites from Mt Iphigene (Y1-IG070 and Y1-IG052) and from Mt Avers (Y1-AW038, 10CY-039, Y1-AE051, and Y1-AE064) yielded zircons that are euhedral and prismatic with dark cores. Ages were obtained from bright overgrowths.

The dark cores could not be analyzed due to high concentrations of ^{204}Pb. Zircons from these samples yielded ages from 108 to 102 Ma, with two samples that showed evidence of two age populations. Sample Y1-AW038 has a zircon population at 113.6 ± 2.9 Ma and another at 105.1 ± 2 Ma. Sample Y1-AE051 also shows evidence of two zircon populations at 107.2 ± 1.3 Ma and 100.0 ± 1.8 Ma. Zircons from the microgranite sample, 10CY-024, from Maigetter Peak yield a Cretaceous age of 104.3 ± 1.8 Ma (n = 19; MSWD = 1.05).

Given that zircons from the first metamorphic event yielded Devonian ages, contrasting with ages from the Korhonen *et al.,* (2010b), Sr and Nd from this study are age-corrected to 360 Ma instead of 350 Ma. Data from the Korhonen *et al.,* (2010b) study have been recalculated to 360 Ma so that the full range of data now available for the Devonian–Carboniferous samples may be discussed below.

6.2 Major and trace elements results

Whole rock major oxide and trace element compositions determined by XRF are given in Table 1 and presented in Figure 2. Rare earth element concentration results, as determined by ICP-MS, are presented in Table 2, and chondrite-normalized patterns are presented in Figure 3.

Putative sources

Samples from the Swanson Formation have SiO_2 content ranging from 61 to 74 wt %; they are peraluminous with aluminum saturation indices (ASI= Molar [$Al_2O_3/(CaO+Na_2O+K_2O)$]) of 1.24–2.08. For this suite of samples, TiO_2, ($MgO+FeO^*$), CaO and Na_2O remain relatively constant with increasing SiO_2

content, while Al_2O_3 and K_2O are negatively correlated with increasing SiO_2 content (Fig. 2). Rubidium and Rb/Sr are also negatively correlated with increasing SiO_2. Barium and Th remain constant with increasing SiO_2, whereas Sr and Zr are positively correlated with increasing SiO_2. Samples from the Swanson Formation have a limited range of absolute and relative abundances of REE and are characterized by smooth to concave down patterns for the LREE (La–Gd) and smooth HREE (Tb–Lu) patterns (Fig. 3). The La to Lu slopes of the Swanson Formation samples are relatively consistent (La/Lu = 1.5–2.8); all samples have a negative Eu anomaly (Eu/Eu* = 0.55–0.70).

Samples from the Ford Granodiorite suite from within the Fosdick complex, and from the surrounding area, have SiO_2 contents ranging from 66 to 70 wt%, except one sample that has SiO_2 of 76 wt % (Fig. 2). The samples are metaluminous to peraluminous (ASI = 0.98–1.12). For this suite of samples, (CaO, Na_2O, K_2O, ASI, Rb, Sr, Rb/Sr, Ba, Zr and Th are all have positive correlation with increasing SiO_2 content. TiO_2 (MgO+FeO*), Al_2O_3, and ASI have a negative correlation with SiO_2. Samples from the Ford Granodiorite suite have smooth to concave down patterns for the LREE and smooth to concave up HREE patterns (Fig. 3). All samples have negative Eu anomalies (Eu/Eu*=0.31–0.85).

Paragneisses have major oxide and trace element abundances and trends that are similar to the Swanson Formation rocks. Paragneisses generally have SiO_2 content ranging from 60 to 75 wt %; these samples are peraluminous (ASI = 1.25–2.19). One biotite-rich paragneiss sample, Y1-IG057, has 42 wt % SiO_2 and an ASI value of 3.13. For these samples, TiO_2, Al_2O_3, CaO, Ba, and Zr correlate negatively with increasing SiO_2, while (MgO+FeO*), ASI, Na_2O, Rb, Sr, Rb/Sr and Th are relatively constant (Fig. 2). Sample Y1-IG057 has higher TiO_2, Al_2O_3, Rb, Rb/Sr, and Th, and lower CaO, Na_2O, and Sr than the rest of the paragneiss samples. These results are consistent with the predominance of biotite in this sample. Chondrite-normalized REE patterns for the paragneisses show a wider range of LREE concentrations than those for the Swanson Formation, but otherwise show a similar pattern of chondrite-normalized abundances (Fig. 3). All paragneiss samples have negative Eu anomalies that varies in magnitude (Eu/Eu* = 0.17–0.90). Sample Y1-IG057 has the smallest Eu anomaly (Eu/Eu* = 0.17) as well as elevated HREE compared with the other paragneiss and Swanson Formation samples.

Orthogneisses have major oxide and trace element abundances and trends that are consistent with a Ford Granodiorite suite parentage. Orthogneisses have SiO_2 content ranging from 64 to 74 wt %; the range of ASI values is small (ASI = 1.05–1.10). With increasing SiO_2, the orthogneisses have decreasing TiO_2 and (MgO+FeO*), constant Al_2O_3, ASI, Na_2O, CaO, Sr, and Zr, and increasing K_2O and Ba, and slightly increasing Rb, Rb/Sr and Th (Fig. 2). Orthogneisses have LREE concentrations that broadly overlap the LREE concentrations of the Ford Granodiorite suite, except sample Y1-MJ075, which has higher LREE concentrations (Fig. 3). There is some variability in the abundances of HREE and the overall HREE chondrite-normalized patterns that reflects the presence or absence of garnet. The orthogneisses have negative Eu anomalies (Eu/Eu* = 0.44–0.87), except sample 10CY-035, which has a positive Eu anomaly (Eu/Eu* = 1.48).

Diatexites and Granites

Two Devonian-Carboniferous diatexites have SiO_2 of 71 and 73 wt%; they are both metaluminous (ASI = 1.13 and 1.16). Both samples have Rb/Sr ratios <1 (Table 1). Sample Y1-IG073 has twice as much Ba (Ba = 1109 ppm) as sample Y1-IG071 (Ba = 551 ppm). With the exception of Ba, the other major and trace element abundances are comparable to each other. The REE abundances and the steep chondrite-normalized patterns (La/Lu = 21.5–57.1) of the diatexites are similar to those of the Ford Granodiorite suite or the Swanson Formation (Fig. 3). They have negative Eu anomalies (Eu/Eu* = 0.52 and 0.64).

Devonian–Carboniferous granites have SiO_2 contents ranging from 65 to 76 wt %; they are metaluminous to peraluminous (ASI = 0.99–1.20). The granites show decreasing TiO_2, Al_2O_3, (MgO+FeO*), CaO, Ba, Zr, Th, and Rb with increasing SiO_2 (Fig. 2). The samples have ASI, Na_2O, K_2O, Sr and Rb/Sr that remain relatively constant with increasing SiO_2; Rb/Sr ratios are <1 (Table 1).

Devonian–Carboniferous granites have varied LREE and HREE abundances as well as both positive and negative Eu anomalies (Eu/Eu* = 0.4–1.1). Sample C6-AW86-1 from Mt Avers has the steepest La/Lu slope (La/Lu = 82.6), the steepest Tb/Lu slope (Tb/Lu = 6.79), and is depleted in HREE compared to the Swanson Formation and the Ford Granodiorite suite (Fig. 3). Sample Y1-IG062 has the lowest LREE concentrations of the Devonian–Carboniferous granites and also has the lowest Tb/Lu and La/Lu slopes (Tb/Lu = 0.42; La/Lu = 1.77). The HREE concave upward pattern is likely due to the presence of garnet in the sample. Sample C5-I26 has concentrations of LREE and HREE that are almost twice as high as the Ford Granodiorite suite. This sample also has P_2O_5 of 1.2 wt % that is an order of magnitude higher than all of the other samples analyzed. Only one sample, M5-G175, has REE abundances and a REE pattern comparable to the Ford Granodiorite suite.

Cretaceous granites have silica contents ranging from 71 to 78 wt % and have a higher and more limited range of SiO_2 contents than the Devonian–Carboniferous granites. Cretaceous granites have TiO_2, Al_2O_3, (FeO*+MgO) and Zr content that are negatively correlated with increasing SiO_2 content (Fig. 2). Rb, Rb/Sr and Th show slight decreasing trends with increasing SiO_2. The Cretaceous granites have CaO, Na_2O, ASI, Ba, and Sr contents that show no obvious trend with increasing SiO_2 content. Sr and K_2O content is positively correlated with increasing SiO_2 content with one outlier, sample Y1-AW038, which has a greater K_2O weight percent than would be expected for its SiO_2 content. The Cretaceous microgranite has oxide and trace element abundances similar to the other Cretaceous granites, except for TiO_2, Zr, and Th, which are significantly elevated over other Cretaceous granites.

The Cretaceous granites are generally depleted in REE compared with the potential sources (Fig. 3). All show moderate to strong positive Eu anomalies ($Eu/Eu^* = 1.17–7.91$). HREE patterns are not flat and have Tb_N/Lu_N values that range from 0.17–4.01. Samples Y1-IG052, Y1-AE051 and Y1-AW038 have increasing, concave downward HREE patterns that are consistent with the presence of garnet. The Cretaceous microgranite, 10CY-024, has REE abundances that are greater than the other Cretaceous granites, with a negative, concave downward chondrite-normalized LREE slope and a negative, concave upward chondrite-normalized HREE pattern. This sample also has a negative Eu anomaly ($Eu/Eu^* = 0.37$).

Table 1: Whole-rock major oxide and trace element composition as determined by XRF

Rock Type:	**Swanson Formation**					**Ford Granodiorite Suite**			
Sample Name:	**10CY-001**	**10CY-002**	**Y2-BR086**	**Y2-MD092**	**Y2-MP098**	**51225-1**	**51225-2**	**Y2-GP091**	**Y2-HN097**
wt %									
SiO_2	64.33	63.92	71.59	73.92	74.06	68.24	66.43	67.50	69.08
TiO_2	0.68	0.70	0.73	0.57	0.68	0.70	0.78	0.59	0.53
Al_2O_3	15.86	16.52	14.02	11.54	12.00	15.13	15.37	15.35	14.98
Fe_2O_3	0.70	0.74	0.58	0.21	0.57	0.39	0.56	0.89	0.83
FeO	5.70	5.82	4.08	4.03	4.06	3.61	4.01	2.47	2.43
MnO	0.11	0.11	0.08	0.11	0.11	0.07	0.07	0.06	0.06
MgO	3.69	3.76	2.41	2.97	2.78	1.42	1.62	2.02	1.77
CaO	3.01	1.25	0.94	2.31	1.47	2.67	2.59	3.20	3.15
Na_2O	2.20	2.44	1.70	1.57	1.93	3.19	3.03	3.83	3.97
K_2O	3.02	4.24	3.36	2.33	2.15	3.7	4.19	3.05	2.52
P_2O_5	0.18	0.17	0.19	0.17	0.18	0.22	0.24	0.18	0.17
LOI	1.50	1.86	2.05	0.98	1.97	1.06	1.05	1.62	0.94
Total	100.11	100.32	100.13	100.18	100.44	99.74	99.34	99.42	99.76
ASI	1.28	1.52	1.52	1.24	1.47	1.07	1.08	1.00	1.00
(FeO+MgO)	9.38	9.55	6.48	6.99	6.81	5.04	5.67	4.52	4.21
ppm									
Rb	140	196	163	99	96	189	209	144	88
Sr	207	149	137	196	155	223	218	378	354
Rb/Sr	0.7	1.3	1.2	0.5	0.6	0.8	1.0	0.4	0.2
Y	32	34	39	33	39	32	35	23	24
Zr	123	121	172	166	233	228	240	146	143
V	131	112	89	80	84	73	82	77	72
Ni	110	118	43	106	112	9	10	37	35
Cr	110	118	84	123	151	33	36	60	80
Nb	12	13	15	12	14	20	21	13	15
Ga	21	21	19	16	17	22	22	19	20
Cu	39	41	6	8.0	30	12	23	9	9
Zn	120	152	85	74	78	66	73	48	46
Co	26	28	18	17	17	11	14	12	11
Ba	483	658	727	426	438	514	565	483	472
La	26	29	32	30	37	34	44	24	23
Ce	69	75	82	65	83	75	105	51	44
U	3.1	1.4	3.8	1.9	3.8	5.1	5.3	2.1	4.9
Th	14	17	14	14	13	15	25	15	5
Sc	18	16	12	12	12	11	12	11	9
Pb	8	12	15	11	3	15	28	<1	10

Table 1: Continued

Rock Type:	**Ford Granodiorite Suite**				**Orthogneiss**				
Sample Name:	**Y2-JU096**	**Y2-MS089**	**Y2-SM095**	**Y1-AE035**	**10CY-035**	**Y1-AW049**	**Y1-AW039**	**Y1-IG053**	**Y1-MJ075**
wt %									
SiO_2	69.10	76.00	67.38	66.59	74.19	64.19	67.82	65.51	72.84
TiO_2	0.54	0.15	0.68	0.87	0.08	0.92	0.76	0.89	0.29
Al_2O_3	15.00	13.76	15.29	16.04	14.29	16.48	15.85	16.60	14.80
Fe_2O_3	0.53	0.27	1.06	1.15	0.06	1.65	0.91	1.03	0.28
FeO	2.68	0.77	3.14	3.71	0.50	3.70	3.42	3.86	1.49
MnO	0.05	0.04	0.07	0.06	0.01	0.07	0.08	0.07	0.03
MgO	1.66	0.27	2.35	1.63	0.23	1.95	1.71	2.02	0.63
CaO	2.74	0.88	3.92	3.52	0.89	3.62	2.86	3.95	1.30
Na_2O	3.48	3.29	3.40	3.68	2.43	4.09	4.17	3.40	3.44
K_2O	3.35	4.88	2.63	2.26	7.22	2.17	2.23	2.20	5.03
P_2O_5	0.16	0.06	0.17	0.27	0.08	0.29	0.31	0.30	0.16
LOI	1.71	1.32	1.36	1.05	0.43	1.08	1.18	1.01	0.69
Total	99.59	100.46	100.44	100.19	100.04	99.54	100.50	100.26	100.46
ASI	1.05	1.12	0.98	1.08	1.06	1.05	1.10	1.10	1.10
(FeO+MgO)	4.36	1.04	5.47	5.33	0.73	5.68	5.13	5.86	2.11
ppm									
Rb	117	381	99	146	201	131	149	128	236
Sr	418	90	346	281	264	291	186	280	158
Rb/Sr	0.3	4.2	0.3	0.5	0.8	0.5	0.8	0.5	1.5
Y	35	35	27	23	6	16	31	25	13
Zr	173	89	155	256	93	260	198	191	261
V	73	14	97	100	15	101	93	102	26
Ni	34	3	35	10	4	12	14	12	6
Cr	64	14	78	58	24	61	59	65	28
Nb	15	23	10	17	3	17	20	14	17
Ga	19	20	19	22	15	23	24	23	21
Cu	9	3	9	8	3.0	5.0	10	17	4.0
Zn	53	34	59	80	14	88	74	78	41
Co	11	<1	15	14	<1	17	14	16	1
Ba	628	209	525	690	963	388	267	486	945
La	38	23	29	23	19	28	23	18	51
Ce	80	46	55	50	32	60	49	38	122
U	4.7	3.5	2.3	2.2	1.9	2.1	3.9	2.9	8.4
Th	16	14	9	6	6.8	6.7	8.0	1.5	17
Sc	11	3	11	16	<1	16	14	16	5
Pb	189	26	22	21	47	14	2	15	38

Table 1: Continued

Rock Type:	Paragneiss									
Sample Name:	**10CY-010**	**10CY-015**	**10CY-021**	**10CY-023**	**10CY-033**	**10CY-041**	**Y1-BB013**	**Y1-CB080**	**Y1-IG057**	**Y1-IG061**
wt %										
SiO_2	61.55	68.82	67.40	66.51	67.85	67.32	60.89	70.39	42.01	71.00
TiO_2	0.94	0.81	0.94	1.05	0.76	0.77	0.85	0.76	1.57	0.68
Al_2O_3	17.54	14.67	14.56	14.76	14.39	14.26	19.04	13.15	23.10	14.34
Fe_2O_3	1.32	1.24	0.76	1.06	1.36	1.08	1.21	0.67	3.89	0.94
FeO	6.05	4.55	5.50	5.87	4.21	4.61	5.87	5.04	12.78	4.34
MnO	0.09	0.05	0.07	0.08	0.08	0.05	0.07	0.08	0.44	0.09
MgO	3.71	2.76	3.26	3.59	2.74	2.89	3.90	3.00	7.74	2.45
CaO	0.91	0.82	1.31	0.71	1.37	1.75	0.93	1.75	0.43	1.17
Na_2O	1.91	1.64	1.81	0.99	2.03	2.55	1.33	1.85	0.37	1.43
K_2O	3.98	3.05	3.31	3.52	3.60	3.69	5.23	2.61	5.54	3.42
P_2O_5	0.13	0.06	0.14	0.08	0.13	0.14	0.15	0.19	0.15	0.19
LOI	2.21	1.77	1.50	1.90	1.85	1.18	2.65	1.69	3.49	2.22
Total	100.34	100.24	100.56	100.12	100.37	100.29	100.12	100.05	99.44	100.53
ASI	1.93	1.96	1.63	2.19	1.48	1.25	2.00	1.45	3.13	1.75
(FeO+MgO)	9.73	7.29	8.71	9.45	6.92	7.48	9.76	8.04	20.64	6.75
ppm										
Rb	276	247	198	228	201	188	299	141	394	176
Sr	106	66	133	80	126	161	135	152	18	157
Rb/Sr	2.6	3.7	1.5	2.9	1.6	1.2	2.2	0.9	21.9	1.1
Y	40	29	34	37	33	33	35	29	91	38
Zr	218	245	253	232	200	193	140	214	155	177
V	138	113	127	135	110	110	121	115	222	95
Ni	76	50	51	61	51	51	54	53	90	55
Cr	188	139	141	159	141	129	120	118	166	98
Nb	22	32	19	28	22	15	22	17	39	13
Ga	26	28	22	27	23	20	29	20	39	19
Cu	43	15	13	5	18	10	11	14	69	16
Zn	138	141	114	138	107	110	129	100	296	81
Co	28	21	22	27	20	20	23	22	51	18
Ba	682	306	399	373	428	456	901	427	262	822
La	28	28	28	32	22	26	28	26	16	25
Ce	74	57	65	75	54	54	72	68	53	60
U	3.4	5.6	1.2	2.6	3.8	2.3	2.3	2.1	1.2	2.6
Th	21	25	19	24	16	15	14	18	34	14
Sc	18	15	17	13	16	14	16	15	41	11
Pb	<1	<1	<1	<1	<1	<1	18	14	<1	14

Table 1: Continued

			Devonian-Carboniferous					
Rock Type:	**Paragneiss**		**Diatexite**		**Granite**			
Sample Name:	**Y1-LH077**	**Y1-MJ074**	**Y1-IG071**	**Y1-IG073**	**Y1-IG062**	**C5-I26**	**C6-AW86-1**	**M5-G175**
wt %								
SiO_2	69.59	68.37	72.88	71.63	75.60	65.27	75.85	67.54
TiO_2	0.76	0.74	0.46	0.48	0.01	0.55	0.08	0.70
Al_2O_3	13.58	15.71	13.91	14.62	13.97	16.07	13.47	15.23
Fe_2O_3	1.06	1.00	0.49	0.26	0.03	0.27	0.05	0.92
FeO	4.17	4.53	2.51	2.39	0.76	2.67	0.43	3.76
MnO	0.04	0.09	0.04	0.02	0.06	0.05	0.01	0.06
MgO	2.90	2.75	1.36	1.04	0.17	1.07	0.22	1.96
CaO	2.22	0.85	1.63	2.08	1.05	2.65	1.02	1.72
Na_2O	2.21	1.69	2.72	2.96	2.77	2.47	2.60	3.11
K_2O	2.89	3.92	4.16	4.00	5.80	6.85	5.93	4.14
P_2O_5	0.18	0.14	0.08	0.17	0.09	1.20	0.05	0.09
LOI	1.42	2.30	1.06	0.98	0.58	0.91	0.39	1.10
Total	100.06	100.29	100.52	99.92	100.39	99.42	99.76	99.65
ASI	1.26	1.83	1.16	1.13	1.10	0.99	1.07	1.20
(FeO+MgO)	6.75	6.75	3.85	3.43	0.93	3.75	0.65	5.73
ppm								
Rb	158	201	173	151	167	222	183	201
Sr	147	151	191	259	225	269	321	249
Rb/Sr	1.1	1.3	0.9	0.6	0.7	0.8	0.6	0.8
Y	32	31	26	22	27	89	3	39
Zr	215	166	169	255	76	295	122	233
V	103	105	57	51	<1	59	12	85
Ni	49	55	15	10	2	12	2	23
Cr	128	107	75	34	21	66	11	77
Nb	15	17	14	12	1	12	2	19
Ga	19	22	19	19	14	19	15	22
Cu	5.0	7.0	7	7	7	12	3	23
Zn	102	100	58	50	11	51	13	81
Co	18	19	8	6	<1	5	<1	15
Ba	459	875	551	1109	632	1533	803	1119
La	23	26	24	40	19	37	25	36
Ce	59	63	53	100	37	106	53	87
U	2.2	4.3	3.7	3.6	3.1	8.7	2.0	6.2
Th	17	11	12	22	3	11	7	17
Sc	14	14	8	8	4	10	<1	12
Pb	20	22	28	33	52	58	36	27

Table 1: Continued

	Cretaceous							
Rock Type:	**Granites**							**Microgranite**
Sample Name:	**10CY-039**	**Y1-AE051**	**Y1-IG052**	**Y1-IG070**	**Y1-AW038**	**Y1-AE033**	**Y1-AE064**	**10CY-024**
wt %								
SiO_2	73.95	76.08	75.33	77.50	71.16	74.06	75.01	74.25
TiO_2	0.04	0.02	0.02	0.01	0.03	0.10	0.04	0.28
Al_2O_3	14.85	14.62	14.17	13.85	16.02	15.58	14.64	13.99
Fe_2O_3	0.08	0.11	0.11	0.03	0.04	0.09	0.22	0.12
FeO	0.22	0.39	0.83	0.08	0.54	0.14	0.40	1.31
MnO	0.01	0.03	0.07	0.01	0.08	0.01	0.05	0.03
MgO	0.15	0.14	0.20	0.004	0.11	0.10	0.18	0.31
CaO	0.89	2.50	1.22	1.98	0.44	1.37	1.65	1.20
Na_2O	2.80	3.60	2.74	3.66	2.80	2.74	3.13	2.82
K_2O	6.81	2.84	5.43	3.21	8.89	5.91	5.15	5.34
P_2O_5	0.11	0.10	0.09	0.08	0.07	0.11	0.06	0.07
LOI	0.61	0.65	0.48	0.33	0.47	0.62	0.48	0.78
Total	99.93	100.47	100.30	100.42	100.24	100.23	100.57	99.87
ASI	1.09	1.08	1.12	1.06	1.07	1.16	1.07	1.11
(FeO+MgO)	0.37	0.53	1.03	0.08	0.65	0.24	0.58	1.62
ppm								
Rb	182	80	137	92	284	178	147	195
Sr	236	209	250	224	167	194	210	222
Rb/Sr	0.8	0.4	0.5	0.4	1.7	0.9	0.7	0.9
Y	5	15	16	4	15	9	10	34
Zr	39	56	57	28	76	23	73	227
V	5	1	6	1	5	8	6	23
Ni	6	2	2	1	1	1	3	1
Cr	35	33	18	19	14	8	21	4
Nb	2	1	1	1	2	2	2	15
Ga	15	17	14	16	15	19	16	20
Cu	4	2	7	25	4	3	4	7
Zn	11	9	10	7	13	10	13	27
Co	<1	<1	<1	<1	<1	<1	<1	2
Ba	895	402	1073	434	457	640	515	834
La	11	19	17	13	15	21	26	48
Ce	13	23	20	17	13	28	39	108
U	1.1	3.0	<0.5	1.1	1.4	1.4	1.7	2.4
Th	<0.5	<0.5	<0.5	<0.5	<0.5	<0.5	6	36
Sc	<1	4	3	1	3	1	2	3
Pb	65	46	62	43	64	58	47	29

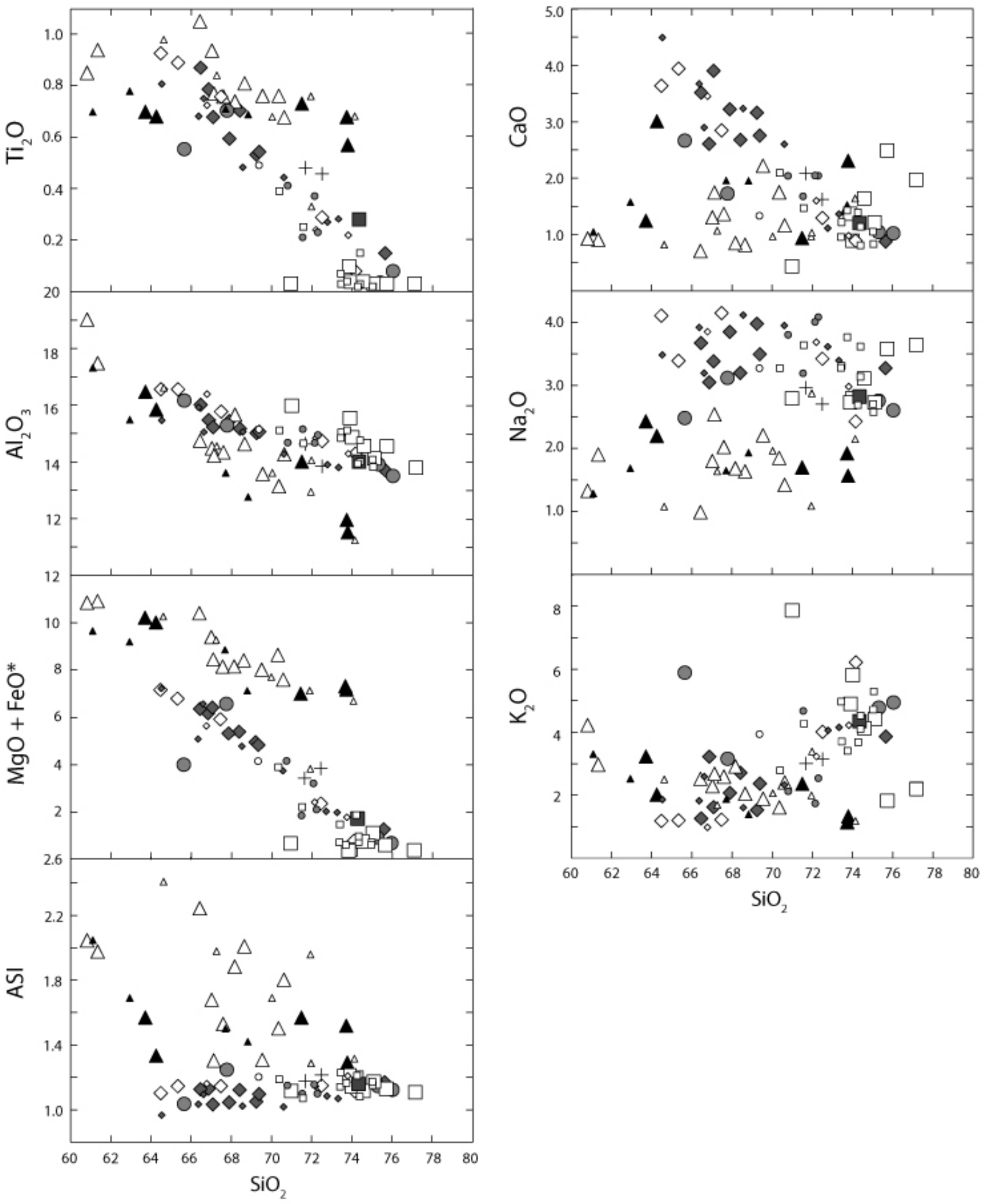

Figure 2: Select major and trace element data for samples as determined by XRF. Ford Granodiorite samples include data from Korhonen *et al.* (2010b), Weaver *et al.* (1992), and Pankhurst *et al.* (1998). FeO* represents total ferrous iron. Aluminum saturation index (ASI) = molar [Al_2O_3 / CaO + Na_2O + K_2O]. Graphs of oxides are plotted as weight percent while trace elements are plotted as parts per million (ppm).

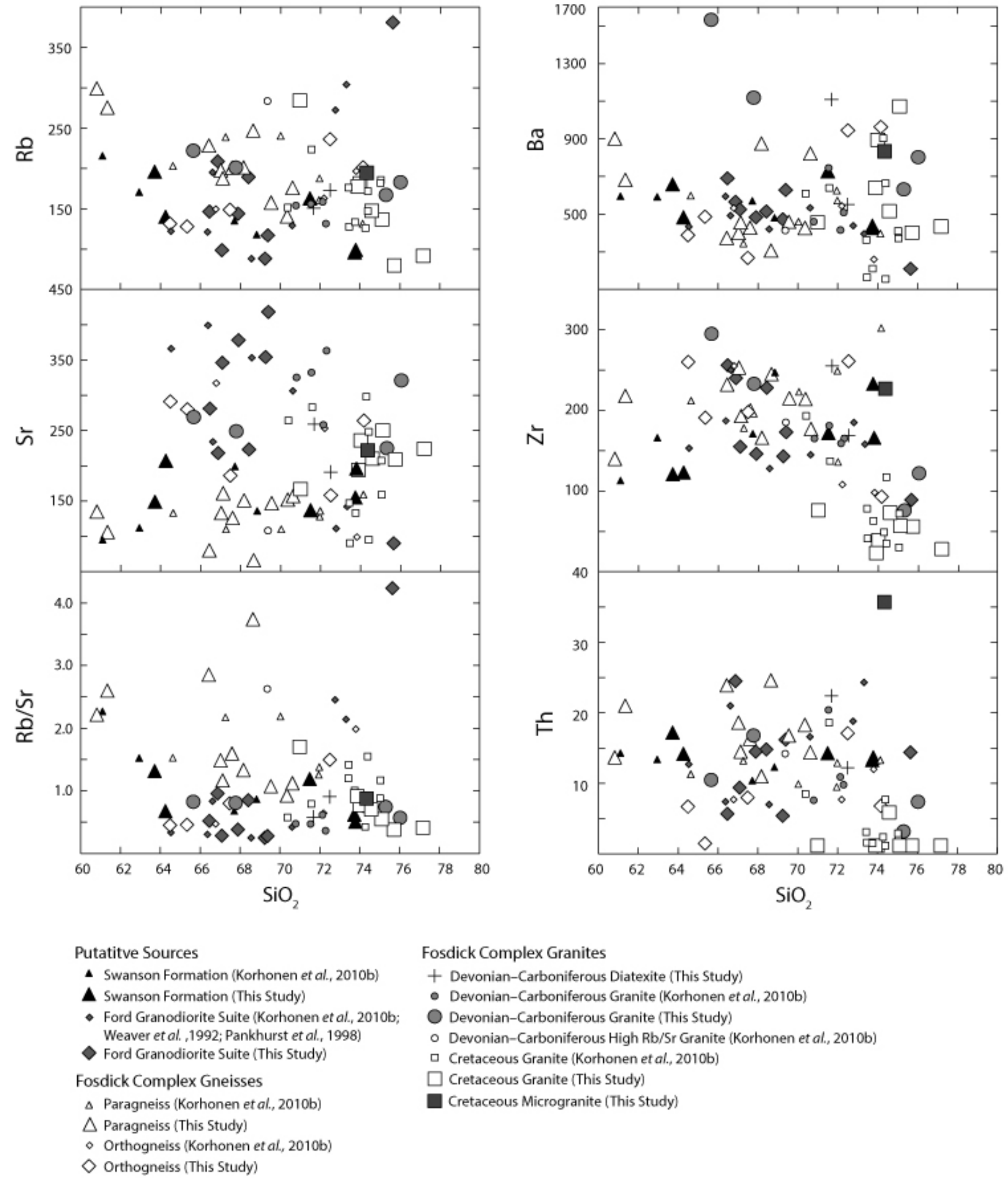

Figure 2: Continued

Table 2: Rare earth element (REE) compositions as determined by SC-ICP-MS

Rock Type:	**Swanson Formation**					**Ford Granodiorite Suite**			
Sample Name:	**10CY-001**	**10CY-002**	**Y2-BR086**	**Y2-MD092**	**Y2-MP098**	**51225-1**	**51225-2**	**Y2-GP091**	**Y2-HN097**
Sc	18.2	17.3	11.2	9.8	10.4	10.9	11.3	8.64	8.72
Y	28.6	30.4	38.9	27.0	31.3	34.5	33.8	20.9	19.0
La	32.3	37.3	42.9	32.7	36.7	48.0	53.2	25.0	21.0
Ce	66.6	76.4	90.1	66.7	75.0	103	114	50.1	41.6
Pr	7.83	8.84	10.60	7.92	8.97	12.8	14.1	6.16	5.04
Nd	30.0	34.2	40.3	30.3	34.2	48.3	52.7	23.3	19.3
Sm	6.25	6.96	8.43	6.10	6.92	8.97	9.47	4.65	3.93
Eu	1.34	1.44	1.65	1.18	1.29	1.38	1.34	1.06	0.94
Gd	5.05	5.52	6.95	4.89	5.47	7.53	7.59	4.21	3.65
Tb	0.85	0.91	1.20	0.81	0.93	1.17	1.18	0.69	0.61
Dy	5.03	5.26	7.03	4.75	5.50	6.31	6.48	3.90	3.45
Ho	1.03	1.07	1.41	0.96	1.14	1.19	1.22	0.74	0.67
Er	2.89	3.01	3.83	2.65	3.17	3.51	3.63	2.21	1.99
Tm	0.43	0.43	0.55	0.39	0.47	0.55	0.58	0.36	0.32
Yb	2.81	2.86	3.45	2.43	3.03	3.39	3.59	2.38	2.03
Lu	0.39	0.40	0.45	0.33	0.42	0.52	0.56	0.39	0.32
Eu/Eu*	0.70	0.68	0.64	0.64	0.62	0.50	0.47	0.72	0.74
Tb_N/Lu_N	1.50	1.54	1.82	1.67	1.53	1.53	1.44	1.22	1.29
La_N/Lu_N	8.64	9.61	9.94	10.2	9.18	8.64	9.61	9.94	10.2

Rock Type:	**Ford Granodiorite Suite**				**Orthogneiss**				
Sample Name:	**Y2-JU096**	**Y2-MS089**	**Y2-SM095**	**Y1-AE035**	**10CY-035**	**Y1-AW049**	**Y1-AW039**	**Y1-IG053**	**Y1-MJ075**
Sc	9.59	3.83	11.4	15.8	1.46	14.8	13.9	14.8	5.0
Y	30.7	33.5	22.4	25.8	7.83	15.7	33.7	26.0	14.4
La	40.5	16.8	22.4	43.7	14.7	43.5	33.4	24.5	93.4
Ce	82.6	37.4	49.0	91.8	30.1	89.2	70.3	52.5	169
Pr	10.0	4.83	6.05	11.3	3.74	10.6	8.94	6.89	18.2
Nd	37.4	17.5	23.1	44.5	13.8	38.3	34.8	27.7	60.3
Sm	6.91	4.12	4.63	8.37	2.95	6.55	7.56	5.82	8.73
Eu	1.39	0.42	1.16	1.76	1.35	1.28	1.28	1.63	1.10
Gd	6.02	4.09	4.30	6.83	2.45	5.44	7.09	5.52	5.97
Tb	0.97	0.82	0.70	1.05	0.37	0.77	1.23	0.95	0.83
Dy	5.34	5.10	3.94	5.38	1.71	3.67	6.76	5.33	3.61
Ho	1.03	1.05	0.77	0.95	0.28	0.61	1.22	0.98	0.50
Er	3.06	3.47	2.27	2.54	0.73	1.46	3.38	2.63	1.04
Tm	0.49	0.63	0.36	0.37	0.11	0.19	0.52	0.36	0.12
Yb	3.09	4.54	2.29	2.19	0.73	1.07	3.10	2.01	0.63
Lu	0.49	0.77	0.37	0.33	0.12	0.17	0.45	0.29	0.08
Eu/Eu*	0.64	0.31	0.78	0.69	1.48	0.63	0.52	0.52	0.44
Tb_N/Lu_N	1.35	0.73	1.30	2.19	2.04	3.17	1.86	1.86	6.84
La_N/Lu_N	8.60	2.27	6.34	13.9	12.4	27.3	7.68	7.68	117

Rock Type:	**Paragneiss**								
Sample Name:	**10CY-010**	**10CY-015**	**10CY-023**	**10CY-033**	**10CY-041**	**Y1-BB013**	**Y1-CB080**	**Y1-IG057**	**Y1-IG061**
Sc	18.4	13.8	16.7	13.6	14.2	16.6	13.4	58.2	12.6
Y	40.5	34.4	45.2	28.0	34.4	23.9	25.9	99.2	34.3
La	57.1	47.8	68.7	43.9	35.6	41.5	48.6	68.0	28.1
Ce	114	97.0	140	91.1	72.74	83.7	98.4	138	57.9
Pr	13.4	11.3	16.5	10.7	8.72	9.58	11.45	16.23	6.87
Nd	51.6	43.1	63.2	40.6	33.1	37.5	44.0	60.7	26.6
Sm	10.3	8.72	12.8	7.96	6.89	7.61	8.56	11.96	5.54
Eu	1.60	0.98	1.09	1.13	1.22	1.41	1.31	0.63	1.53
Gd	8.07	6.66	9.31	5.79	5.65	5.75	6.35	10.06	4.62
Tb	1.33	1.11	1.45	0.94	0.99	0.90	0.98	2.16	0.84
Dy	7.36	6.11	8.19	5.21	5.90	4.76	5.19	16.04	5.41
Ho	1.47	1.17	1.66	0.99	1.23	0.87	0.93	3.58	1.20
Er	3.90	3.07	4.70	2.56	3.43	2.12	2.24	9.84	3.55
Tm	0.55	0.43	0.70	0.36	0.50	0.27	0.29	1.40	0.54
Yb	3.31	2.64	4.47	2.17	3.14	1.56	1.73	8.36	3.48
Lu	0.43	0.35	0.62	0.28	0.43	0.20	0.23	1.09	0.46
Eu/Eu*	0.51	0.38	0.29	0.48	0.58	0.62	0.52	0.17	0.90
Tb_N/Lu_N	2.09	2.17	1.60	2.30	1.58	3.07	2.94	1.35	1.24
La_N/Lu_N	13.7	14.3	11.5	16.3	8.66	21.5	22.2	6.48	6.31

Table 2: Continued

			Devonian-Carboniferous					
Rock Type:	**Paragneiss**		**Diatexite**		**Granite**			
Sample Name:	**Y1-LH077**	**Y1-MJ074**	**Y1-IG071**	**Y1-IG073**	**Y1-IG062**	**C5-I26**	**C6-AW86-1**	**M5-G175**
Sc	12.5	10.9	10.3	7.97	7.32	9.78	1.11	14.0
Y	31.5	21.8	17.7	22.5	24.9	103	3.50	35.9
La	45.0	35.9	31.5	63.8	14.3	61.4	27.6	58.0
Ce	91.9	72.7	65.7	132	30.0	137	55.4	115
Pr	10.8	8.57	8.16	16.0	3.79	18.1	6.87	13.7
Nd	41.6	33.2	29.8	61.0	13.8	72.7	24.9	50.1
Sm	8.38	6.66	6.0	11.1	3.20	17.1	4.54	8.94
Eu	1.58	1.34	1.18	1.74	1.13	2.25	0.98	1.53
Gd	6.54	4.97	4.92	8.65	2.77	18.1	3.25	7.82
Tb	1.06	0.78	0.79	1.24	0.52	3.48	0.34	1.19
Dy	5.84	4.21	3.88	5.83	3.51	20.3	1.12	6.25
Ho	1.11	0.79	0.64	0.87	0.86	3.61	0.13	1.19
Er	2.82	2.04	1.56	1.91	3.31	9.57	0.26	3.50
Tm	0.37	0.29	0.20	0.21	0.65	1.35	0.03	0.53
Yb	2.18	1.74	1.10	0.96	4.95	7.07	0.21	3.10
Lu	0.28	0.23	0.15	0.12	0.84	0.94	0.03	0.48
Eu/Eu*	0.63	0.68	0.64	0.52	1.13	0.39	0.74	0.54
Tb_N/Lu_N	2.54	2.29	3.52	7.27	0.42	2.51	6.79	1.69
La_N/Lu_N	16.5	16.0	21.5	57.1	1.77	6.76	82.6	12.5

	Cretaceous							
Rock Type:	**Granites**							**Microgranite**
Sample Name:	**10CY-039**	**Y1-AE051**	**Y1-IG052**	**Y1-IG070**	**Y1-AW038**	**Y1-AE033**	**Y1-AE064**	**10CY-024**
Sc	0.79	4.51	6.40	0.51	3.57	1.04	3.96	3.80
Y	5.63	12.7	17.8	2.95	10.9	9.77	11.9	35.4
La	6.12	7.79	11.1	4.34	1.87	15.2	20.1	66.2
Ce	11.1	13.2	20.1	7.14	2.45	31.3	40.7	141
Pr	1.28	1.48	2.32	0.76	0.24	3.90	4.86	17.1
Nd	4.54	5.06	8.13	2.43	0.75	14.4	17.3	62.7
Sm	0.99	1.04	1.48	0.45	0.23	3.26	3.33	11.0
Eu	1.32	1.44	1.58	1.13	0.60	1.49	1.16	1.22
Gd	0.94	0.99	1.33	0.41	0.41	2.93	2.54	8.33
Tb	0.18	0.22	0.31	0.08	0.13	0.47	0.39	1.25
Dy	1.00	1.70	2.51	0.47	1.21	2.17	2.10	6.65
Ho	0.19	0.45	0.61	0.10	0.35	0.33	0.41	1.26
Er	0.52	1.73	2.30	0.33	1.51	0.79	1.43	3.68
Tm	0.08	0.33	0.48	0.06	0.34	0.10	0.30	0.56
Yb	0.45	2.36	3.80	0.45	2.87	0.57	2.51	3.38
Lu	0.07	0.39	0.62	0.08	0.53	0.08	0.46	0.52
Eu/Eu*	4.10	4.24	3.35	7.91	5.88	1.44	1.17	0.37
Tb_N/Lu_N	1.73	0.37	0.33	0.68	0.17	4.01	0.58	1.63
La_N/Lu_N	9.14	2.05	1.85	5.88	0.36	19.9	4.56	13.1

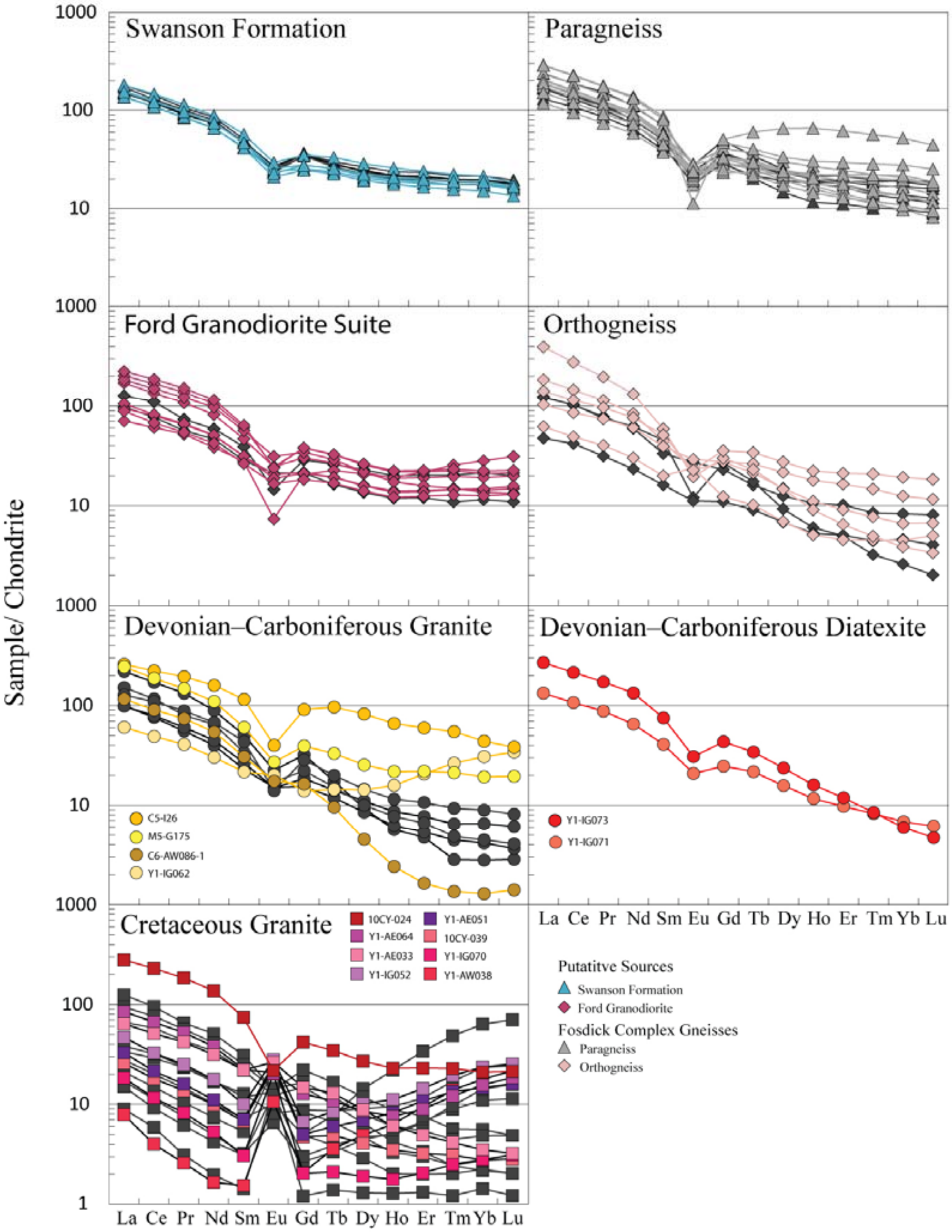

Figure 3: Rare earth element (REE) chondrite-normalized patterns for source rocks and granites. Data from Korhonen *et al.* (2010b) are given as black symbols for comparison.

6.3 Major and trace element discussion

Granite may not represent direct melts of their sources, which could account for differences in their chemical compositions when compared with their putative sources. In order to determine whether or not the granites analyzed represent direct melts of the Swanson Formation or the Ford Granodiorite suite, the compositional variability of Carboniferous and Cretaceous granites was investigated using the ternary system (Na+Ca)–(Fe*+Mg+Ti)–K (after Solar and Brown, 2001). Because there have been no melting experiments done on the either the Swanson Formation or the Ford Granodiorite suite, experimental melt compositions from Skjerlie *et al.* (1993), Patiño-Douce and Harris (1998) and Koester *et al.*, (2002) were used based on similarity of the chemical composition of their starting material to the putative sources. The starting material and melt compositions from Skjerlie *et al.* (1993), Patiño-Douce and Harris (1998) and Koester *et al.*, (2002) are plotted along with samples from the Swanson Formation, Ford Granodiorite suite, their high-grade equivalents, and Devonian–Carboniferous and Cretaceous granites in Figure 4. The experimental melts from Skjerlie *et al.* (1993) were used as proxies for the Ford Granodiorite suite melt composition while the experimental results of Patiño-Douce and Harris (1998) and Koester *et al.* (2002) were used to infer melt compositions of the Swanson Formation and the paragneiss samples, respectively. Select mineral composition are also plotted on the ternary diagram.

Paragneiss samples generally fall within the same major and trace element compositional field as the Swanson Formation with sample Y1-IG057 plotting close to the biotite (Fig. 4), consistent with this sample h as indicated by the elevated Rb/Sr ratio and biotite-rich mineral assemblage. Paragneisses have major and trace element compositions and REE patterns that are very similar to the Swanson Formation. Orthogneiss samples generally fall within the compositional field as the Ford Granodiorite suite (Fig. 4) and have major and trace element compositions and REE patterns that are very similar to the Ford Granodiorite suite (Figs 2 and 3). Samples 10CY-035 and Y1-MJ075 are exceptions. Both samples are displaced toward the potassium apex indicating slightly more evolved compositions (Fig. 4). Samples Y1-MJ075 and 10CY-035 have higher K and Ba content than the Ford Granodiorite suite, consistent with the accumulation of plagioclase and potassium feldspar during crystallization. Sample 10CY-035 also has a positive Eu anomaly, consistent with the sample being a cumulate.

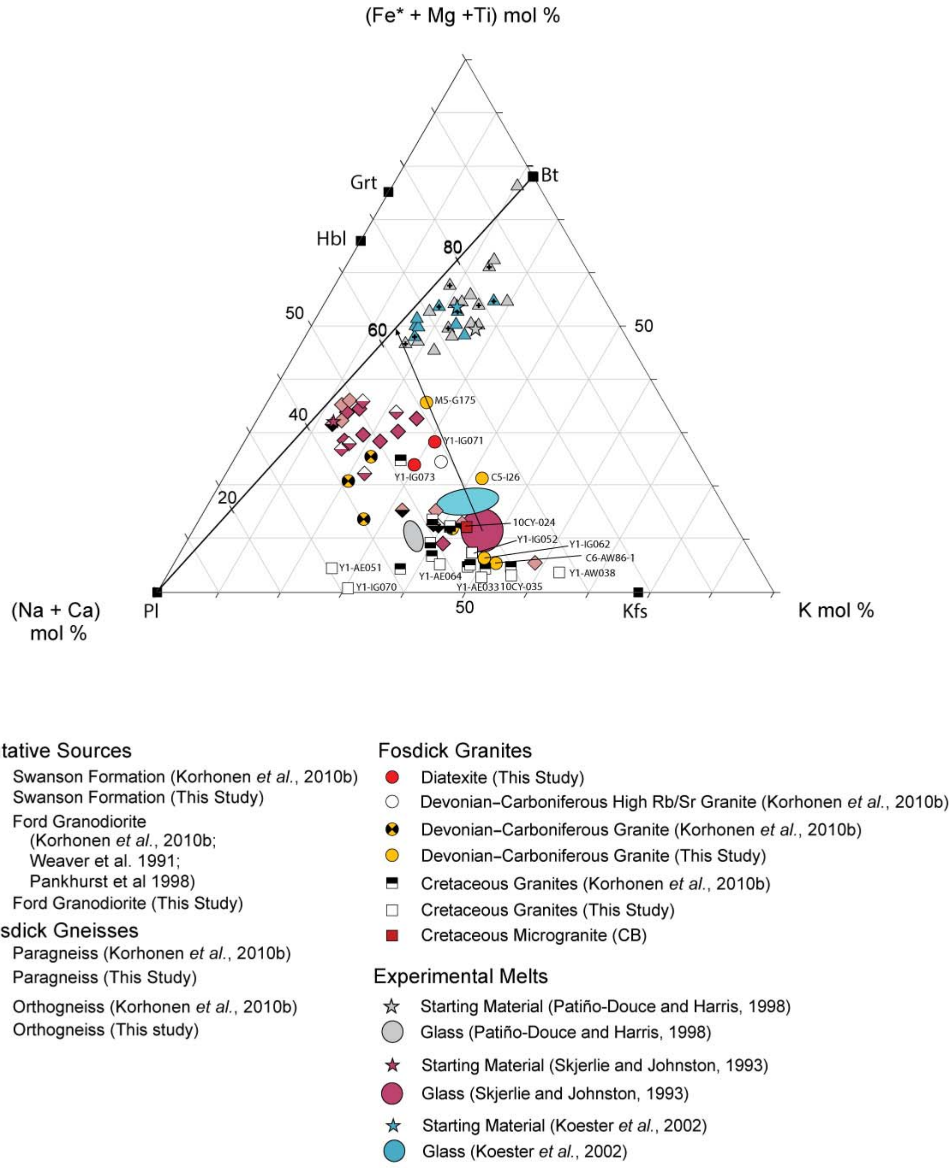

Figure 4: Ternary (Na+Ca)–(Fe*+Mg+Ti)–K (after Solar and Brown, 2001). The arrow from glass (Skjerlie *et al.*, 1993) through M5-G175 tracks model cumulate and fractionated melt trend. This granite would represent ~65% cumulate composed of 63% biotite and 37% plagioclase

Devonian–Carboniferous granites Y1-IG062, C6-AW86-1, C5-I26, M5-G175 and diatexites Y1-IG073 and Y1-IG071 have major and trace element compositions that are consistent with them being derived from or having a component of the Ford Granodiorite suite (Figs 2 and 3). However, none of these samples fall within the field defined by experimental melt compositions resulting from melting of the Ford Granodiorite suite (Fig. 4). Instead, they can be described as cumulates. By projecting from the melt composition through the granite composition, it is possible to determine the amount of cumulate material and the proportion of minerals needed to produce a granite of that composition (e.g., Solar and Brown, 2001; Korhonen *et al.*, 2010b). Sample M5-G175 could reflect a Ford Granodiorite suite melt with ~65% cumulate composed of ~63% biotite and ~37% plagioclase (Fig. 4). Sample C5-I26 can be modeled as a ~15% cumulate derived from the Ford Granodiorite suite composed of ~87% biotite and ~13% plagioclase. Sample Y1-IG073 can be modeled as ~45% cumulate composed of ~35% biotite and ~65% plagioclase while sample Y1-IG071 as ~50% cumulate composed of ~60% biotite and ~40% plagioclase. Samples Y1-IG062 and C6-AW086-1 plot closer to the Na–Ca and K tie line than the melt composition, which suggests that they have either lost residual ferromagnesian minerals (biotite or garnet) or that they contain early crystallized (cumulate) feldspar. Sample Y1-IG062 could represent a cumulate composed of 25% biotite and 60% K-feldspar and 40% plagioclase, which could account for the slight positive Eu anomaly. Sample C6-AW086-1 could represent 25% cumulate composed of 70% K-feldspar and 30% plagioclase. Because samples Y1-IG062 and C6-AW86-1 lie close to the K-feldspar–plagioclase feldspar tie line, there is more uncertainty in estimating the proportion of cumulate minerals.

Cretaceous granites also do not fall within the melt compositions of the Swanson Formation or the Ford Granodiorite suite. They all have positive Eu anomalies, indicating that they could be cumulates of early crystallizing feldspars. Samples 10CY-039, Y1-AW038, Y1-IG052 and Y1-AE064 are have major and trace element compositions similar to the Ford Granodiorite suite. The major element compositions of these samples are displaced towards the K-feldspar–plagioclase tie line relative to the experimental melt compositions. Projecting from the melt composition through each sample to the K-feldspar–plagioclase join (Fig. 4), the amount and composition of cumulate can be calculated. 10CY-039 can be modeled as ~60% cumulate composed of ~87% K-feldspar and ~13% plagioclase. Y1-AW038 can be modeled as ~70% cumulate composed of ~75% K-feldspar and ~25% plagioclase. Y1-IG052 could represent the lowest amount of cumulate at ~50% cumulate composed of ~52% K-feldspar and ~48% plagioclase. Y1-AE064 could represent ~50% cumulate composed of ~50% K-feldspar and ~50% plagioclase. Y1-AE033 can be modeled as ~80% cumulate composed of ~64% K-feldspar and ~36% plagioclase. Y1-IG070 lies closest to the plagioclase and K-feldspar tie line It can be modeled as >80% cumulate composed of ~65% plagioclase and ~35% K-feldspar. This sample also has the strongest positive Eu anomaly, consistent with containing a lot of cumulate feldspar. As with two of the Devonian–Carboniferous granites, there is large uncertainty on estimating the proportion of cumulate in the Cretaceous samples as they lie so close the feldspar tie-line.

Because these granites aren't melt compositions, the behavior of major and accessory minerals during partial melting may have a strong impact on the chemical and isotope composition of the granite. Certain minerals are more likely to affect the chemical and isotopic composition of a melt more strongly than others. Trace elements such as Rb and Sr are controlled primarily major rock-forming minerals. Strontium ratios are controlled by the growth or breakdown of major rock-forming minerals rich in Rb and Sr (e.g., micas and plagioclase); the stability of these minerals is primarily controlled by temperature, pressure, water content during melting. Rb is incorporated into the K site in biotite while Sr can be found in the Ca site of plagioclases. Therefore, melting reactions that involve micas will increase the ^{87}Sr/^{86}Sr ratio of the melt, while the breakdown of plagioclase during melting will decrease the ^{87}Sr/^{86}Sr ratio (Farina and Stevens, 2011). In the Fosdick complex, >10 vol. % melt is expected to be generated at temperatures above biotite stability for Ford Granodiorite suite compositions (>850°C; Korhonen *et al.*, 2010a). Melt derived from this source generally has low Rb/Sr, consistent with the breakdown of plagioclase and hornblende. Melts derived from the Swanson Formation would be expected to have high Rb/Sr and high ^{87}Sr/^{86}Sr due to the prevalence of biotite in the source and melting conditions that involve the break-down of biotite (Korhonen *et al.*, 2010a).

Unlike Sr isotope signatures, which are controlled by the growth and breakdown of major minerals, REEs and Nd isotope ratios are mainly controlled by the behavior of accessory minerals during partial melting. Minerals such as zircon, apatite, monazite and xenotime contain more than 80–90% of the REE, Zr Y, U, and

Th budget in granites and migmatites (Ayres and Harris, 1997). Zircon and xenotime have negligible amounts of Sm and Nd when compared with monazite and apatite. The REE-rich minerals will have a large influence on the REE budget of a melt and, therefore, will have a large effect on the Nd isotopic signature of the melt. Their dissolution into the melt is largely controlled by water content and composition of the melt, temperature and pressure at which melt is produced, and whether the minerals are sequestered from melt in other minerals. If the melt is saturated in REE and P_2O_5, dissolution of apatite and monazite is inhibited (Patiño-Douce and Harris, 1998; Rapp and Watson, 1986). Hot and dry conditions promote apatite dissolution whereas wetter and lower temperature conditions favor the dissolution of monazite. Apatite will generally contribute ~10% of LREE, 50% of MREE, and >90% HREE to the melt (Ayres and Harris, 1997). Therefore melt with a large contribution of apatite relative to monazite will show an increase in P_2O_5, a large Sm/Nd fractionation signature, a more radiogenic εNd value, and a depleted LREE signature compared with the putative source (Zeng *et al.*, 2005a, 2005b). However, because apatite and monazite can occur as inclusions in other minerals, such as biotite, the availability of these minerals can be strongly dependent on the breakdown of the host mineral, which is frequently biotite. Wetter conditions will promote biotite stability, so even though the conditions may be favorable for monazite dissolution, biotite stability may prevent the inclusions from reacting with the melt and affecting the Nd signature. If biotite is residual, and accessory minerals are sequestered away in biotite, then the melt will be depleted in REE compared with the source (Bea, 1996; Watt and Harley, 1993; Rapp and Watson, 1986). Understanding the behavior major rock forming minerals and accessory minerals is necessary in understanding the REE patterns and isotope compositions of the granites.

6.4 Modeling REE patterns of a Cretaceous granite

Although the REE patterns of the granites are consistent with crustal source, it is necessary to determine if one of the putative sources could produce a REE pattern that matches one of the granites. To determine if the Ford Granodiorite suite could produce one of the granites, batch melting and fractional crystallization of the Ford Granodiorite suite was modeled. Sample Y1-IG070, a Cretaceous granite, was used to compare against the model. This sample has the largest positive Eu anomaly (Eu/Eu* = 7.91) of the Cretaceous granites and can be used to determine if melting of the Ford Granodiorite suite and subsequent crystallization can produce a REE pattern with a positive Eu anomaly of similar magnitude. This sample also has no visible accessory phases, so uncertainties in estimating modal abundances of accessory minerals can be minimized to estimates of accessory minerals in the source.

Melting of the Ford Granodiorite was modeled using the modal abundance of Y2-HN097 (Table ___) because it has the most plagioclase and could add enough Eu to the melt to produce a large Eu anomaly in a granite if the Eu is sequestered in early crystallizing feldspars. The model uses average REE concentrations from all Ford Granodiorite samples. Batch melting was modeled first using the batch melting equation:

$C_L/C_O = 1/(F + (1-F)*D)$ where C_L is the concentration of a given element in the melt, C_O is the concentration of a given element in the whole system, D is the bulk distribution coefficient, and F is the fraction of melt produced. Minerals that were used to calculate the bulk distribution coefficient were limited by available mineral partition coefficients for peraluminous granites. Minerals used to calculate the bulk distribution coefficients were biotite, plagioclase, K-feldspar, apatite and zircon. Partition coefficients (Kds) that were used are listed in Table ____. Fractional crystallization of the melt was modeled second. The fractional crystallization model used the 5% melt composition determined by the batch melting model. This is approximately the same amount of melt that the Ford Granodiorite suite would have produce at the *P–T* conditions during the Cretaceous melting event (Korhonen *et al.*, 2010a). Fractional crystallization of this melt was modeled using the equation: $C_L/C_O = F^{(D-1)}$.

Table 3: Modal abundances and Kds of select minerals from sample Y2-HN097 used in REE modeling

	Biotite	Plagioclase	K-feldspar	Quartz	Hornblende	Apatite	Zircon
Modal Abundances	0.17	0.5	0.11	0.16	0.05	0.005	0.005
Kd*							
La	0.06	4.61	1.01			456	1.3
Ce	0.05	3.87	0.86			569	2.04
Pr	0.07	4.22	0.87			764	2.54
Nd	0.08	2.56	0.51			855	3.35
Sm	0.06	1.45	0.42			1105	3.79
Eu	0.05	2.99	2.32			23.8	0.45
Gd	0.1	2.05	0.6			2133	9.21
Tb	0.18	2.93	0.92			3643	24.8
Dy	0.17	1.94	0.77			3257	38.8
Ho	0.16	1.8	0.88			3143	74.5
Er	0.22	1.94	1.14			4231	165
Tm	0.22	1.63	1.12			3769	282
Yb	0.12	0.82	0.64			2216	278
Lu	0.2	1.32	0.96			2981	923

*Bea, 1994

If the modal proportions of apatite and zircon are not considered, different proportions of melting do not change the REE pattern relative to the average Ford Granodiorite patterns. The REE pattern only changes when accessory phases are considered. Figures 5–8 presents the REE pattern of melting the Ford Granodiorite with 5%, 10%, 20%, 50% and 90% melt when apatite and zircon modal abundances in the source are 0%, 0.25%, 0.5%, and 1%. Figures 5–8 also presents the REE patterns of 10%, 30%, 50%, and 80% fractional crystallization of 5% batch melting of Ford Granodiorite suite. Results indicate that it is possible to produce a Eu anomaly of similar magnitude to Y1-IG070 from melting of the Ford Granodiorite suite that has 0.5% modal abundance of apatite and zircon and 80% fractional crystallization. This percentage of crystallization is similar to the proportion of cumulate determined from Figure 4. The closest match to the Eu anomaly in Y1-IG070 comes from a source that has 1% modal abundance of apatite and zircon and 80% cumulate. However, this is an unrealistic modal abundance of apatite and zircon for the Ford Granodiorite suite.

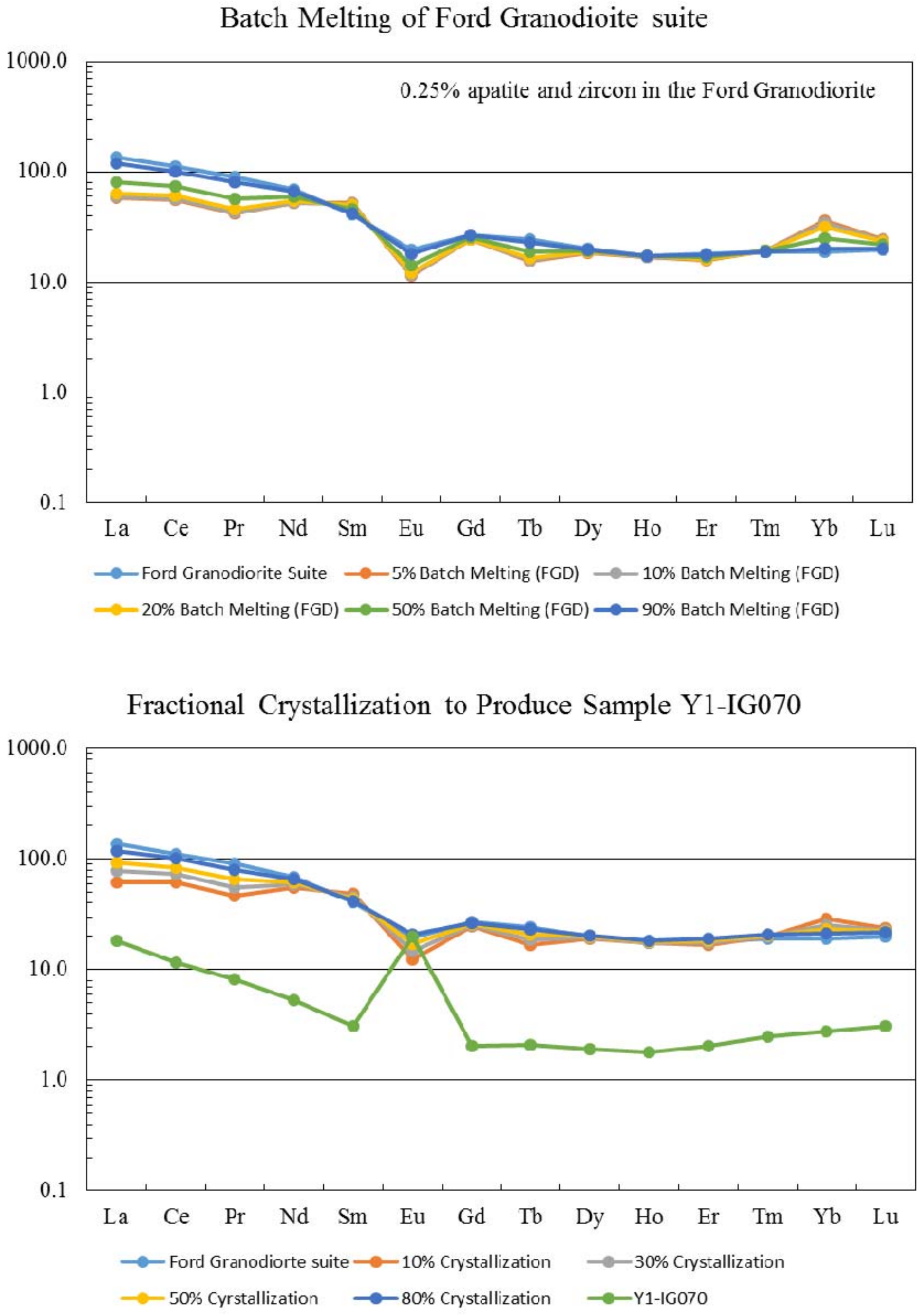

Figure 5: Model of batch melting and fractional crystallization with 0% apatite and zircon in the source material

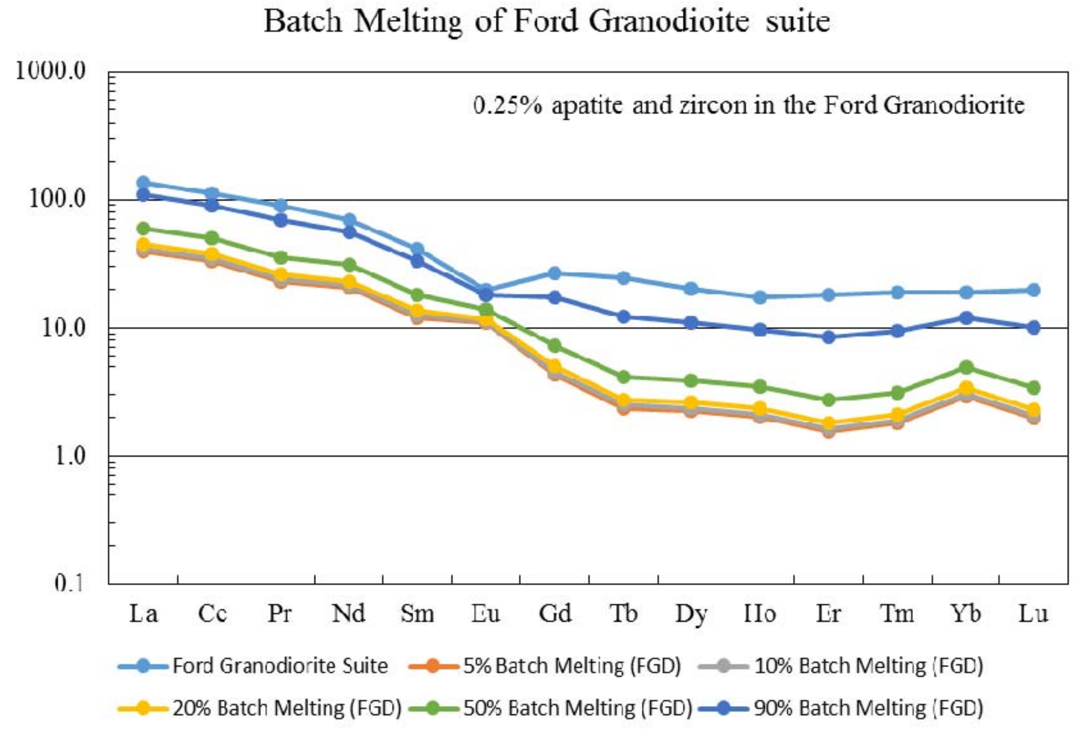

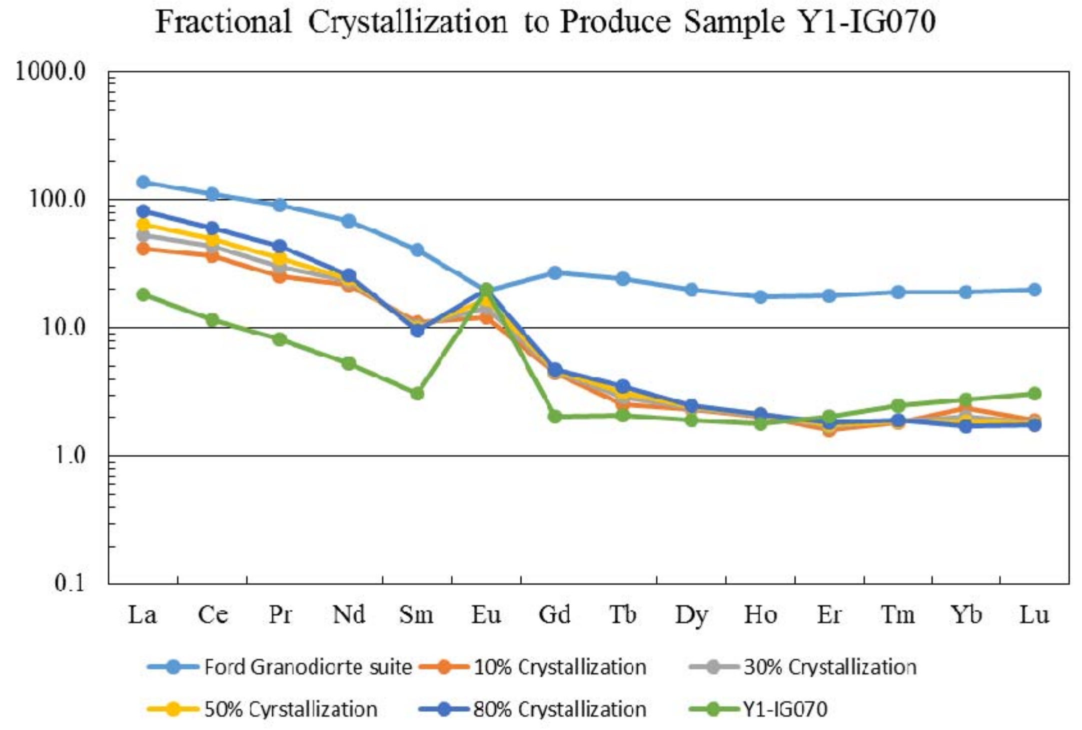

Figure 6: Model of batch melting and fractional crystallization with 0.25% apatite and zircon in the source material

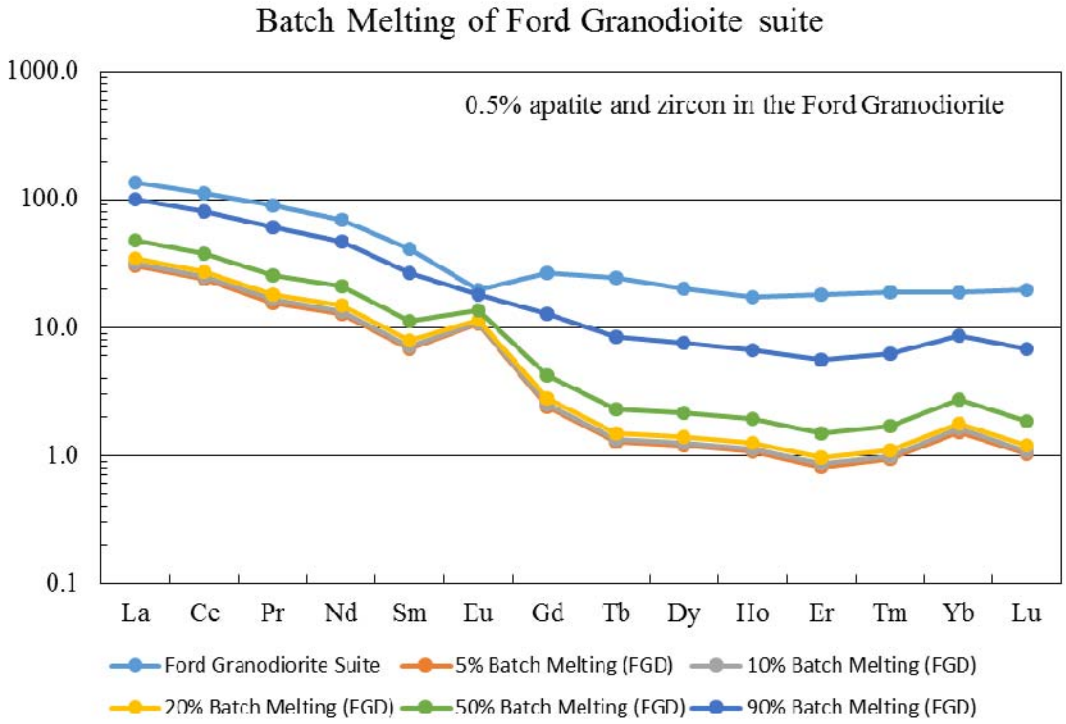

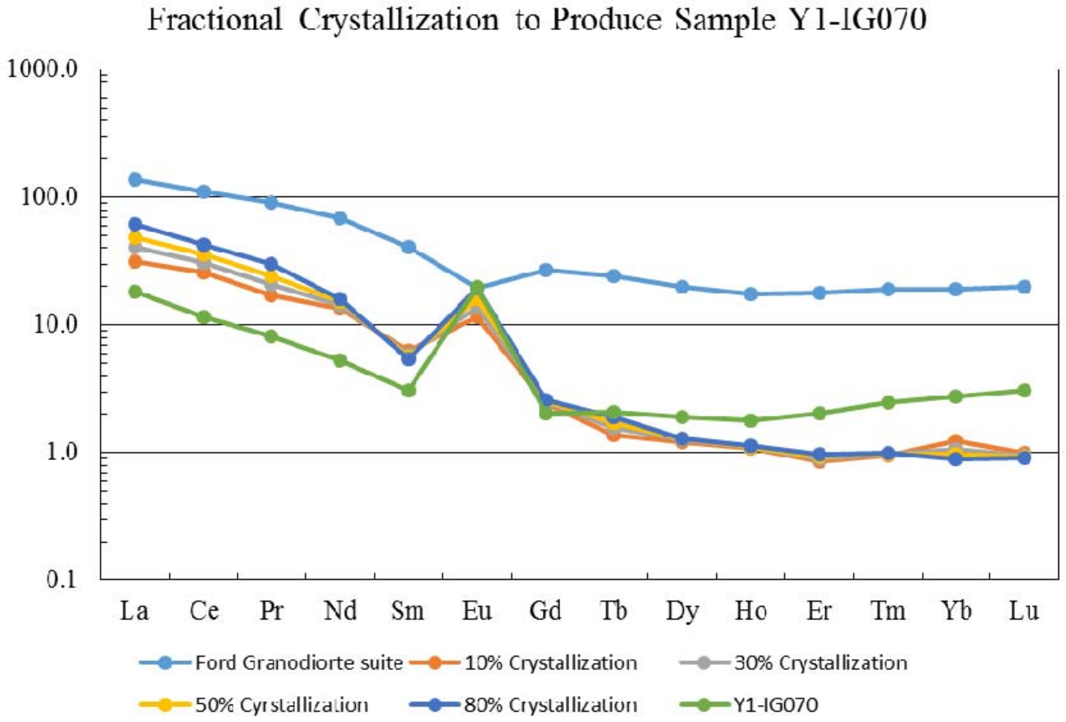

Figure 7: Model of batch melting and fractional crystallization with 0.5% apatite and zircon in the source material

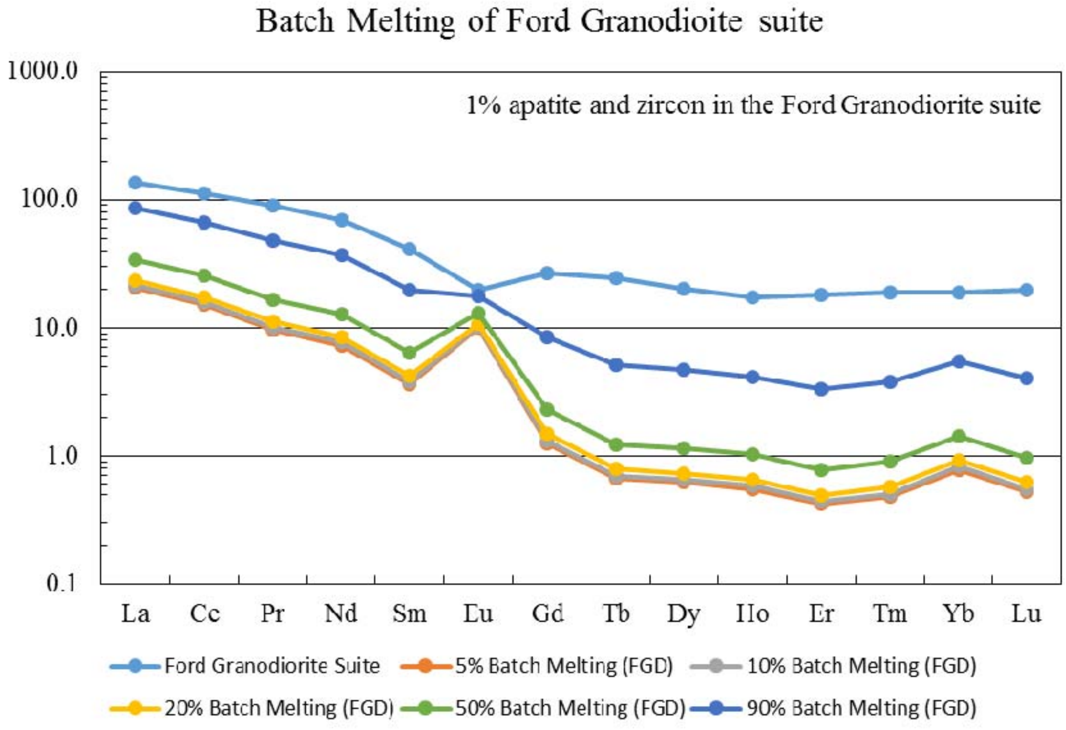

Batch Melting of Ford Granodioite suite

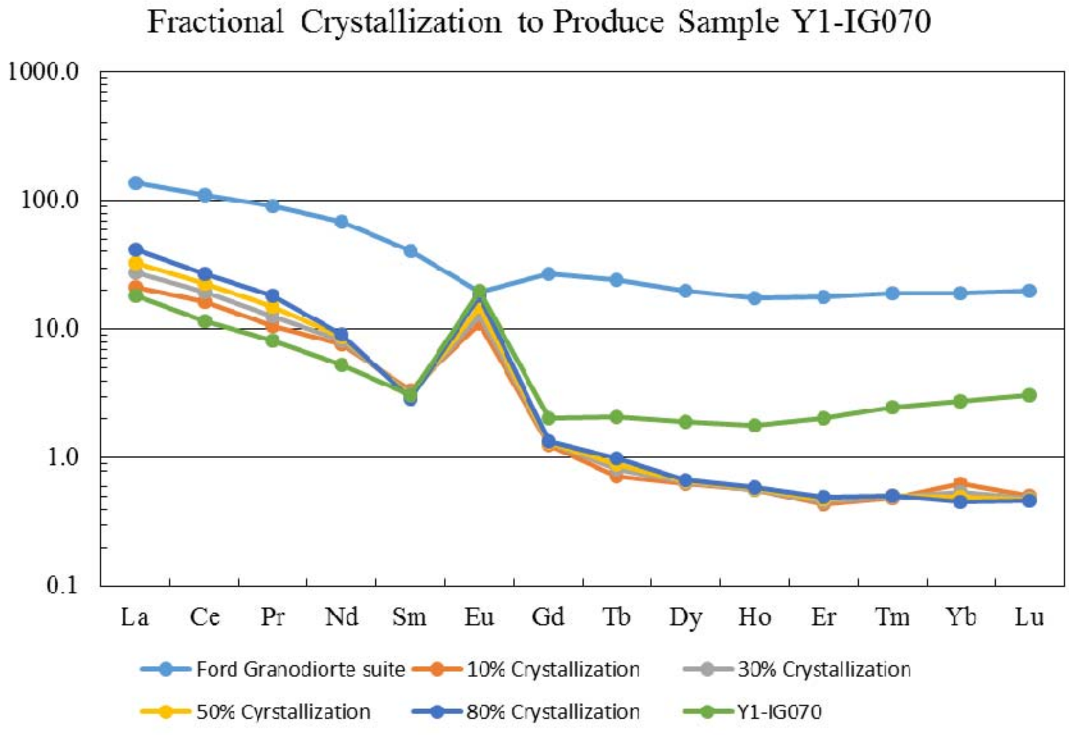

Fractional Crystallization to Produce Sample Y1-IG070

Figure 8: Model of batch melting and fractional crystallization with 1% apatite and zircon in the source material

Although the model closely match the positive Eu anomaly seen in sample Y1-IG070, there are differences in the modeled REE pattern when compared with the REE pattern of sample Y1-IG070. The LREE concentrations are lower in the sample than in the model and the HREE are higher in the sample than in the model. This could be due to basic assumptions of the model, such as equilibrium melting. However, for melt abundances less than 7%, equilibrium melting may be a reasonable assumption. The model also does not account for monazite in the source because REEs are essential structural elements. Their behavior is non-Henrian and therefore, partition coefficients are not constant. This makes modeling the behavior of monazite during melting difficult. It is possible that monazite remained in the source during melting, causing a depletion in LREE seen in the sample, but, because monazite was not considered in bulk distribution coefficients, the LREE depletion is not seen in the model. It is also possible that this sample has a component of Swanson Formation that is affecting the REE pattern of the sample that is not accounted for in the model.

However, even with some differences between the model and the sample, the model suggests that it is possible to melt the Ford Granodiorite suite to produce one of the Cretaceous granites with positive Eu anomalies.

6.5 Sr–Nd isotope results

Thirty-eight samples were analyzed for Sr and Nd isotopic compositions and Rb and Sr and Sm and Nd concentrations. Samples include 5 metasedimentary samples from the Swanson Formation, 8 samples from the Ford Granodiorite Suite, 7 paragneiss samples, 5 orthogneiss samples, 2 diatexite samples, 4 Devonian–Carboniferous granites, 6 Cretaceous granites, and 1 microgranite.

Isotopic ratios of granites have been age-corrected to either 360 Ma or 100 Ma depending on the U–Pb age of the granite. Potential sources have been corrected to 360 Ma and 100 Ma to compare their isotope signatures at time of crystallization of either the Devonian–Carboniferous granites or Cretaceous granites. Mixing lines between the two putative sources were calculated using the average Rb, Sr, Nd and Sm compositions of each source and the end-member isotope compositions for each source. The Swanson Formation has $^{87}Sr/^{86}Sr_{360Ma}$ values between 0.711890–0.759472 and has εNd_{360Ma} values ranging from -9.3 to -6.3 (Table 4). Samples from the Ford Granodiorite suite collected from outside of the Fosdick complex have $^{87}Sr/^{86}Sr_{360Ma}$ values of 0.705231–0.709237 and have εNd_{360Ma} values ranging from -3.1 to -0.2 (Table 4). The Ford Granodiorite suite sample collected from within the Fosdick complex, Y1-AW039, has $^{87}Sr/^{86}Sr_{360Ma}$ value of 0.709056 and has an εNd_{360Ma} value of -3.8 (Table 4). At 100 Ma, the Swanson formation has $^{87}Sr/^{86}Sr_{100Ma}$ values of 0.723375–0.766167 and has εNd_{100Ma} values ranging from -11.9 to -9.1 (Table 4). The Ford Granodiorite suite samples from outside the Fosdick complex have $^{87}Sr/^{86}Sr_{100Ma}$ values of 0.709028–0.751809 and have εNd_{100Ma} values ranging from -6.0 to -3.0 (Table 4). The Ford Granodiorite suite sample collected from within the Fosdick complex, Y1-AW039, has an $^{87}Sr/^{86}Sr_{100Ma}$ value of 0.714059 and has an εNd_{360Ma} values of -6.5.

Paragneiss samples have $^{87}Sr/^{86}Sr_{360Ma}$ values that range from 0.695066 to 0.720852 and εNd_{360Ma} values that range from -8.3 to -4.0 (Table 4). Sample Y1-IG057 yields a calculated $^{87}Sr/^{86}Sr_{360Ma}$ ratio of 0.313076. $^{87}Sr/^{86}Sr_{100Ma}$ values that range from 0.719704 to 0.733346 and εNd_{100Ma} values that range from -10.9 to -7.5. Cretaceous age corrected isotope ratios for the paragneiss are consistent with the Swanson Formation. Devonian–Carboniferous age corrected isotope ratios produce a wider spread of Sr and Nd isotope ratios compared with isotope composition of the Swanson Formation. Three of the paragneiss samples have $^{87}Sr/^{86}Sr_{360\ Ma}$ that are less than the initial solar system (Fig. 9). If the paragneiss formed during the Cretaceous, they would give a false age if corrected back to 360 Ma. It is also possible that those paragneiss samples had Sr rich melt extracted from them between the Devonian–Carboniferous and the Cretaceous, producing a higher $^{87}Sr/^{86}Sr$ than would be expected had the system remained closed. If the residue remaining is rich in biotite, then the resulting $^{87}Sr/^{86}Sr$ ratio could increase if enough time has passed for the ^{87}Rb to decay to ^{87}Sr.

Orthogneiss samples have $^{87}Sr/^{86}Sr_{360Ma}$ values of 0.707423–0.710255 and εNd_{360Ma} values ranging from -4.5 to -0.2 (Table 4). At 100 Ma, $^{87}Sr/^{86}Sr_{100Ma}$ values range from 0.712295 to 0.724913 and εNd_{100Ma} values range from -6.8 to -3.7. The age corrected isotope ratios of the orthogneiss are consistent with the age corrected isotope ratios of the Ford Granodiorite suite (Fig. 9 and 10), which supports the hypothesis that the orthogneiss is the high grade equivalent of the Ford Granodiorite suite.

The Devonian–Carboniferous homogenous diatexite, Y1-IG073, has an $^{87}Sr/^{86}Sr_{360Ma}$ of 0.709360 and an εNd_{360Ma} of -4.3. At 100 Ma, the $^{87}Sr/^{86}Sr_{100Ma}$ = 0.715431 and the εNd_{100Ma} =

-7.1. This sample is consistent with isotope composition of the Ford Granodiorite suite and the orthogneisses (Fig. 9). The Devonian–Carboniferous heterogeneous diatexite, Y1-IGO71, has an $^{87}Sr/^{86}Sr_{360Ma}$ = 0.704513 and an εNd_{360Ma} of -5.7. It has a similar εNd_{360Ma} to C5-I26, although has a slightly less radiogenic Sr signature. At 100 Ma, the $^{87}Sr/^{86}Sr_{100Ma}$ ratio is 0.713997 and the εNd_{100Ma} is -8.1 (Table 4).

Devonian–Carboniferous granites have $^{87}Sr/^{86}Sr_{360Ma}$ values of 0.707423–0.710255 and εNd_{360Ma} values that range from -6.0 to -3.3. The isotope compositions for samples Y1-IG062, C6-AW86-1 and M5-G175 are comparable to the Ford Granodiorite suite and the orthogneiss (Fig. 9), suggesting that the granites were derived from the Ford Granodiorite suite. Sample C5-I26 lies between the Ford Granodiorite suite and the Swanson Formation, close to the mixing line between the two potential sources at about 45% Swanson Formation (Fig. 9).

Cretaceous granites have $^{87}Sr/^{86}Sr_{100Ma}$ ratios that range from 0.718598to 0.725792 and εNd_{100Ma} values of -8.2 to -5.1. Garnet-bearing Cretaceous granites, Y1-IG052 and Y1- AE064, have $^{87}Sr/^{86}Sr_{100Ma}$ of 0.723376 and 0.718598, respectively and have εNd_{100Ma} of -6.3 and -6.5, respectively. The microgranite, 10CY-024, has an $^{87}Sr/^{86}Sr_{100Ma}$ ratio of 0.708989 and an εNd_{100Ma} of -10 (Table 4).

Table 4: Sr–Nd isotope composition of source rocks and granites

Rock Type:	**Swanson Formation**					**Ford Granodiorite Suite**			
Sample Name:	**10CY-001**	**10CY-002**	**Y2-BR086**	**Y2-MD092**	**Y2-MP098**	**51225-1**	**51225-2**	**Y2-GP091**	**Y2-HN097**
Rb (ppm)	131.3	205.5	155.2	99.95	95.55	194.2	220.7	142.5	85.33
Sr (ppm)	201.1	147.6	128.7	194.8	150.7	223.0	220.4	375.9	357.2
Rb/Sr	0.65	1.39	1.21	0.51	0.63	0.87	1.00	0.38	0.24
^{87}Rb/^{86}Sr	2.086	4.037	0.000	1.487	1.838	2.288	2.901	1.097	0.6911
^{87}Sr/^{86}Sr	0.726291	0.732242	0.738139	0.727782	0.768736	0.720773	0.721630	0.710770	0.708715
^{87}Sr/^{86}Sr$_{100Ma}$	0.723375	0.726599	0.738139	0.725704	0.766167	0.717575	0.717575	0.709237	0.707749
^{87}Sr/^{86}Sr$_{360Ma}$	0.715775	0.711890	0.738139	0.720285	0.759472	0.709237	0.707005	0.705241	0.705231
Sm (ppm)	6.612	6.652	7.977	6.022	6.856	9.190	11.179	4.315	3.823
Nd (ppm)	35.29	32.76	38.80	30.32	34.32	45.89	59.61	21.54	18.21
Sm/Nd	0.19	0.20	0.21	0.20	0.20	0.20	0.19	0.20	0.21
^{147}Sm/^{144}Nd	0.1133	0.1227	0.1243	0.1200	0.1208	0.0904	0.1134	0.1211	0.1109
^{143}Nd/^{144}Nd	0.512117	0.512084	0.512079	0.511979	0.512061	0.512378	0.512292	0.512432	0.512276
εNd$_{100Ma}$	-9.1	-9.9	-10.0	-11.9	-10.3	-3.7	-5.7	-3.1	-6.0
εNd$_{360Ma}$	-6.3	-7.4	-7.6	-9.3	-7.8	-0.2	-2.9	-0.5	-3.1

Rock Type:	**Ford Granodiorite Suite**				**Orthogneiss**				
Sample Name:	**Y2-JU096**	**Y2-MS089**	**Y2-SM095**	**Y1-AE035**	**10CY-035**	**Y1-AW049**	**Y1-AW039**	**Y1-IG053**	**Y1-MJ075**
Rb (ppm)	122.2	339.13	100.45	128.6	196.2	133.2	131.3	114.4	224.8
Sr (ppm)	422.8	81.49	345.6	271.1	269.8	288.3	181.0	285.9	156.5
Rb/Sr	0.29	4.16	0.29	0.47	0.73	0.46	0.73	0.40	1.44
^{87}Rb/^{86}Sr	0.8362	12.11	0.8408	1.373	2.105	1.337	2.101	1.159	4.164
^{87}Sr/^{86}Sr	0.710850	0.768736	0.710204	0.715979	0.718183	0.714164	0.721511	0.716095	0.730733
^{87}Sr/^{86}Sr$_{100Ma}$	0.709681	0.751809	0.709028	0.714059	0.715240	0.712295	0.718575	0.716091	0.724913
^{87}Sr/^{86}Sr$_{360Ma}$	0.706634	0.707688	0.705965	0.709056	0.707570	0.707423	0.710921	0.716079	0.709743
Sm (ppm)	8.560	4.328	4.828	6.072	2.494	6.532	6.301	6.469	6.997
Nd (ppm)	46.65	17.31	22.98	31.43	11.52	38.37	28.79	34.52	46.79
Sm/Nd	0.18	0.25	0.21	0.19	0.22	0.17	0.22	0.19	0.15
^{147}Sm/^{144}Nd	0.1269	0.1511	0.1270	0.1168	0.1309	0.1029	0.1323	0.1133	0.0904
^{143}Nd/^{144}Nd	0.512438	0.512385	0.512368	0.512254	0.512253	0.512229	0.511900	0.512252	0.512378
εNd$_{100Ma}$	-3.0	-4.4	-4.4	-6.5	-6.7	-6.8	-13.6	-6.5	-3.7
εNd$_{360Ma}$	-0.7	-2.8	-2.1	-3.8	-4.5	-3.7	-11.4	-3.7	-0.2

Rock Type:	**Paragneiss**						
Sample Name:	**10CY-010**	**10CY-015**	**10CY-023**	**10CY-033**	**Y1-CB080**	**Y1-IG057**	**Y1-LH077**
Rb (ppm)	205.5	284.9	232.4	206.5	147.3	453.1	164.7
Sr (ppm)	147.6	104.4	99.59	98.35	144.3	11.92	139.3
Rb/Sr	1.39	2.73	2.33	2.10	1.02	38.02	1.18
^{87}Rb/^{86}Sr	4.037	7.919	6.762	6.090	2.960	111.8	3.429
^{87}Sr/^{86}Sr	0.732242	0.739512	0.729157	0.734120	0.731493	0.876604	0.738139
^{87}Sr/^{86}Sr$_{100Ma}$	0.726599	0.728444	0.719704	0.725607	0.727356	0.720353	0.733346
^{87}Sr/^{86}Sr$_{360Ma}$	0.711890	0.699593	0.695066	0.703418	0.716573	0.313076	0.720852
Sm (ppm)	13.23	9.802	10.50	7.233	7.593	12.45	7.506
Nd (ppm)	69.90	51.43	46.59	35.57	38.56	65.74	38.24
Sm/Nd	0.19	0.19	0.23	0.20	0.20	0.19	0.20
^{147}Sm/^{144}Nd	0.1144	0.1152	0.1210	0.1229	0.1190	0.1145	0.1186
^{143}Nd/^{144}Nd	0.512098	0.512203	0.512253	0.512090	0.512187	0.512044	0.512027
εNd$_{100Ma}$	-9.5	-7.5	-6.6	-9.8	-7.8	-10.5	-10.9
εNd$_{360Ma}$	-6.8	-4.7	-4.0	-7.3	-5.2	-7.8	-8.3

Table 4: Continued

	Devonian-Carboniferous					
Rock Type:	**Diatexite**		**Granite**			
Sample Name:	**Y1-IG071**	**Y1-IG073**	**Y1-IG062**	**C5-I26**	**C6-AW86-1**	**M5-G175**
Rb (ppm)	171.2	146.6	154.4	225.6	167.2	213.8
Sr (ppm)	190.5	279.7	225.8	280.4	328.8	248.5
Rb/Sr	0.90	0.52	0.68	0.80	0.51	0.86
^{87}Rb/^{86}Sr	2.603	1.642	1.987	2.330	1.472	2.492
^{87}Sr/^{86}Sr	0.717636	0.717636	0.719813	0.719497	0.713661	0.720081
^{87}Sr/^{86}Sr$_{100Ma}$	0.713997	0.715341	0.717036	0.716241	0.711604	0.716597
^{87}Sr/^{86}Sr$_{360Ma}$	0.704513	0.709360	0.709795	0.707752	0.706242	0.707518
Sm (ppm)	8.463	11.48	3.471	16.61	4.972	10.15
Nd (ppm)	41.30	61.65	15.02	65.96	25.77	53.60
Sm/Nd	0.20	0.19	0.23	0.25	0.19	0.19
^{147}Sm/^{144}Nd	0.123871	0.112547	0.1361	0.1522	0.1166	0.1145
^{143}Nd/^{144}Nd	0.512175	0.512217	0.512256	0.512227	0.512281	0.512225
εNd$_{100Ma}$	-8.1	-7.1	-6.7	-7.4	-5.9	-7.0
εNd$_{360Ma}$	-5.7	-4.3	-4.7	-6.0	-3.3	-4.3

	Cretaceous						
Rock Type:	**Granites**						**Microgranite**
Sample Name:	**10CY-039**	**Y1-IG052**	**Y1-IG070**	**Y1-AW038**	**Y1-AE033**	**Y1-AE064**	**10CY-024**
Rb (ppm)	164.9	131.0	84.58	255.2	130.7	154.9	192.1
Sr (ppm)	240.1	252.9	219.1	172.3	210.7	195.2	225.6
Rb/Sr	0.69	0.52	0.39	1.48	0.62	0.79	0.85
^{87}Rb/^{86}Sr	1.901	1.532	1.118	4.244	1.736	2.125	2.303
^{87}Sr/^{86}Sr	0.723183	0.725517	0.721505	0.725957	0.721024	0.728763	0.712208
^{87}Sr/^{86}Sr$_{100Ma}$	0.720526	0.723376	0.719943	0.720025	0.718598	0.725792	0.708989
^{87}Sr/^{86}Sr$_{360Ma}$	0.713598	0.717794	0.715869	0.704562	0.712273	0.718048	0.700600
Sm (ppm)	0.4368	1.073	0.4497	0.3425	2.625	2.927	10.08
Nd (ppm)	1.975	5.652	2.956	1.120	13.39	12.29	54.93
Sm/Nd	0.22	0.19	0.15	0.31	0.20	0.24	0.18
^{147}Sm/^{144}Nd	0.1337	0.1400	0.0919	0.1848	0.1440	0.1133	0.1243
^{143}Nd/^{144}Nd	0.512338	0.512277	0.512151	0.512346	0.512251	0.512190	0.512079
εNd$_{100Ma}$	-5.1	-6.3	-8.2	-5.5	-6.5	-8.1	-10.0
εNd$_{360Ma}$	-3.0	-4.4	-4.7	-5.2	-3.7	-6.3	-7.6

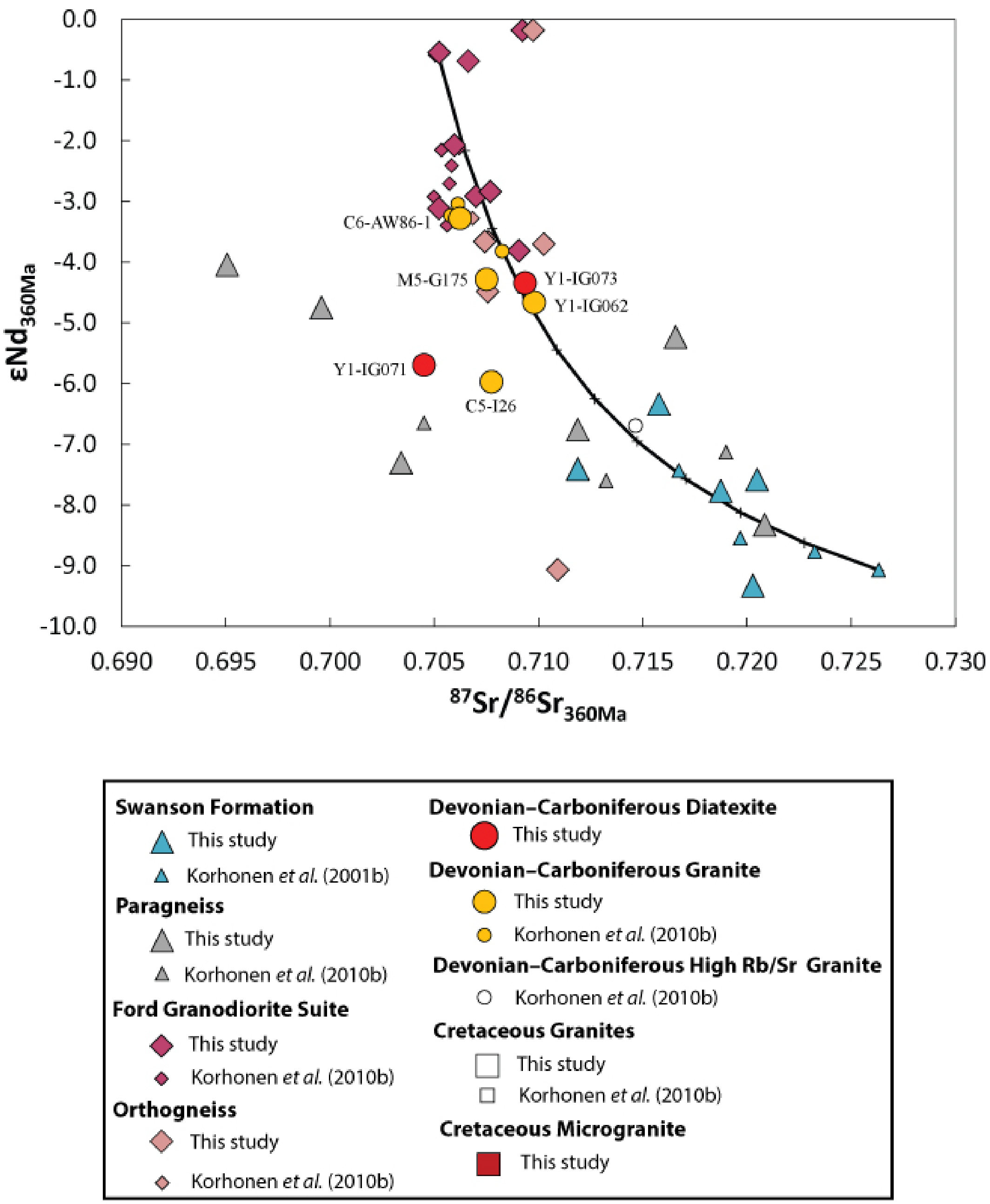

Figure 9: Sr–Nd isotopic compositions at 360 Ma for source rocks and granites from the Ford Ranges. Tick marks along mixing curve are 10% increments of melting between sources.

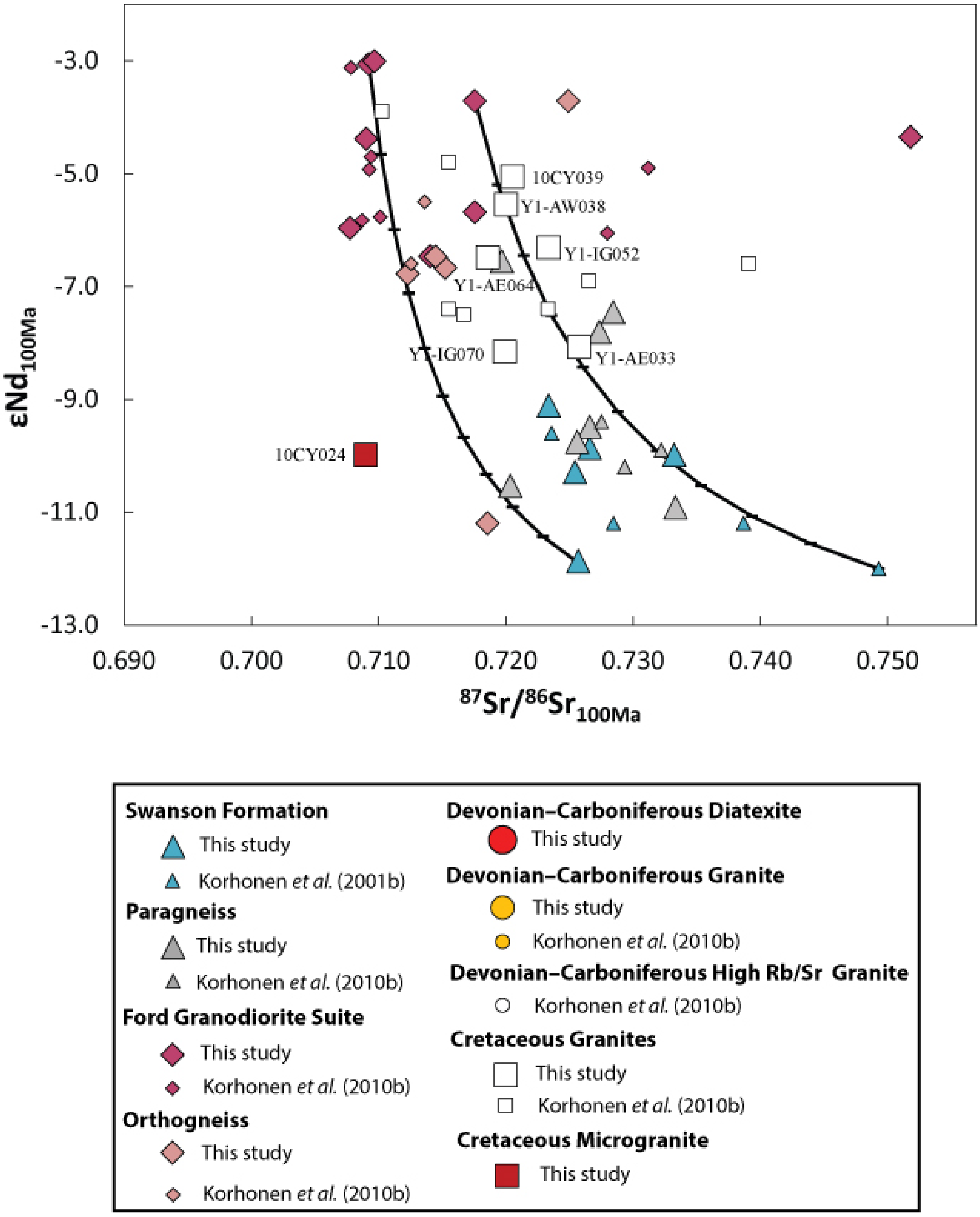

Figure 10: Sr–Nd isotopic compositions at 100 Ma for source rocks and granites from the Ford Ranges. Tick marks along mixing curve are 10% increments of melting between sources.

6.6 Sr–Nd isotope discussion

Paragneiss sample have isotope compositions that generally overlap with the isotope composition of the Swanson Formation. The agreement between the paragneiss and the Swanson Formation is strongest when the samples are age corrected to 100Ma. When corrected to 360Ma, 3 paragneiss samples have $^{87}Sr/^{86}Sr$ ratios that are lower than the initial solar system $^{87}Sr/^{86}Sr$ ratio (Fig. 9). Either these samples were not formed during the Devonian–Carboniferous and the age correct ratios are spurious, or the samples have had Sr-rich melt extracted from them at some point after 360 Ma, leaving behind a Rb rich residue. This would falsely increase the $^{87}Sr/^{86}Sr$ ratio when age corrected to 360 Ma. Despite the isotopic irregularities during the Devonian–Carboniferous, the paragneiss generally have major and trace element compositions as well as isotope compositions that are similar to the Swanson Formation, consistent with the conclusions of Korhonen *et al.,* (2010b) that the paragneisses are the high-grade equivalents of the Swanson Formation.

Orthogneiss samples have isotope compositions that generally overlap with the isotope composition for the Ford Granodiorite suite (Fig. 9 and 10). The orthogneiss also have similar major and trace element compositions as the Ford Granodiorite suite (Fig 2 and 3). Sample Y1-AW039 has a less radiogenic Nd signature than the rest of the orthogneisses. This may reflect the entrapment of melt derived from the less radiogenic Swanson Formation in the sample or an analytical issue. The isotope data from this study support the conclusions of Korhonen *et al.* (2010b) that the orthogneisses are genetically related to the Ford Granodiorite suite.

Devonian–Carboniferous granites and diatexites generally have similar isotope compositions as the Ford Granodiorite suite and the orthogneiss samples (Fig. 9), suggesting that they were either derived from that source or has a mixed source with larger contribution from the Ford Granodiorite than from the Swanson Formation. Sample Y1-IG071 does not fall on a mixing line between the Swanson Formation and the Ford Granodiorite suite (Fig. 9). It is possible that the Swanson Formation can have lower $^{87}Sr/^{86}Sr$ but no samples with those compositions have been sampled and analyzed. This sample also has a mixed zircon population. If the sample crystallized in the Cretaceous, then age correcting back to 360 Ma could yield a lower than expected $^{87}Sr/^{86}Sr$ ratio. Sample C5-I26 has an isotope composition that reflects a mix of the Ford Granodiorite source and the Swanson Formation source (Fig. 9). This sample also has a phosphorus content that is an order of magnitude greater than the other granites, as well as elevated Sm/Nd values compared with values from the potential sources (Tables 1 and 2). The elevated Sm/Nd ratios and the elevated phosphorous content are consistent with the presence of apatite either precipitated from the melt or entrained from the source. This sample may reflect a filter zone where apatite or monazite remained after melt was removed.

Cretaceous granites generally have isotope compositions that are consistent with the Ford Granodiorite suite with two samples, Y1-IG070 and Y1-AE033, which could represent mixing between the two sources. Sample Y1-IG070 does not have elevated Sm/Nd ratios compared with either source and likely represents a mix of the two sources (Table 2). Sample Y1-AE033 has elevated Sm/Nd and low phosphorous content compared with the source. It is possible that this sample represents a mixture of the two sources and has an accessory phase that is controlling the Sm/Nd ratio and possibly the εNd value.

Chapter 7: Conclusions

Based on the major and trace elements as well as the isotope compositions of the granites analyzed in the study, Devonian–Carboniferous granites are derived primarily from the Ford Granodiorite Suite, consistent with results from Korhonen *et al.* (2010b). Because the Ford Granodiorite suite was not a fertile source at the *P–T* conditions of metamorphism during the Devonian–Carboniferous at the level of the Fosdick complex, it is likely that these granites were sourced from deeper in the crust. The elevated Sr and low Rb would indicate melting at *P–T* conditions above biotite stability, involving the breakdown of plagioclase and hornblende at higher temperatures than recorded in the Fosdick complex. These minerals would contribute more Sr to the melt and produce melts with lower Rb/Sr ratios. The major and trace element concentrations of these granites are consistent with them being mixtures of melt and either cumulate biotite and plagioclase or, for two samples, cumulate plagioclase and K-feldspar.

The chemical compositions and isotope composition of the Cretaceous granites are consistent with them being derived from mixtures of both the Ford Granodiorite suite and the Swanson Formation. Because the Ford Granodiorite suite is not a fertile source at the *P–T* conditions during the Cretaceous, it is likely that these melts were sourced from deeper in the crust, much like the Devonian–Carboniferous granites. Devonian–Carboniferous granites tend to show oscillatory-zoned zircons whereas zircons from Cretaceous granites show dark metamict cores surrounded by a thin bright rim in CL. The presence of inherited zircon cores may indicate lower water content during melting in the Cretaceous. These findings are consistent with findings of Korhonen *et al.*, (2010b). Previous results noted a temporal and spatial difference between Cretaceous granites derived from the Ford Granodiorite and granites from the Swanson Formation, where Ford Granodiorite suite-derived granites are older than those derived from the Swanson (Korhonen *et al.*, 2010b). In contrast to previous results, all Cretaceous granites in this study yield ages younger than 110 Ma and granites with a Swanson Formation component are not limited spatially to the leucogranite sheeted complex, but were emplaced throughout the Fosdick complex.

In summary, the results of this study have determined that the Devonian–Carboniferous granites from the Fosdick migmatite–granite complex crystallized c.360 Ma and are primarily derived from the Ford Granodiorite suite. Samples that fall between the two sources can be ascribed to mixing. The Cretaceous samples crystallized c.100 Ma and are prevalent thought out the Fosdick complex. The Cretaceous granites are also primarily derived from the Ford Granodiorite suite. Samples that fall in between the two sources represent mixing or possibly represent a melt where an accessory phase is controlling the εNd value. There is no evidence for source other than the two crustal sources previous mentioned, indicating that is possible to differentiate the continental crust a convergent margin without the addition of a more juvenile source.

Appendix A: Sample Analysis and Sample Locations

Table A1: List of sample names and analyses completed

Swanson
Formation

Sample Name	Location	U–Pb	XRF	REE	Sr–Nd
10CY-001	Clark Mts		✓	✓	✓
10CY-002	Clark Mts		✓	✓	✓
Y2-BR086	Bailey Ridge		✓	✓	✓
Y2-MD092	Mt. Dolber		✓	✓	✓
Y2-MP098	Mt. Passell		✓	✓	✓

Ford Granodiorite suite

Sample Name	Location	U–Pb	XRF	REE	Sr–Nd
51225-1	Chester Mts	✓	✓	✓	✓
51225-2	Chester Mts	✓	✓	✓	✓
Y2-GP091	Greer Peak	✓	✓	✓	✓
Y2-HN097	Hermann Nunatak		✓	✓	✓
Y2-JU096	Mt June	✓	✓	✓	✓
Y2-MS089	Mt Swan		✓	✓	✓
Y2-SM095	Saunders Mountain		✓	✓	✓
Y1-AE035	Mt Avers East	✓	✓	✓	✓

Paragneiss

Sample Name	Location	U–Pb	XRF	REE	Sr–Nd
10CY-010	Mt Bitgood		✓	✓	✓
10CY-015	Mt Bitgood		✓	✓	✓
10CY-021	Maigetter Peak		✓		
10CY-023	Maigetter Peak		✓	✓	✓
10CY-033	Mt Avers East		✓	✓	✓
10CY-041	Mt Avers East		✓	✓	
Y1-BB013	Bird Bluff		✓	✓	✓
Y1-CB080	Colombo		✓	✓	✓
Y1-IG057	Mt Iphigene		✓	✓	
Y1-IG061	Mt Iphigene		✓	✓	✓
Y1-LH077	Lochart		✓	✓	

Swanson Formation

Sample Name	Location	U–Pb	XRF	REE	Sr–Nd
10CY-001	Clark Mts		✓	✓	✓
10CY-002	Clark Mts		✓	✓	✓
Y2-BR086	Bailey Ridge		✓	✓	✓
Y2-MD092	Mt. Dolber		✓	✓	✓
Y2-MP098	Mt. Passell		✓	✓	✓

Ford Granodiorite suite

Sample Name	Location	U–Pb	XRF	REE	Sr–Nd
51225-1	Chester Mts	✓	✓	✓	✓
51225-2	Chester Mts	✓	✓	✓	✓
Y2-GP091	Greer Peak	✓	✓	✓	✓
Y2-HN097	Hermann Nunatak		✓	✓	✓
Y2-JU096	Mt June	✓	✓	✓	✓
Y2-MS089	Mt Swan		✓	✓	✓
Y2-SM095	Saunders Mountain		✓	✓	✓
Y1-AE035	Mt Avers East	✓	✓	✓	✓

Paragneiss

Sample Name	Location	U–Pb	XRF	REE	Sr–Nd
10CY-010	Mt Bitgood		✓	✓	✓
10CY-015	Mt Bitgood		✓	✓	✓
10CY-021	Maigetter Peak		✓		
10CY-023	Maigetter Peak		✓	✓	✓
10CY-033	Mt Avers East		✓	✓	✓
10CY-041	Mt Avers East		✓	✓	
Y1-BB013	Bird Bluff		✓	✓	✓
Y1-CB080	Colombo		✓	✓	✓
Y1-IG057	Mt Iphigene		✓	✓	
Y1-IG061	Mt Iphigene		✓	✓	✓
Y1-LH077	Lochart		✓	✓	

Table A1: Continued

Orthogneiss

Sample Name	Location	U–Pb	XRF	REE	Sr–Nd
10CY-035	Mt Avers East	✓	✓	✓	✓
Y1-AW039	Mt Avers West	✓	✓	✓	✓
Y1-AW049	Mt Avers West	✓	✓	✓	✓
Y1-IG053	Mt Iphigene	✓	✓	✓	✓
Y1-MJ075	Marujupu	✓	✓	✓	✓

Diatexite (Devonian-Carboniferous)

Sample Name	Location	U–Pb	XRF	REE	Sr–Nd
Y1-IG071	Mt Iphigene	✓	✓	✓	✓
Y1-IG073	Mt Iphigene	✓	✓	✓	✓

Carboniferous high-Sr granite

Sample Name	Location	U–Pb	XRF	REE	Sr–Nd
Y1-IG062	Mt Iphigene	✓	✓	✓	✓
C5-I26	Mt Iphigene		✓	✓	✓
C6-AW86-1	Mt Avers West		✓	✓	✓
M5-G175	Mt Getz		✓	✓	✓

Cretaceous Granites

Sample Name	Location	U–Pb	XRF	REE	Sr–Nd
Y1-AW038	Avers West	✓	✓	✓	✓
10CY-039	Avers East	✓	✓	✓	✓
Y1-AE051	Avers East	✓	✓	✓	
Y1-IG052	Iphigene	✓	✓	✓	✓
Y1-IG070	Iphigene	✓	✓	✓	✓
Y1-AE064	Avers East	✓	✓	✓	✓
Y1-AE033	Avers East	✓	✓	✓	✓

Microgranite

Sample Name	Location	U–Pb	XRF	REE	Sr–Nd
10CY-024	Maigetter Peak	✓	✓	✓	✓

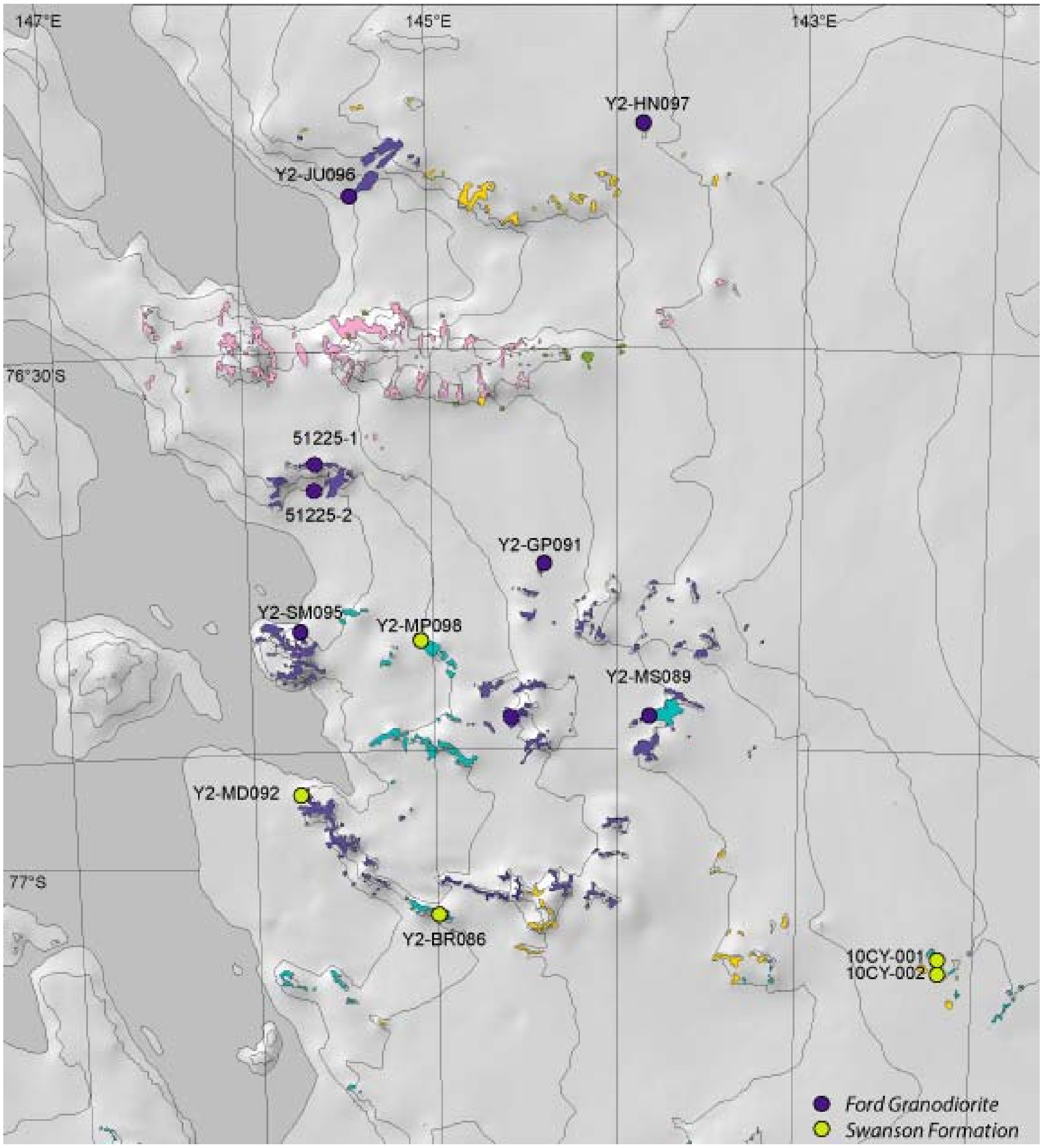

Figure A1: Putative source sample locations within the Ford Ranges

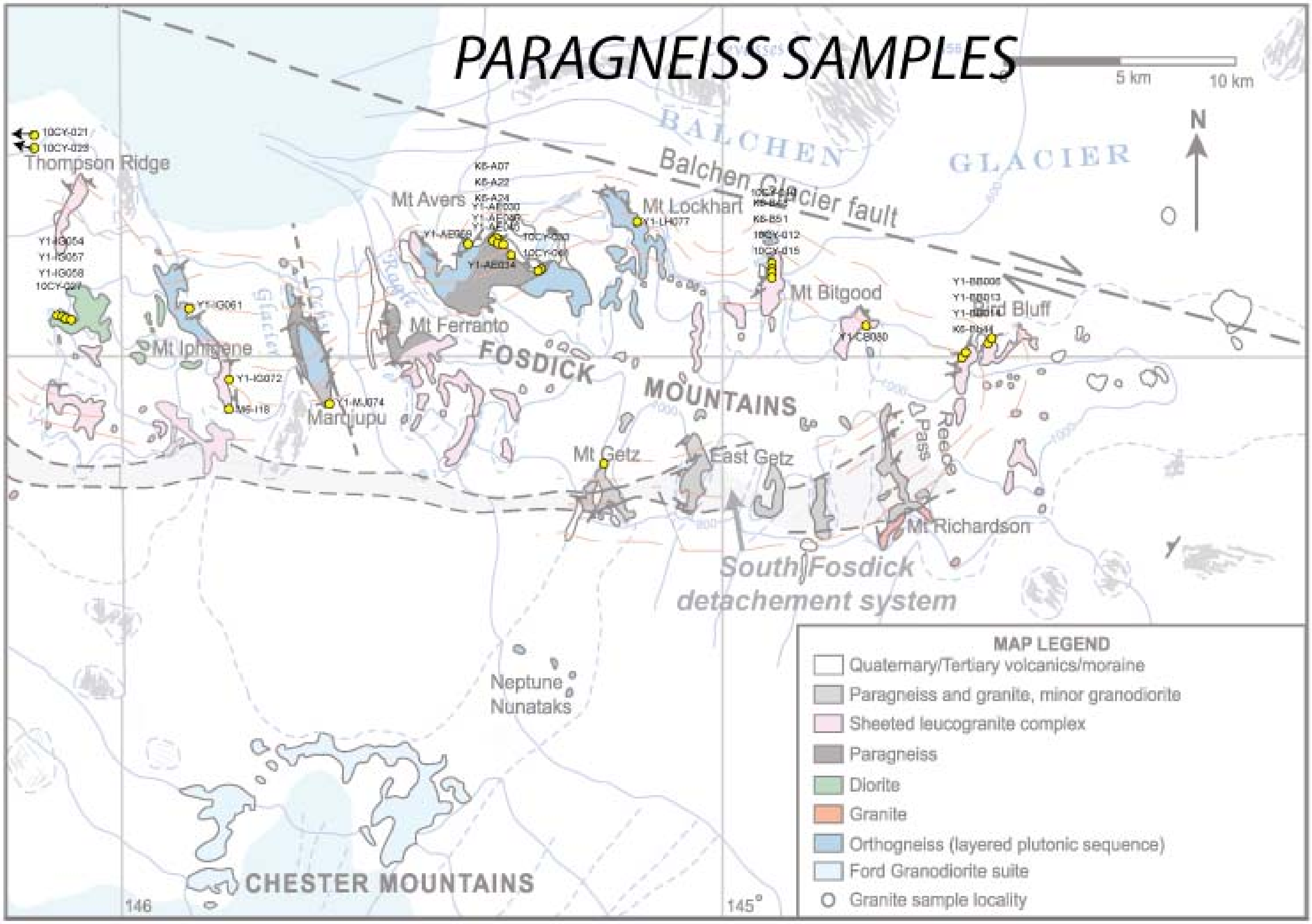

Figure A2: Paragneiss sample locations within the Fosdick migmatite–granite complex

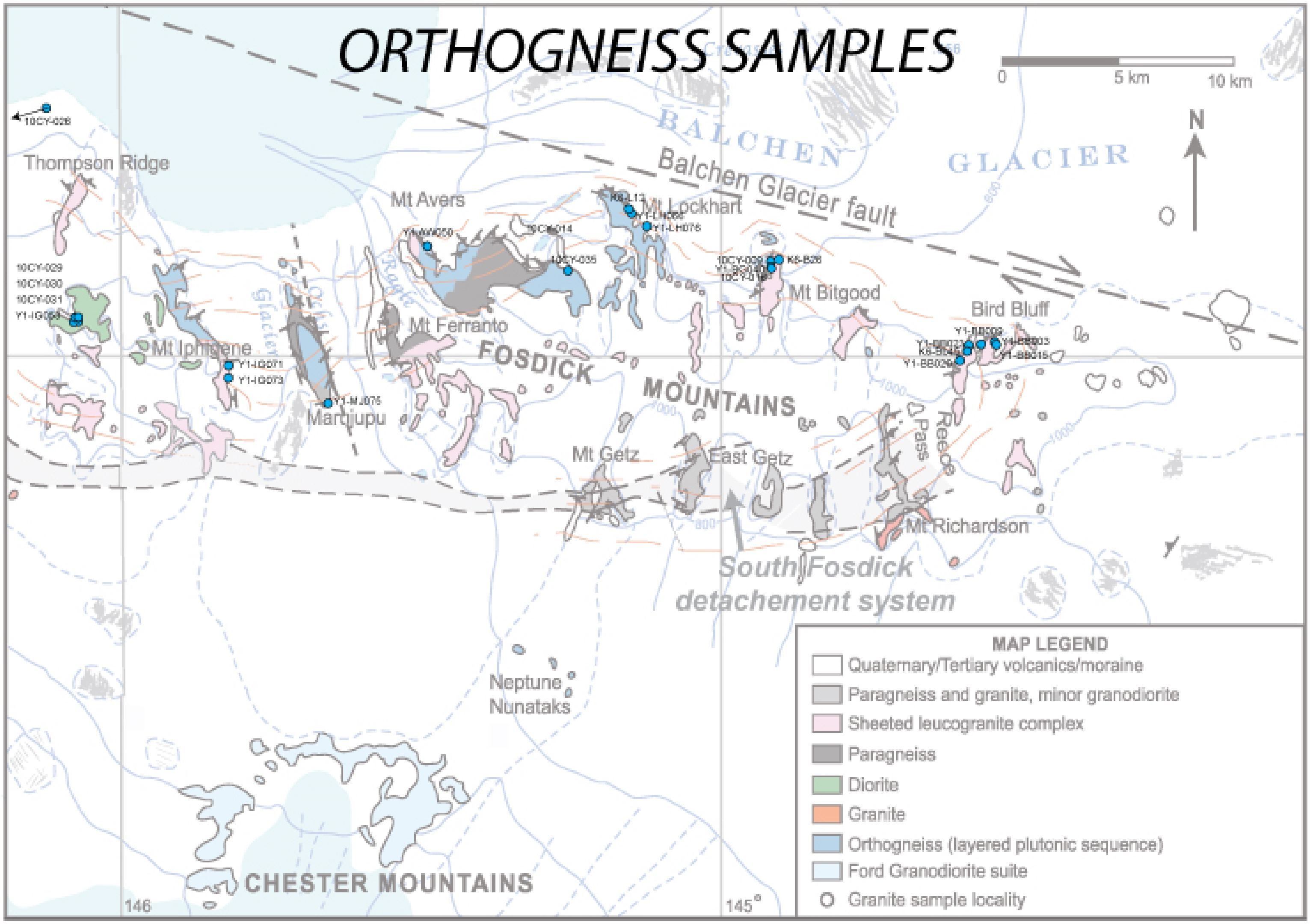

Figure A3: Orthogneiss sample locations within the Fosdick migmatite–granite complex

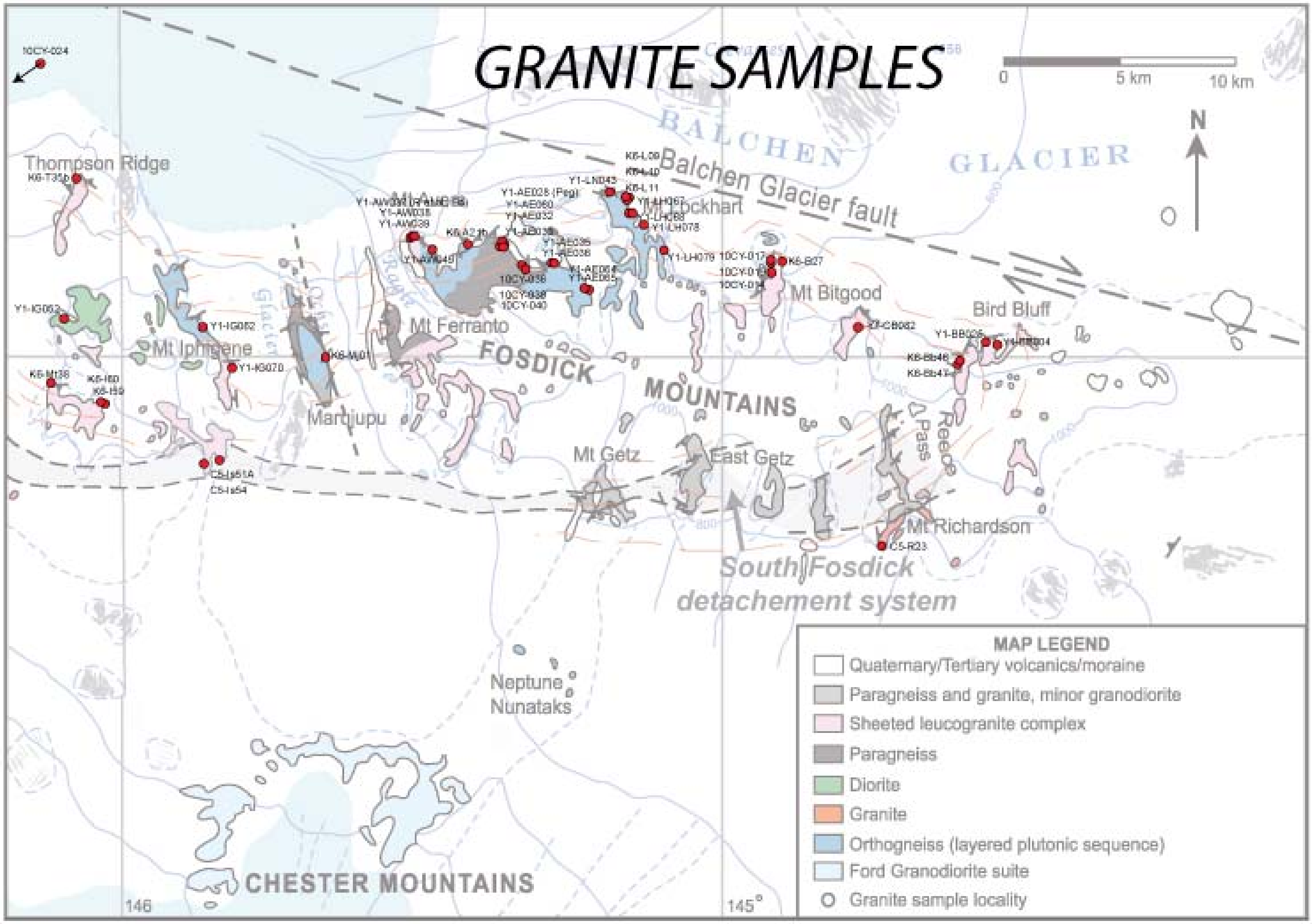

Figure A4: Granite sample locations within the Fosdick migmatite–granite complex

Appendix B: Sample Photomicrographs

Swanson Formation

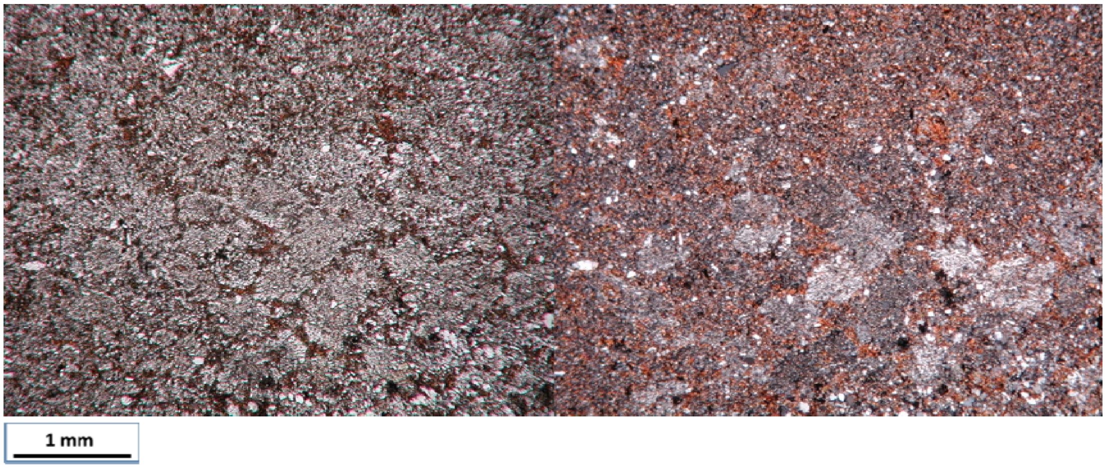

Figure B1: Photomicrograph of thin section 10CY-001

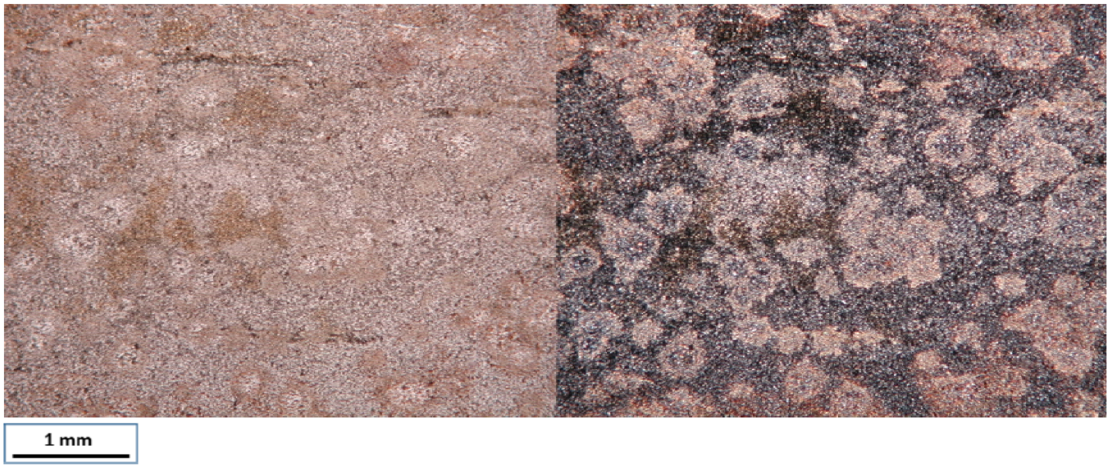

Figure B2: Photomicrograph of thin section 10CY-002

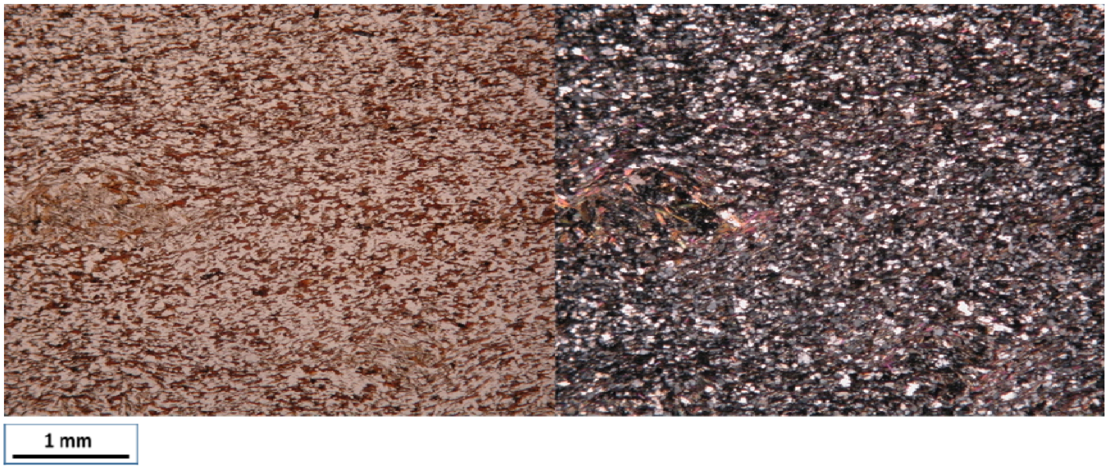

Figure B3: Photomicrograph of thin section Y2-BR086

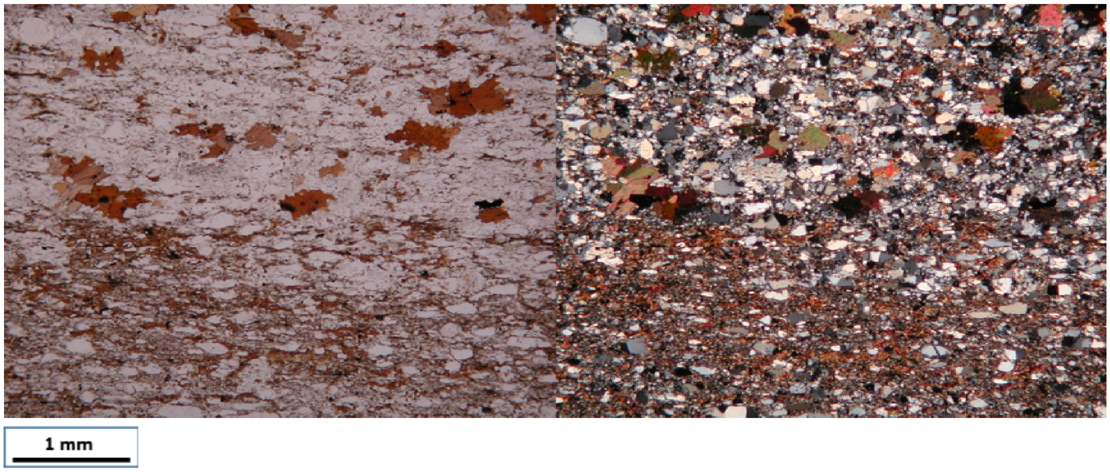

Figure B4: Photomicrograph of thin section Y2-MD092

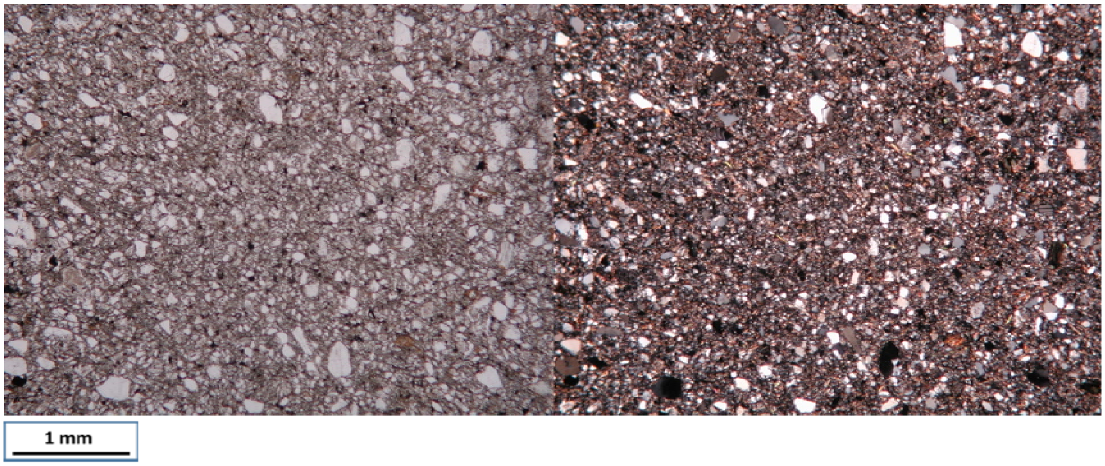

Figure B5: Photomicrograph of thin section Y2-MP098

Ford Granodiorite suite

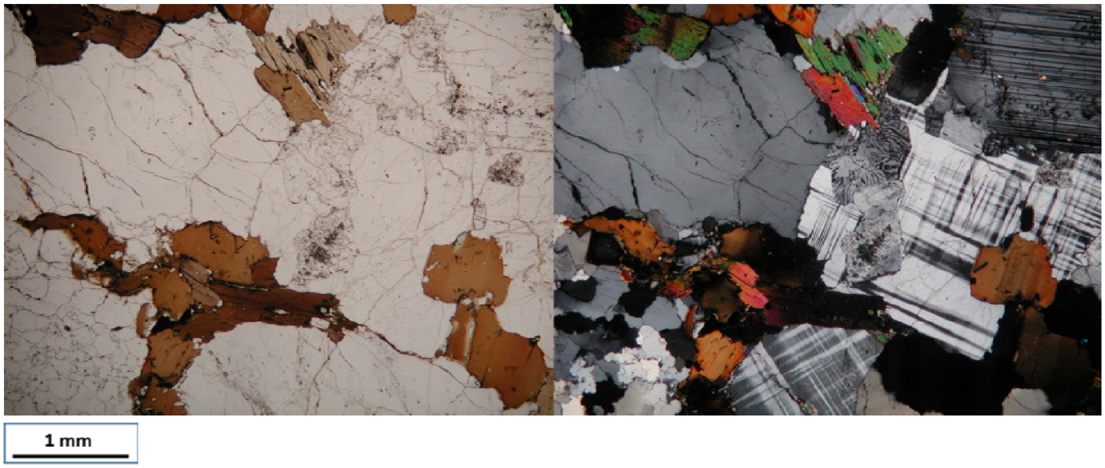

Figure B6: Photomicrograph of thin section 51225-1

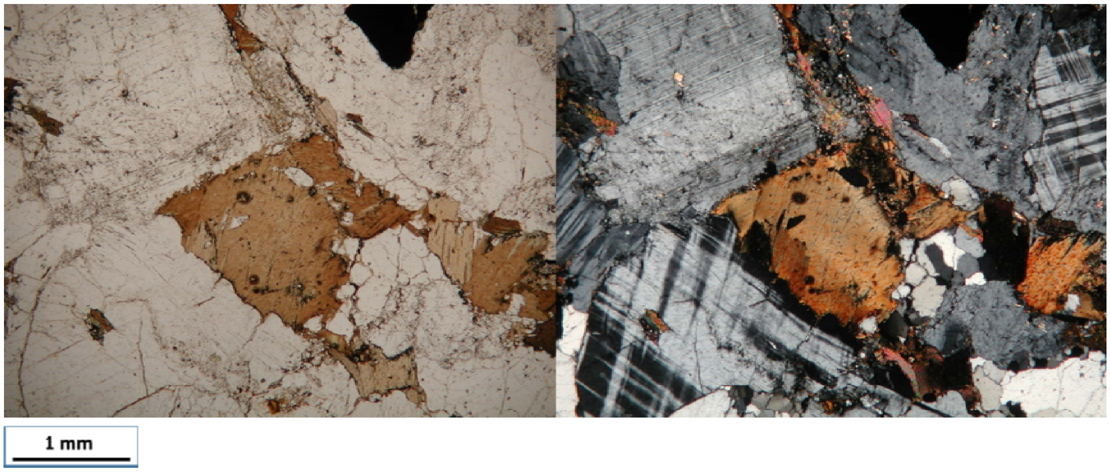

Figure B7: Photomicrograph of thin section 51225-2

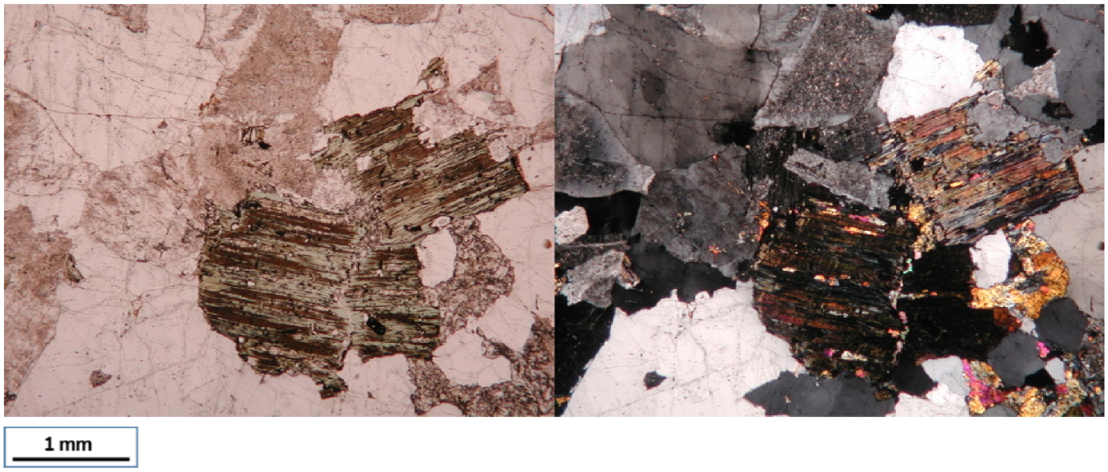

Figure B8: Photomicrograph of thin section Y2-GP091

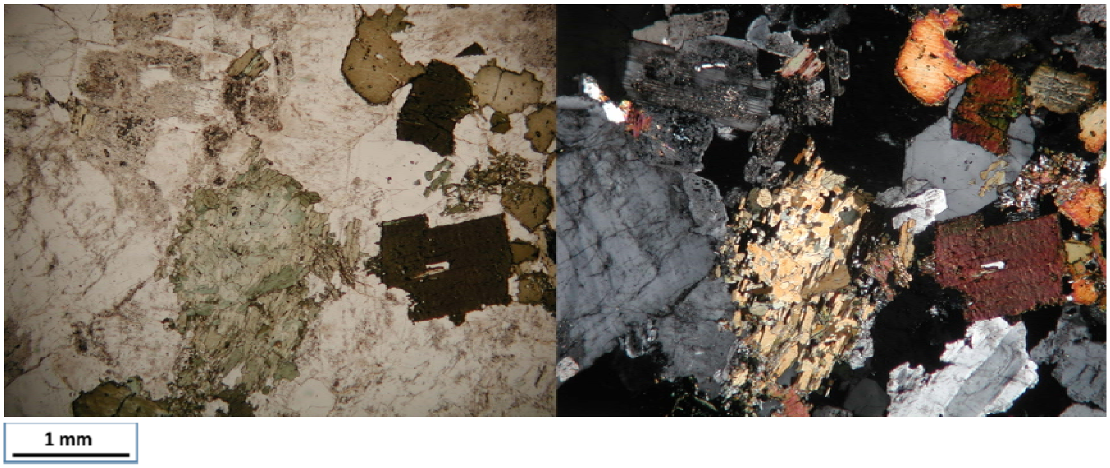

Figure B9: Photomicrograph of thin section Y2-HN097

Figure B10: Photomicrograph of thin section Y2-JU096

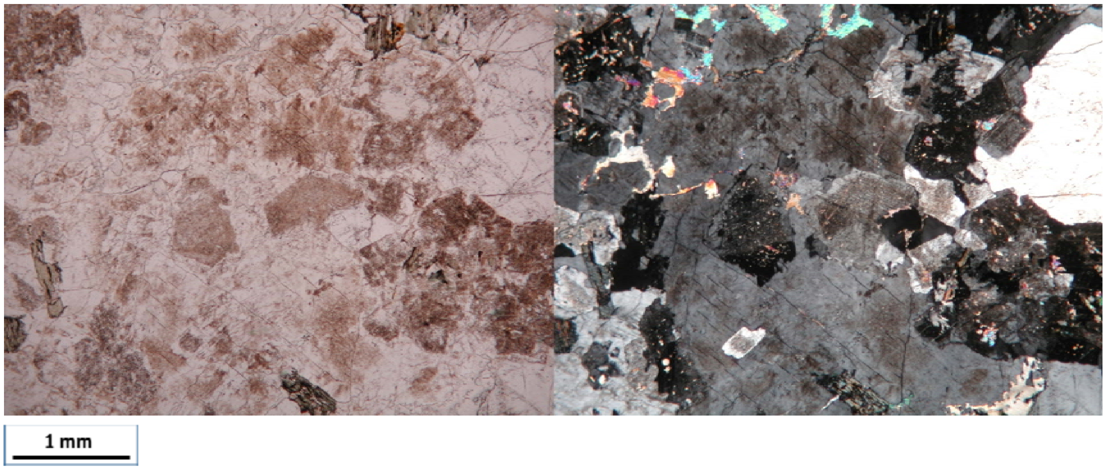

Figure B11: Photomicrograph of thin section Y2-MS089

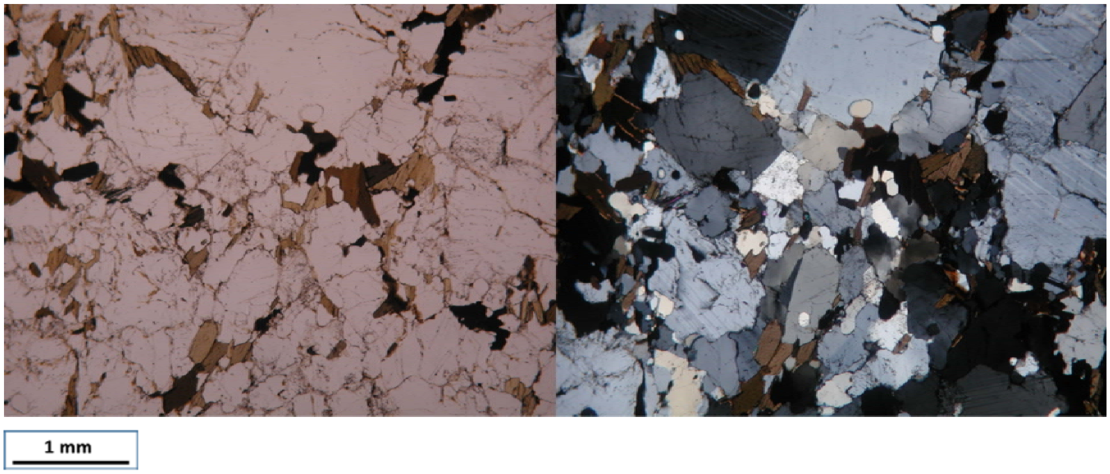

Figure B12: Photomicrograph of thin section Y2-SM095

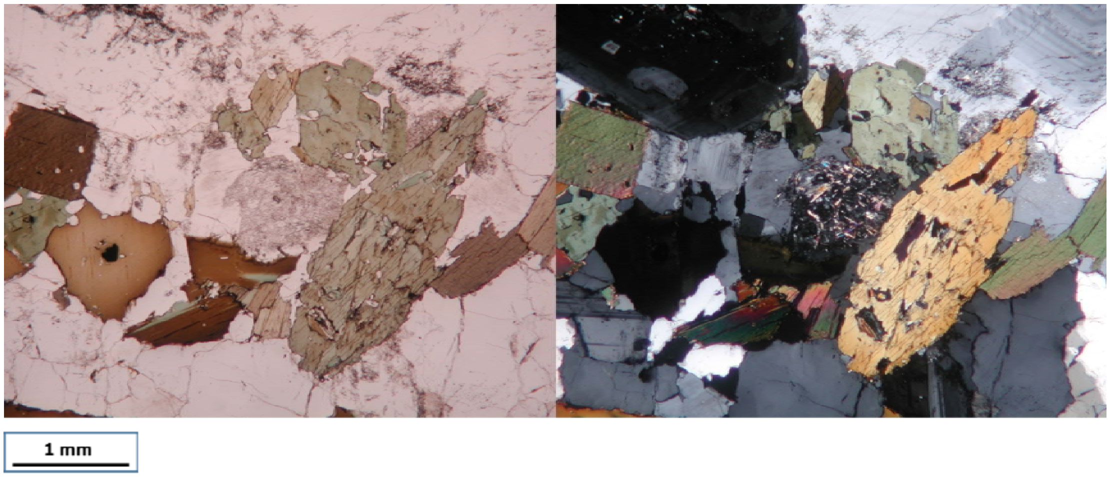

Figure B13: Photomicrograph of thin section Y1-AE035

Paragneisses

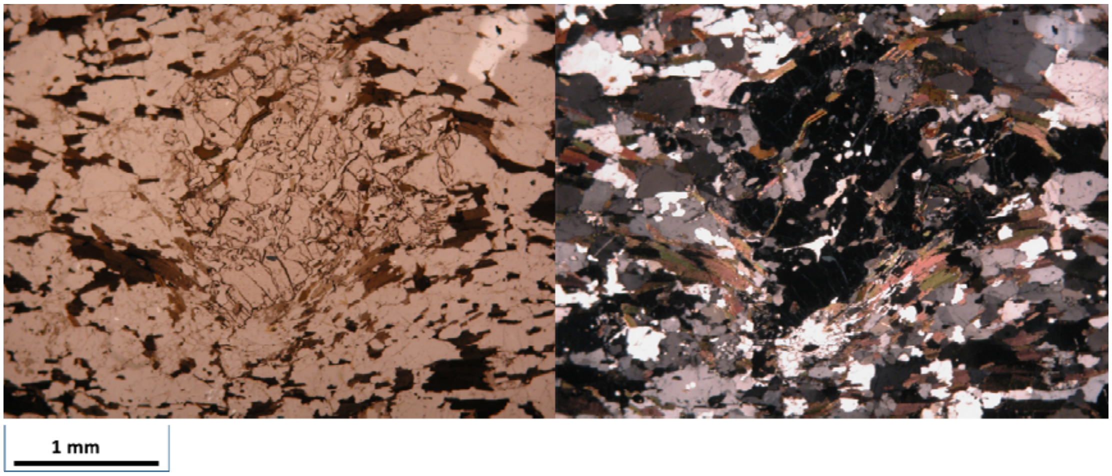

Figure B14: Photomicrograph of thin section 10CY-010

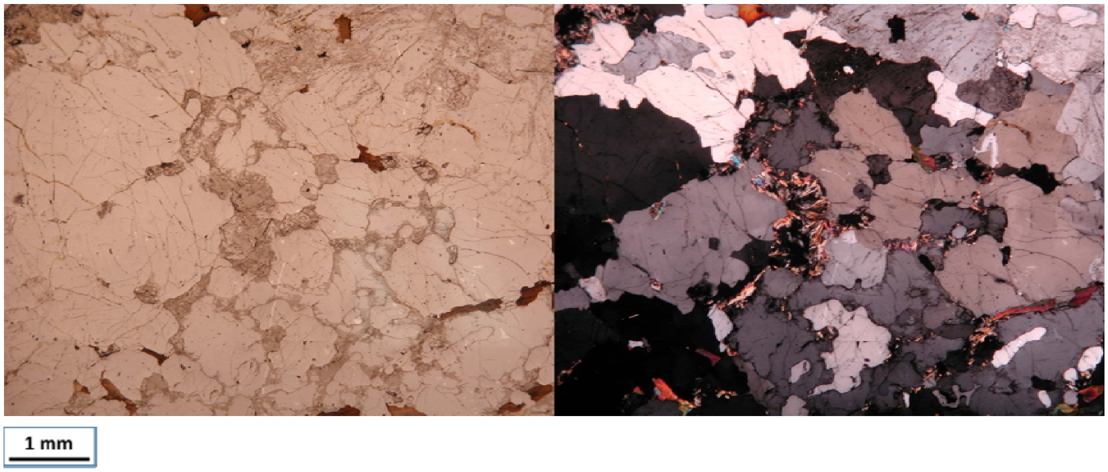

Figure B15: Photomicrograph of thin section 10CY-015

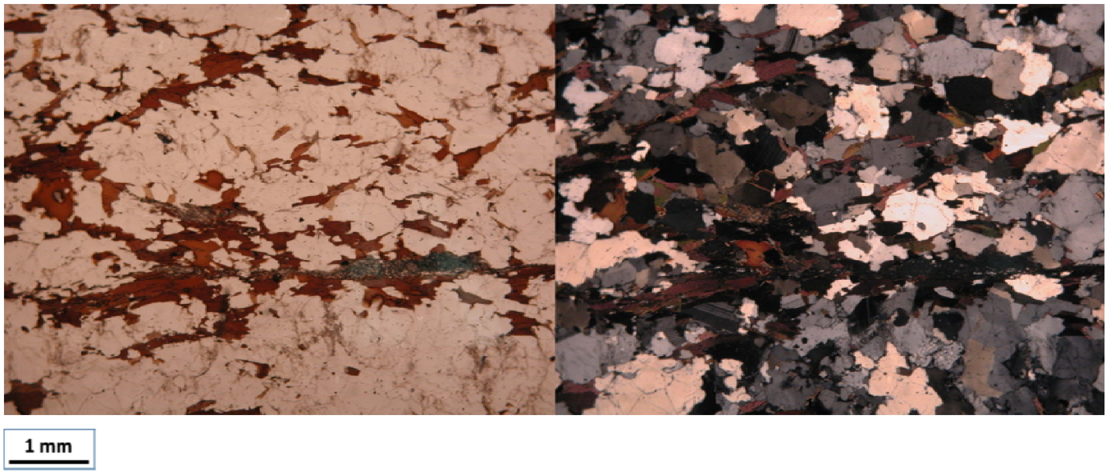

Figure B16: Photomicrograph of thin section 10CY-021

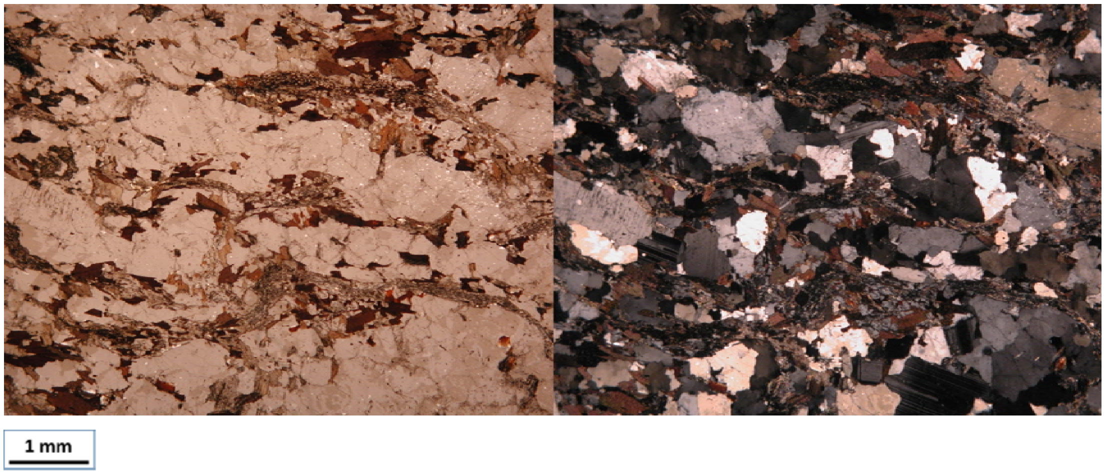

Figure B17: Photomicrograph of thin section 10CY-023

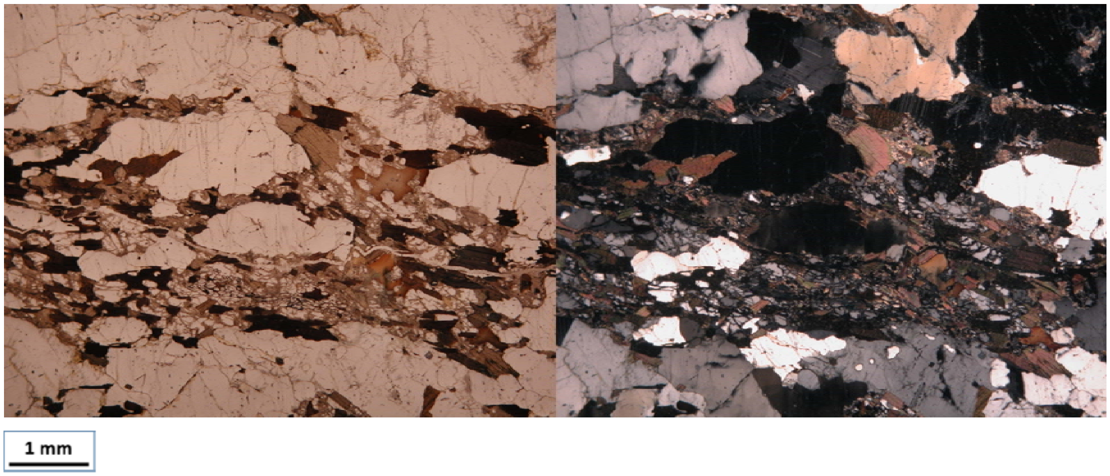

Figure B18: Photomicrograph of thin section 10CY-033

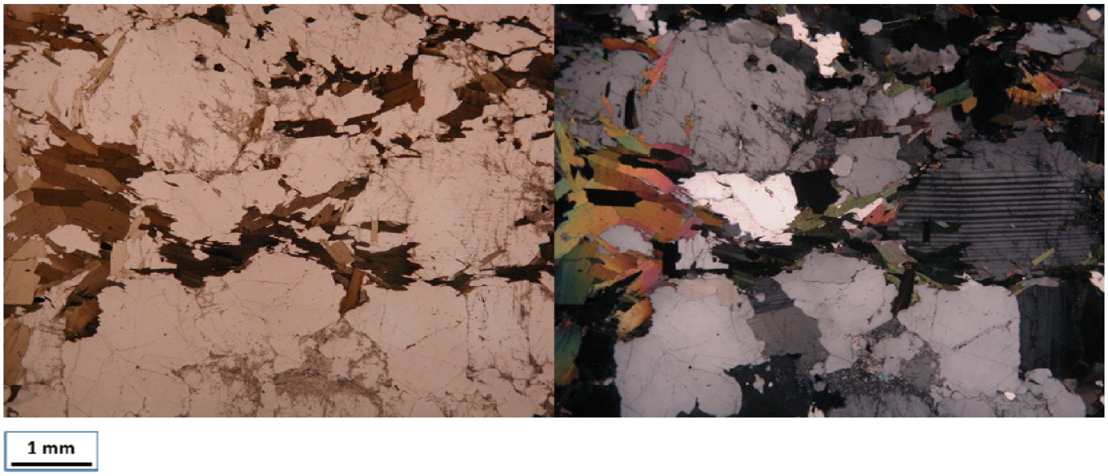

Figure B19: Photomicrograph of thin section 10CY-041

Y1-BB013

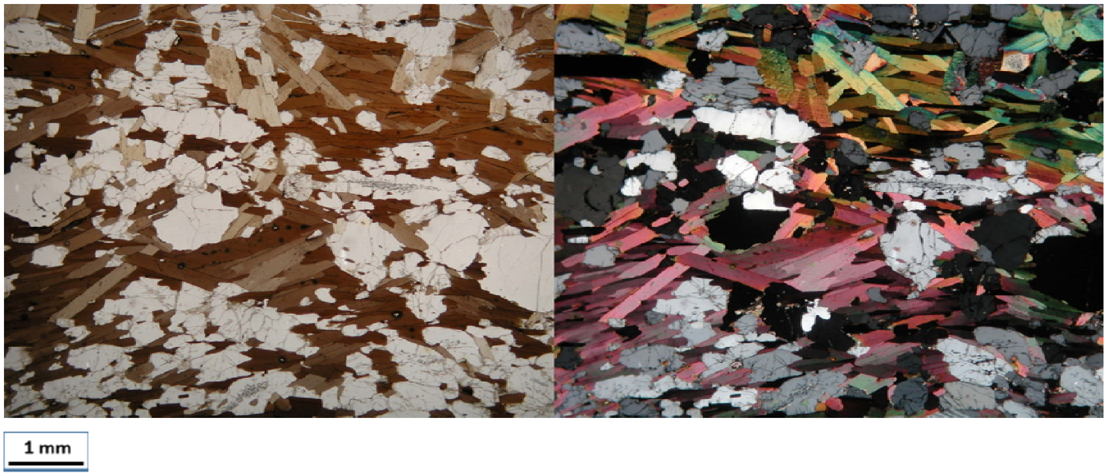

Figure B20: Photomicrograph of thin section Y1-BB013

Figure B21: Photomicrograph of thin section Y1-CB080

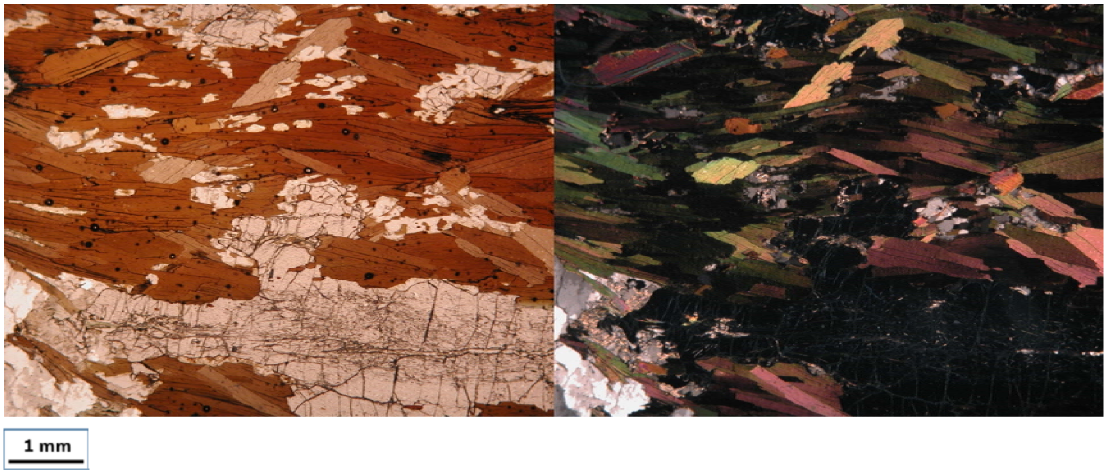

Figure B22: Photomicrograph of thin section Y1-IG057

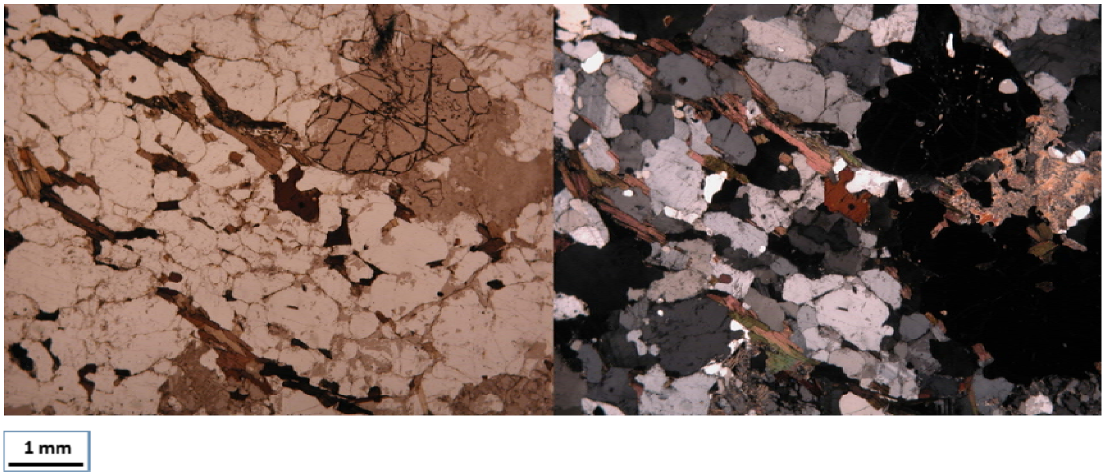

Figure B23: Photomicrograph of thin section Y1-IG061

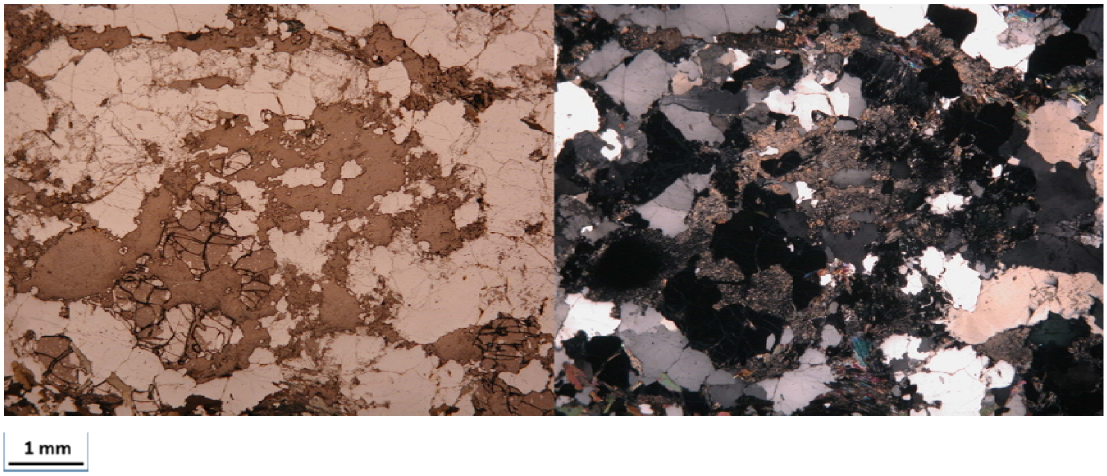

Figure B24: Photomicrograph of thin section Y1-LH077

Figure B25: Photomicrograph of thin section Y1-MJ074

Orthogneisses

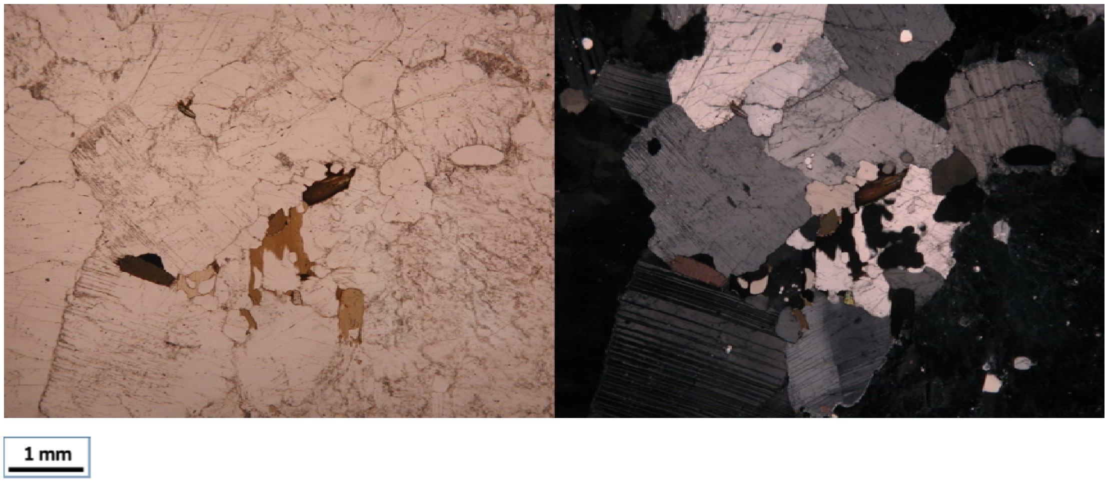

Figure B26: Photomicrograph of thin section 10CY-035

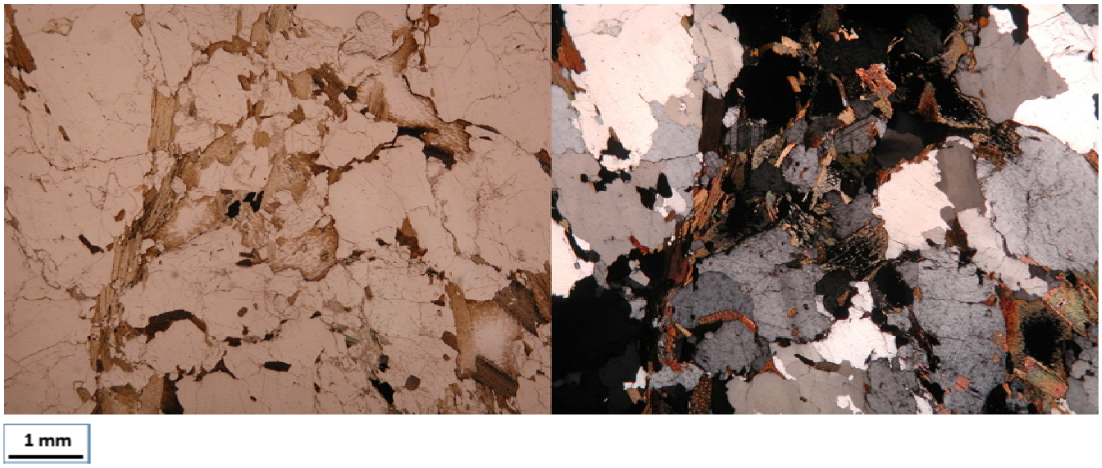

Figure B27: Photomicrograph of thin section Y1-AW039

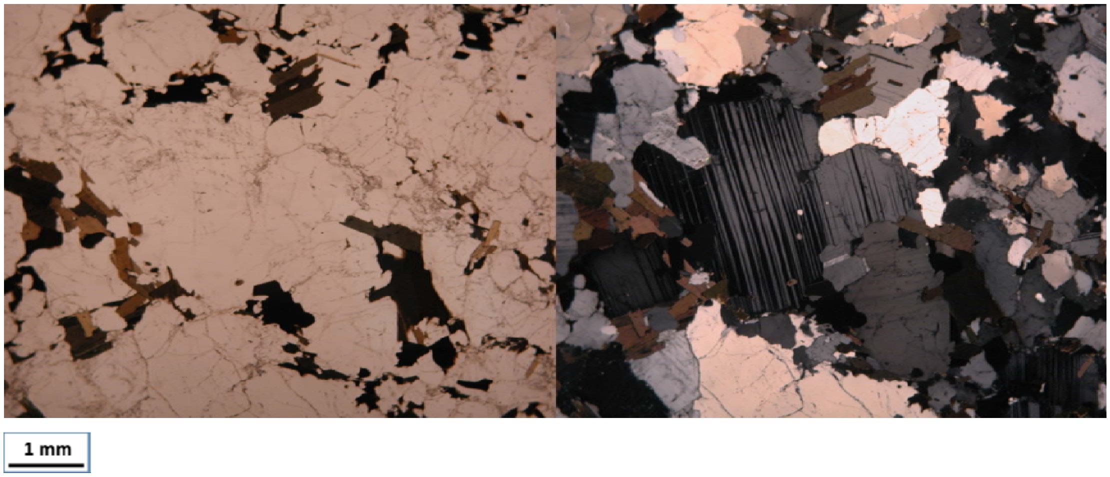

Figure B28: Photomicrograph of thin section Y1-AW049

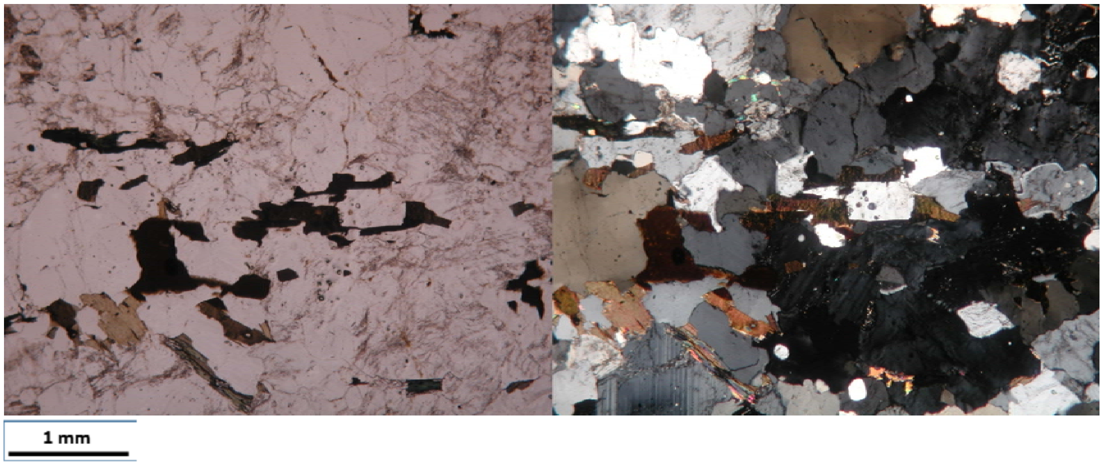

Figure B29: Photomicrograph of thin section Y1-MJ075

Devonian–Carboniferous diatexites

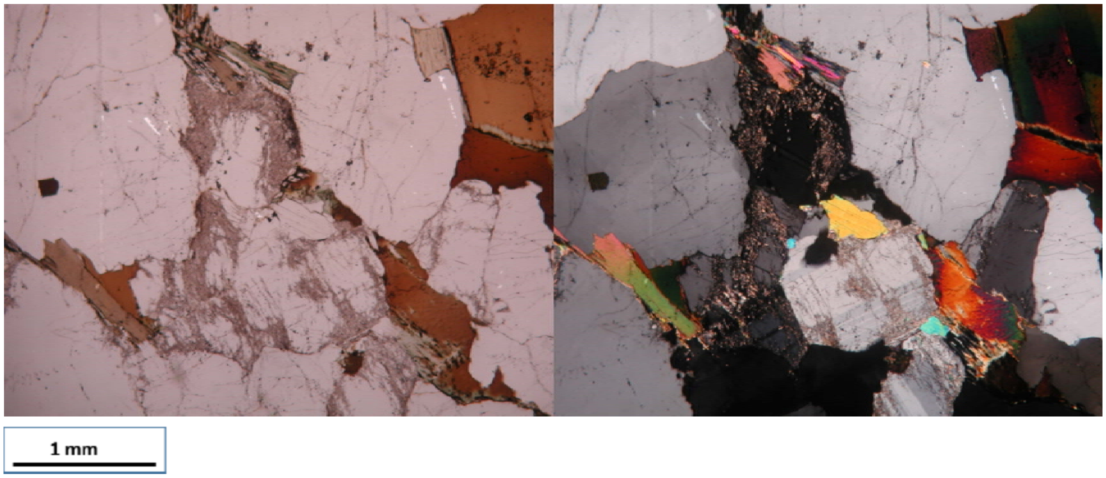

Figure B30: Photomicrograph of thin section Y1-IG071

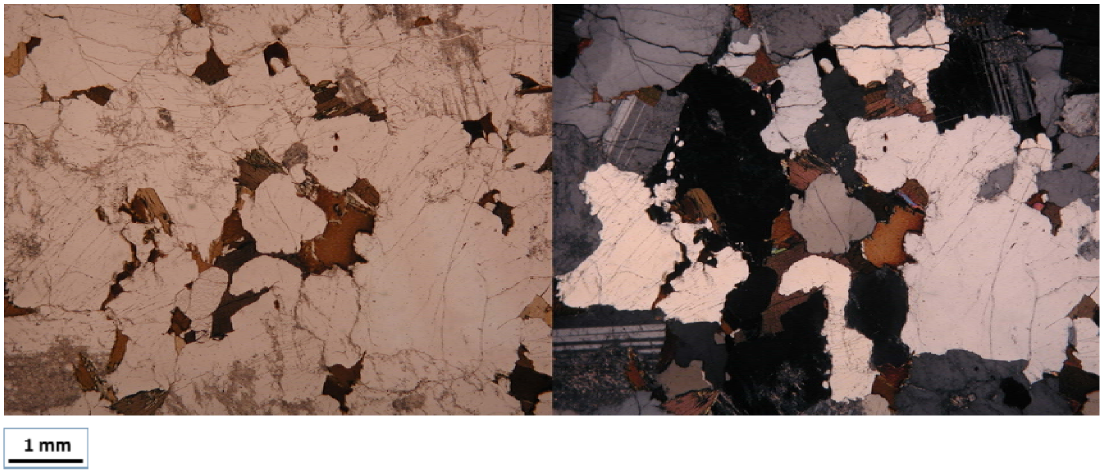

Figure B31: Photomicrograph of thin section Y1-IG073

Devonian–Carboniferous granite

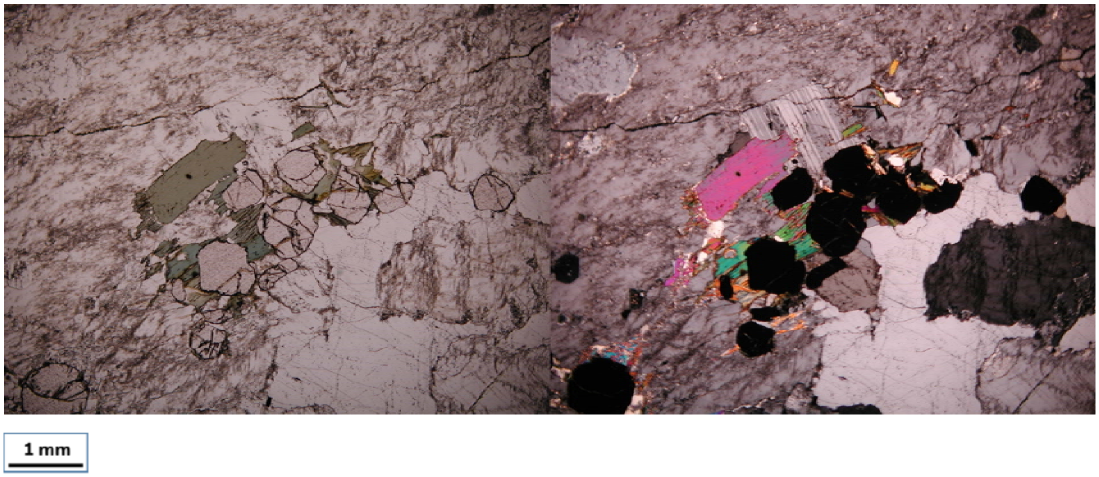

Figure B32: Photomicrograph of thin section Y1-IG062

Cretaceous granites

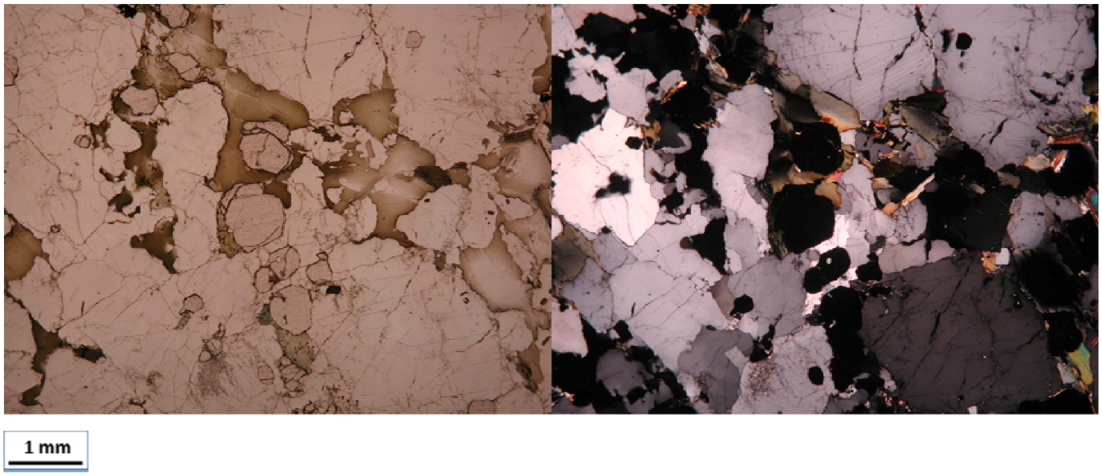

Figure B33: Photomicrograph of thin section Y1-AW038

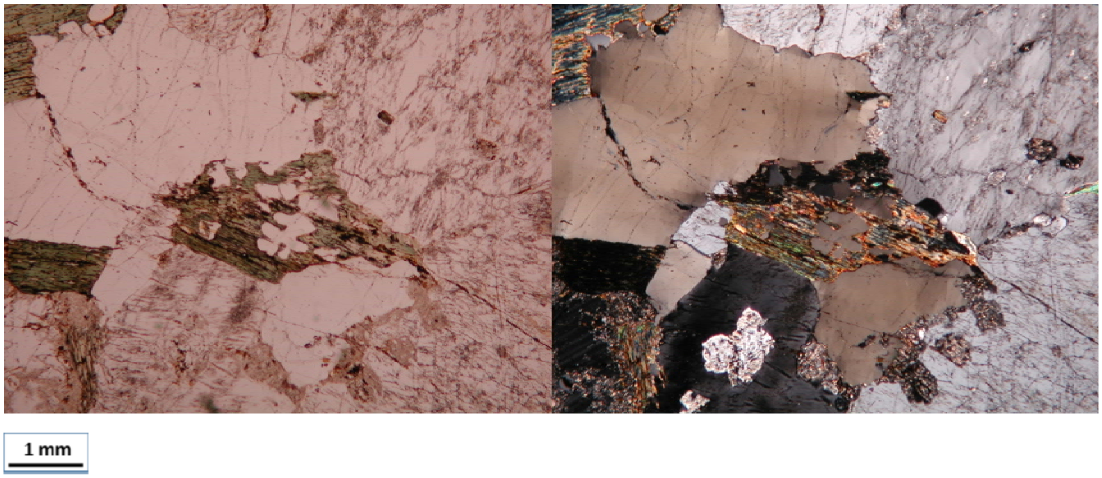

Figure B34: Photomicrograph of thin section 10CY-039

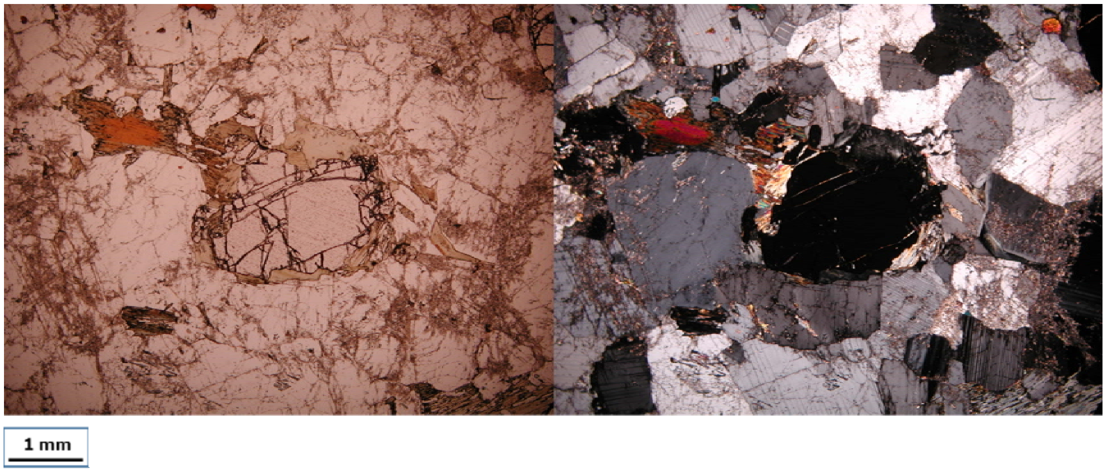

Figure B35: Photomicrograph of thin section Y1-AE051

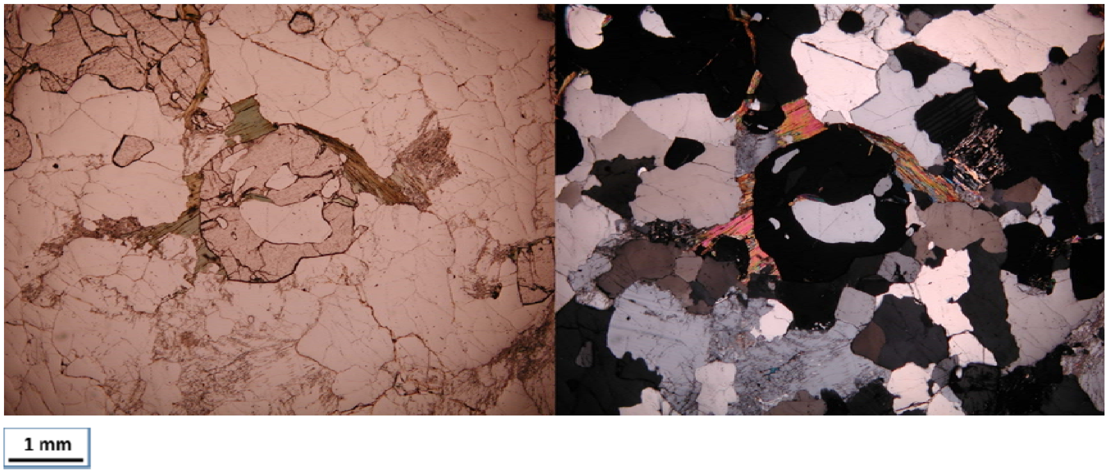

Figure B36: Photomicrograph of thin section Y1-IG052

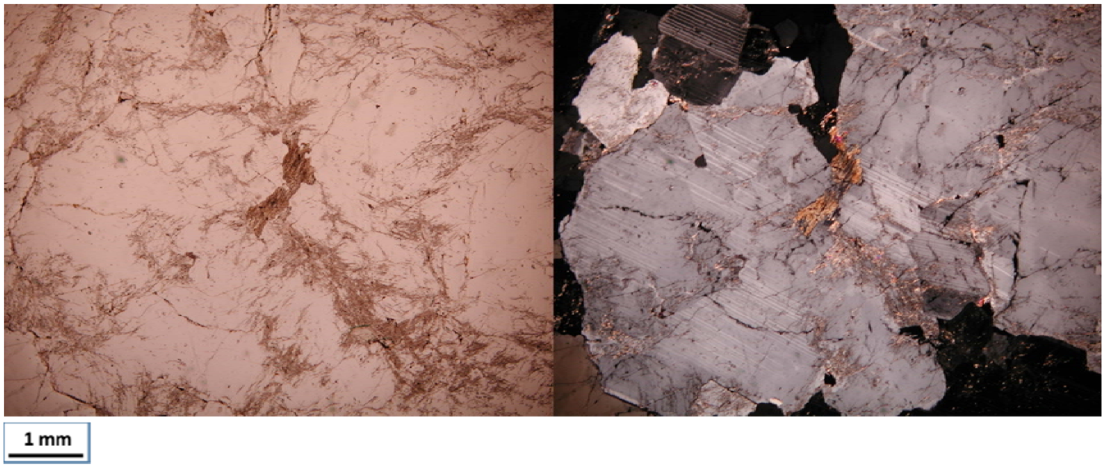

Figure B37: Photomicrograph of thin section Y1-IG070

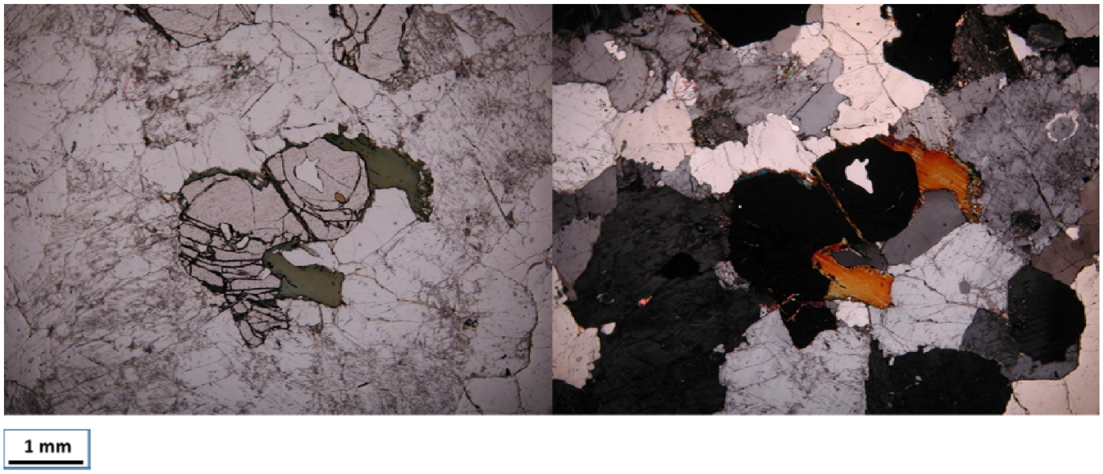

Figure B38: Photomicrograph of thin section Y1-AE064

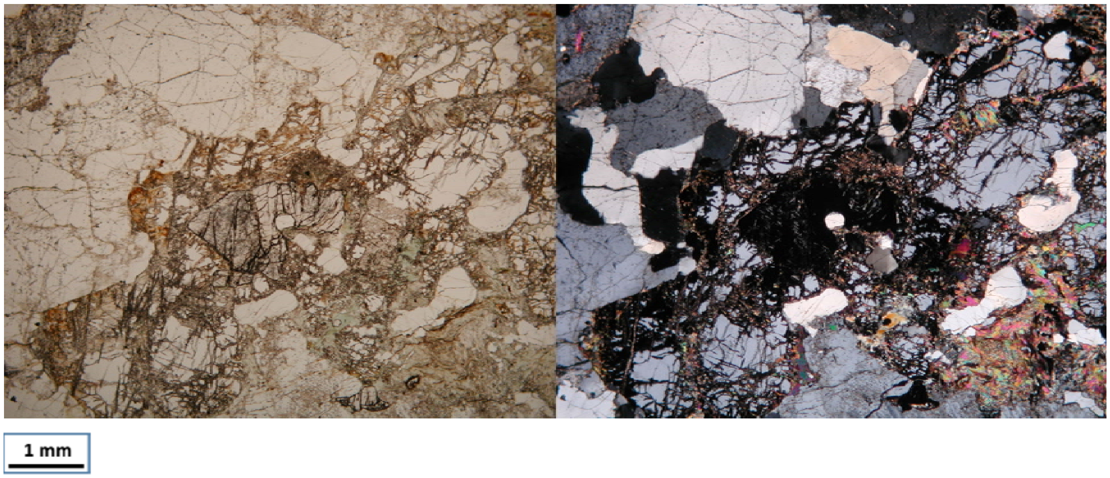

Figure B39: Photomicrograph of thin section Y1-AE033

Appendix C: Zircon U–Pb Radiogenic Ratios and Ages

Table C1: LA-ICP-MS U–Pb zircon data from sample Y1-AE035

					Radiogenic Ratios						Age (Ma)	
	Spot Size (µm)	**U (ppm)**	**Th (ppm)**	**U/Th**	**206Pb/238U**	**2σ**	**207Pb/235U**	**2σ**	**206/207 Pb**	**2σ**	**206Pb/238U**	**2σ**
Y1-AE035												
Y1-AE035_16	30	114	52	2.2	0.0537	0.0030	0.4022	0.093	337.2	62.3	337.2	18.4
Y1-AE035_1	30	180	93	1.9	0.0623	0.0018	0.4659	0.049	389.3	42.6	389.3	11.0
Y1-AE035_2	30	261	172	1.5	0.0567	0.0020	0.4182	0.026	355.8	43.1	355.8	12.2
Y1-AE035_3	30	258	119	2.2	0.0578	0.0035	0.4223	0.035	362.4	76.2	362.4	21.0
Y1-AE035_3	30	242	114	2.1	0.0588	0.0009	0.4397	0.036	368.3	20.3	368.3	5.6
Y1-AE035_5	30	207	167	1.2	0.0585	0.0013	0.4453	0.025	366.4	28.1	366.4	7.6
Y1-AE035_6	30	251	84	3.0	0.0572	0.0021	0.4187	0.039	358.6	46.0	358.6	12.8
Y1-AE035_7	30	472	481	1.0	0.0598	0.0012	0.4414	0.014	374.5	27.9	374.5	7.4
Y1-AE035_8	30	135	56	2.4	0.0599	0.0025	0.4365	0.046	374.7	57.3	374.7	15.2
Y1-AE035_9	30	310	115	2.7	0.0597	0.0022	0.4427	0.032	374.0	49.7	374.0	13.2
Y1-AE035_9	30	385	200	1.9	0.0583	0.0030	0.4402	0.033	365.1	66.3	365.1	18.2
Y1-AE035_11	30	368	99	3.7	0.0592	0.0027	0.4372	0.026	370.5	60.0	370.5	16.2
Y1-AE035_12	30	259	105	2.5	0.0613	0.0016	0.4546	0.026	383.5	37.4	383.5	9.8
Y1-AE035_13	30	149	60	2.5	0.0605	0.0031	0.4456	0.032	378.8	70.8	378.8	18.6
Y1-AE035_14	30	138	61	2.3	0.0575	0.0018	0.4334	0.046	360.6	40.2	360.6	11.2
Y1-AE035_17	30	145	63	2.3	0.0601	0.0016	0.4342	0.045	376.0	37.6	376.0	10.0
Y1-AE035_18	30	206	127	1.6	0.0593	0.0015	0.4441	0.032	371.4	34.4	371.4	9.2
Y1-AE035_19	30	137	62	2.2	0.0583	0.0020	0.4276	0.046	365.1	43.8	365.1	12.0
Y1-AE035_20	30	140	53	2.7	0.0606	0.0037	0.4395	0.062	379.4	84.9	379.4	22.4
Y1-AE035_21	30	227	107	2.1	0.0609	0.0009	0.4469	0.023	381.1	21.7	381.1	5.6
Y1-AE035_22	30	106	44	2.4	0.0584	0.0021	0.4411	0.063	365.9	46.4	365.9	12.6
Y1-AE035_23	30	240	101	2.4	0.0608	0.0020	0.4415	0.036	380.2	47.3	380.2	12.4
Y1-AE035_24	30	138	64	2.1	0.0598	0.0019	0.4446	0.064	374.2	43.3	374.2	11.6
Y1-AE035_25	30	207	168	1.2	0.0586	0.0017	0.4294	0.035	367.1	37.9	367.1	10.4

*1.3=Systematic error of 206Pb/238U age based on Sri Lankan standard

Table C2: LA-ICP-MS U–Pb zircon data from sample Y2-GP091

					Radiogenic Ratios						**Age (Ma)**	
	Spot Size (µm)	**U (ppm)**	**Th (ppm)**	**U/Th**	**206Pb/238U**	**2σ**	**207Pb/235U**	**2σ**	**206/207 Pb**	**2σ**	**206Pb/238U**	**2σ**
Y2-GP091												
Y2-GP091_23	30	156	96	1.6	0.0573	0.0016	0.4297	0.038	359.4	35.5	373.6	15.4
Y2-GP091_13	30	326	260	1.3	0.0576	0.0025	0.4309	0.023	361.2	56.0	461.6	27.7
Y2-GP091_15	30	195	93	2.1	0.0579	0.0018	0.4247	0.020	363.0	39.6	375.6	16.8
Y2-GP091_4	30	109	57	1.9	0.0580	0.0058	0.4297	0.045	363.7	127.6	363.7	35.1
Y2-GP091_14	30	100	76	1.3	0.0581	0.0017	0.4139	0.054	363.8	37.0	373.2	10.8
Y2-GP091_11	30	193	54	3.6	0.0581	0.0020	0.4225	0.033	364.0	43.3	377.1	10.9
Y2-GP091_20	30	104	69	1.5	0.0583	0.0030	0.4363	0.037	365.0	65.9	369.5	14.5
Y2-GP091_18	30	65	45	1.4	0.0584	0.0031	0.4333	0.090	366.0	68.2	367.7	23.3
Y2-GP091_19	30	105	39	2.7	0.0586	0.0043	0.4580	0.060	367.1	95.7	391.4	21.7
Y2-GP091_12	30	96	76	1.3	0.0587	0.0019	0.4475	0.047	367.6	43.2	372.7	10.4
Y2-GP091_8	30	125	126	1.0	0.0587	0.0038	0.4356	0.038	367.7	85.8	364.0	11.9
Y2-GP091_7	30	344	110	3.1	0.0590	0.0024	0.4377	0.022	369.5	53.7	367.6	11.7
Y2-GP091_17	30	110	78	1.4	0.0591	0.0035	0.4488	0.051	370.4	78.4	361.2	15.5
Y2-GP091_10	30	480	183	2.6	0.0595	0.0017	0.4466	0.016	372.7	38.9	363.8	10.2
Y2-GP091_5	30	329	364	0.91	0.0596	0.0018	0.4423	0.019	373.2	40.4	363.0	10.9
Y2-GP091_1	30	126	59	2.1	0.0597	0.0025	0.4499	0.043	373.6	57.5	380.8	24.3
Y2-GP091_22	30	225	163	1.4	0.0598	0.0043	0.4488	0.033	374.1	97.8	370.4	21.2
Y2-GP091_3	30	265	78	3.4	0.0600	0.0028	0.4425	0.025	375.6	63.1	366.0	18.6
Y2-GP091_21	30	102	68	1.5	0.0600	0.0044	0.4575	0.046	375.9	101.3	367.1	26.1
Y2-GP091_6	30	229	76	3.0	0.0602	0.0018	0.4472	0.020	377.1	41.1	365.0	18.1
Y2-GP091_16	30	233	111	2.1	0.0608	0.0040	0.4447	0.037	380.8	92.7	375.9	27.0
Y2-GP091_25	30	648	127	5.1	0.0610	0.0013	0.4549	0.010	381.8	29.4	374.1	26.2
Y2-GP091_24	30	460	120	3.8	0.0611	0.0035	0.4571	0.030	382.5	81.4	359.4	9.9
Y2-GP091_9	30	147	50	2.9	0.0626	0.0036	0.4793	0.045	391.4	85.1	382.5	21.3
Y2-GP091_2	30	160	39	4.1	0.0742	0.0046	0.6055	0.050	461.6	128.0	381.8	7.7

*1.0=Systematic error of ^{206}Pb/^{238}U age based on Sri Lankan standard

Table C3: LA-ICP-MS U–Pb zircon data from sample 51225-1

					Radiogenic Ratios						**Age (Ma)**	
	Spot Size (µm)	**U (ppm)**	**Th (ppm)**	**U/Th**	**206Pb/238U**	**2σ**	**207Pb/235U**	**2σ**	**206/207 Pb**	**2σ**	**206Pb/238U**	**2σ**
51225-1												
51225-1_2	30	337	218	1.5	0.0562	0.0046	0.4205	0.040	352.5	98.9	352.5	28.1
51225-1_6	30	1295	265	4.9	0.0563	0.0013	0.4209	0.010	352.8	28.7	352.8	8.1
51225-1_7	30	693	192	3.6	0.0573	0.0029	0.4276	0.022	359.3	63.5	359.3	17.7
51225-1_4	30	381	147	2.6	0.0575	0.0034	0.4315	0.027	360.2	75.7	360.2	21.0
51225-1_10	30	279	173	1.6	0.0581	0.0017	0.4346	0.022	363.9	37.8	363.9	10.4
51225-1_1	30	520	123	4.2	0.0581	0.0024	0.4333	0.022	364.0	53.8	364.0	14.8
51225-1_17	30	158	150	1.0	0.0581	0.0013	0.4298	0.037	364.2	28.0	364.2	7.7
51225-1_22	30	430	258	1.7	0.0582	0.0019	0.4340	0.018	364.7	42.8	364.7	11.7
51225-1_9	30	330	121	2.7	0.0589	0.0021	0.4398	0.020	368.9	46.6	368.9	12.6
51225-1_12	30	482	166	2.9	0.0590	0.0016	0.4375	0.018	369.6	36.1	369.6	9.8
51225-1_13	30	487	204	2.4	0.0593	0.0036	0.4427	0.029	371.1	82.2	371.1	22.2
51225-1_8	30	339	150	2.3	0.0596	0.0038	0.4412	0.031	373.3	86.9	373.3	23.3
51225-1_11	30	810	260	3.1	0.0597	0.0014	0.4473	0.011	373.6	32.6	373.6	8.7
51225-1_24	30	497	196	2.5	0.0597	0.0032	0.4435	0.025	373.8	71.8	373.8	19.2
51225-1_18	30	400	203	2.0	0.0600	0.0011	0.4426	0.012	375.5	24.0	375.5	6.4
51225-1_25	30	423	158	2.7	0.0602	0.0017	0.4452	0.016	377.1	39.2	377.1	10.4
51225-1_14	30	1045	158	6.6	0.0603	0.0016	0.4489	0.013	377.4	36.4	377.4	9.7
51225-1_21	30	278	112	2.5	0.0604	0.0015	0.4514	0.025	378.2	33.6	378.2	8.9
51225-1_19	30	324	111	2.9	0.0605	0.0016	0.4489	0.021	378.6	37.4	378.6	9.9
51225-1_20	30	768	194	4.0	0.0612	0.0023	0.4562	0.019	382.6	53.6	382.6	14.0
51225-1_15	30	263	94	2.8	0.0634	0.0054	0.4738	0.046	396.4	128.9	396.4	32.5
51225-1_23	30	443	124	3.6	0.0665	0.0024	0.4984	0.025	415.0	60.4	415.0	14.5
51225-1_16	30	224	166	1.4	0.0667	0.0086	0.5213	0.092	416.2	216.8	416.2	52.1
51225-1_3	30	78	53	1.5	0.1810	0.0060	1.8772	0.074	1072.4	350.2	1074.4	42.8

*1.3=Systematic error of ^{206}Pb/^{238}U age based on Sri Lankan standard

Table C4: LA-ICP-MS U–Pb zircon data from sample 51225-2

					Radiogenic Ratios						**Age (Ma)**	
	Spot Size (µm)	**U (ppm)**	**Th (ppm)**	**U/Th**	**206Pb/238U**	**2σ**	**207Pb/235U**	**2σ**	**206/207 Pb**	**2σ**	**206Pb/238U**	**2σ**
51225-2												
51225-2_2	30	778	163	4.8	0.0559	0.0032	0.4158	0.024	350.7	67.9	358.6	12.7
51225-2_4	30	641	125	5.1	0.0572	0.0011	0.4286	0.011	358.4	24.4	350.7	19.4
51225-2_1	30	505	147	3.4	0.0572	0.0021	0.4270	0.019	358.6	45.5	371.9	7.2
51225-2_5	30	537	129	4.2	0.0577	0.0013	0.4253	0.014	361.6	28.3	358.4	6.8
51225-2_6	30	452	318	1.4	0.0579	0.0016	0.4304	0.015	362.9	36.2	361.6	7.8
51225-2_18	30	645	159	4.1	0.0580	0.0011	0.4323	0.012	363.2	24.9	362.9	10.0
51225-2_21	30	766	133	5.8	0.0580	0.0015	0.4309	0.014	363.4	32.6	380.2	13.4
51225-2_13	30	368	115	3.2	0.0580	0.0018	0.4345	0.019	363.7	40.6	369.8	7.5
51225-2_11	30	639	105	6.1	0.0584	0.0012	0.4365	0.011	366.0	27.4	373.5	10.0
51225-2_19	30	1143	174	6.6	0.0585	0.0007	0.4343	0.008	366.2	16.2	368.9	10.0
51225-2_10	30	792	96	8.2	0.0589	0.0016	0.4378	0.013	368.9	36.9	366.0	7.5
51225-2_8	30	401	124	3.2	0.0590	0.0012	0.4374	0.017	369.8	27.6	378.7	7.9
51225-2_15	30	209	71	2.9	0.0594	0.0011	0.4399	0.025	371.7	24.8	363.7	11.2
51225-2_3	30	589	217	2.7	0.0594	0.0012	0.4444	0.012	371.9	26.8	383.3	25.9
51225-2_9	30	161	135	1.2	0.0597	0.0016	0.4456	0.028	373.5	37.3	371.7	6.7
51225-2_17	30	683	140	4.9	0.0597	0.0014	0.4441	0.015	374.1	32.3	377.1	7.9
51225-2_24	30	561	206	2.7	0.0602	0.0019	0.4485	0.015	376.7	42.7	374.1	8.6
51225-2_16	30	484	137	3.5	0.0602	0.0013	0.4494	0.014	377.1	29.8	363.2	6.9
51225-2_12	30	572	157	3.6	0.0605	0.0013	0.4466	0.016	378.7	29.8	366.2	4.4
51225-2_23	30	676	208	3.2	0.0606	0.0012	0.4529	0.013	379.0	28.0	385.4	25.5
51225-2_7	30	472	169	2.8	0.0608	0.0022	0.4533	0.023	380.2	50.9	363.4	9.0
51225-2_14	30	213	140	1.5	0.0613	0.0043	0.4529	0.044	383.3	99.2	379.0	7.4
51225-2_20	30	911	244	3.7	0.0616	0.0042	0.4615	0.032	385.4	98.3	376.7	11.3
51225-2_22	30	326	167	2.0	0.0818	0.0036	0.6462	0.031	506.6	109.1	506.6	21.5
51225-2_25	30	547	131	4.2	0.1254	0.0058	1.2081	0.057	761.6	253.0	761.6	33.2

Table C5: LA-ICP-MS U–Pb zircon data from sample Y2-JU096

					Radiogenic Ratios						Age (Ma)	
	Spot Size (µm)	**U (ppm)**	**Th (ppm)**	**U/Th**	**206Pb/238U**	**2σ**	**207Pb/235U**	**2σ**	**206/207 Pb**	**2σ**	**206Pb/238U**	**2σ**
Y2-JU096												
Y2-JU096_14	30	771	428	1.8	0.0499	0.0039	0.3737	0.032	313.9	75.7	364.7	15.8
Y2-JU096_7	30	582	315	1.8	0.0523	0.0048	0.3917	0.039	328.8	96.2	354.1	16.8
Y2-JU096_8	30	626	303	2.1	0.0530	0.0017	0.3967	0.016	332.7	35.1	370.2	10.6
Y2-JU096_11	30	391	264	1.5	0.0532	0.0084	0.4034	0.066	334.2	172.7	362.1	10.6
Y2-JU096_13	30	297	137	2.2	0.0542	0.0036	0.4004	0.029	340.3	74.7	369.5	12.9
Y2-JU096_24	30	264	159	1.7	0.0563	0.0051	0.4253	0.041	353.1	110.3	328.8	29.2
Y2-JU096_2	30	467	218	2.1	0.0565	0.0028	0.4234	0.026	354.1	59.5	332.7	10.6
Y2-JU096_10	30	721	444	1.6	0.0575	0.0017	0.4263	0.014	360.1	37.4	366.7	6.6
Y2-JU096_25	30	382	320	1.2	0.0577	0.0043	0.4314	0.036	361.7	94.2	360.1	10.4
Y2-JU096_22	30	475	315	1.5	0.0577	0.0019	0.4295	0.019	361.8	42.2	334.2	51.7
Y2-JU096_23	30	472	271	1.7	0.0578	0.0011	0.4284	0.012	362.0	25.2	371.2	17.8
Y2-JU096_4	30	360	205	1.8	0.0578	0.0017	0.4370	0.021	362.1	38.2	340.3	21.9
Y2-JU096_15	30	335	187	1.8	0.0581	0.0020	0.4318	0.018	364.2	45.4	313.9	24.1
Y2-JU096_21	30	650	372	1.8	0.0582	0.0032	0.4320	0.025	364.7	70.2	364.2	12.5
Y2-JU096_1	30	617	414	1.5	0.0582	0.0026	0.4310	0.023	364.7	57.7	368.1	9.9
Y2-JU096_9	30	407	190	2.1	0.0585	0.0011	0.4327	0.015	366.7	24.2	389.0	15.5
Y2-JU096_16	30	209	145	1.4	0.0588	0.0016	0.4381	0.024	368.1	36.6	364.7	19.2
Y2-JU096_6	30	258	98	2.6	0.0590	0.0021	0.4412	0.020	369.5	47.8	361.8	11.7
Y2-JU096_3	30	342	186	1.8	0.0591	0.0017	0.4466	0.021	370.2	39.3	362.0	7.0
Y2-JU096_12	30	288	131	2.2	0.0593	0.0029	0.4346	0.025	371.2	66.2	353.1	31.2
Y2-JU096_20	30	394	187	2.1	0.0622	0.0026	0.4836	0.029	389.0	60.3	361.7	26.1

*1.0=Systematic error of ^{206}Pb/^{238}U age based on Sri Lankan standard

Table C6: LA-ICP-MS U–Pb zircon data from sample Y1-AW039

					Radiogenic Ratios						Age (Ma)	
	Spot Size (µm)	**U (ppm)**	**Th (ppm)**	**U/Th**	**206Pb/238U**	**2σ**	**207Pb/235U**	**2σ**	**206/207 Pb**	**2σ**	**206Pb/238U**	**2σ**
Y1-AW039												
Y1-AW039_11	30	171.969	61.19063	2.8104	0.0429	0.0024	0.3158	0.027	270.7	40.6	350.5	22.9
Y1-AW039_14	30	616.761	58.70103	10.507	0.0441	0.0073	0.3162	0.055	278.3	125.2	351.3	20.8
Y1-AW039_25	30	508.902	109.7093	4.6386	0.0512	0.0026	0.3801	0.021	322.2	51.8	395.4	29.1
Y1-AW039_1	30	403.55	84.76941	4.7606	0.0559	0.0037	0.4180	0.030	350.5	80.2	363.5	9.9
Y1-AW039_2	30	139.42	82.12934	1.6976	0.0560	0.0034	0.4179	0.039	351.3	73.2	377.0	8.9
Y1-AW039_10	30	350.907	97.519	3.5983	0.0577	0.0025	0.4326	0.022	361.5	55.5	370.5	13.0
Y1-AW039_24	30	154.451	127.1083	1.2151	0.0579	0.0019	0.4337	0.026	363.0	42.8	365.2	13.6
Y1-AW039_4	30	396.191	95.67819	4.1409	0.0580	0.0016	0.4328	0.017	363.5	36.0	372.6	10.0
Y1-AW039_18	30	282.262	117.0235	2.412	0.0581	0.0029	0.4377	0.037	364.1	64.1	382.0	17.7
Y1-AW039_7	30	107.181	65.46837	1.6371	0.0583	0.0022	0.4353	0.039	365.2	49.5	361.5	15.3
Y1-AW039_21	30	163.014	64.3179	2.5345	0.0587	0.0028	0.4389	0.033	367.4	62.4	270.7	15.0
Y1-AW039_23	30	459.21	119.5613	3.8408	0.0587	0.0026	0.4372	0.021	367.6	58.5	429.9	49.8
Y1-AW039_13	30	112.775	76.05766	1.4828	0.0591	0.0019	0.4361	0.044	370.0	41.8	370.0	11.3
Y1-AW039_6	30	441.756	159.7709	2.7649	0.0592	0.0021	0.4431	0.018	370.5	48.2	415.3	62.0
Y1-AW039_8	30	425.782	233.7478	1.8215	0.0595	0.0016	0.4453	0.021	372.6	37.1	278.3	45.0
Y1-AW039_17	30	174.381	122.5009	1.4235	0.0597	0.0031	0.4450	0.037	373.7	71.2	373.7	19.0
Y1-AW039_5	30	443.732	105.4176	4.2093	0.0602	0.0015	0.4506	0.014	377.0	33.5	364.1	17.6
Y1-AW039_9	30	83.8121	55.15553	1.5196	0.0611	0.0029	0.4440	0.064	382.0	67.7	367.4	17.0
Y1-AW039_22	30	260.262	107.2714	2.4262	0.0630	0.0038	0.4650	0.036	393.6	90.9	393.6	23.1
Y1-AW039_3	30	197.892	84.02775	2.3551	0.0633	0.0048	0.4738	0.042	395.4	115.1	367.6	15.9
Y1-AW039_14	30	293.144	101.0806	2.9001	0.0665	0.0103	0.4892	0.077	415.3	257.4	363.0	11.8
Y1-AW039_12	30	355.994	93.1319	3.8225	0.0690	0.0083	0.5126	0.062	429.9	214.0	322.2	16.1

*1.1=Systematic error of 206Pb/238U age based on Sri Lankan standard

Table C7: LA-ICP-MS U–Pb zircon data from sample Y1-IG053

					Radiogenic Ratios						**Age (Ma)**	
	Spot Size (µm)	**U (ppm)**	**Th (ppm)**	**U/Th**	**206Pb/238U**	**2σ**	**207Pb/235U**	**2σ**	**206/207 Pb**	**2σ**	**206Pb/238U**	**2σ**
Y1-IG053												
Y1-IG053_23	30	214	92	2.3	0.0536	0.0088	0.3982	0.095	336.8	180.8	349.7	16.9
Y1-IG053_17	30	246	180	1.4	0.0547	0.0023	0.4122	0.034	343.1	47.4	368.1	9.2
Y1-IG053_20	30	170	67	2.5	0.0548	0.0041	0.4364	0.061	343.8	85.6	365.5	11.9
Y1-IG053_22	30	293	151	1.9	0.0556	0.0031	0.4232	0.041	348.9	65.5	391.2	15.4
Y1-IG053_1	30	170	76	2.2	0.0557	0.0028	0.4107	0.042	349.7	58.9	382.7	8.8
Y1-IG053_10	30	152	127	1.2	0.0562	0.0048	0.4250	0.053	352.5	103.2	367.1	7.2
Y1-IG053_18	30	189	118	1.6	0.0568	0.0022	0.4258	0.034	356.3	48.1	373.8	28.8
Y1-IG053_21	30	235	184	1.3	0.0570	0.0022	0.4254	0.038	357.4	47.2	382.4	21.7
Y1-IG053_14	30	242	126	1.9	0.0570	0.0025	0.4184	0.022	357.6	54.0	358.6	30.9
Y1-IG053_9	30	353	196	1.8	0.0572	0.0051	0.4247	0.039	358.6	110.7	352.5	29.3
Y1-IG053_12	30	110	56	2.0	0.0577	0.0025	0.4069	0.087	361.4	55.9	375.3	15.1
Y1-IG053_16	30	329	159	2.1	0.0581	0.0044	0.4384	0.044	364.1	97.2	361.4	15.5
Y1-IG053_3	30	473	291	1.6	0.0583	0.0020	0.4330	0.020	365.5	43.5	427.9	17.6
Y1-IG053_6	30	367	333	1.1	0.0586	0.0012	0.4226	0.025	367.1	26.6	357.6	15.1
Y1-IG053_15	30	245	160	1.5	0.0586	0.0029	0.4366	0.030	367.1	65.4	367.1	17.8
Y1-IG053_2	30	241	213	1.1	0.0588	0.0015	0.4311	0.022	368.1	33.8	364.1	26.7
Y1-IG053_19	30	271	103	2.6	0.0588	0.0017	0.4338	0.024	368.5	38.2	343.1	13.8
Y1-IG053_7	30	489	323	1.5	0.0597	0.0047	0.4482	0.038	373.8	107.8	356.3	13.5
Y1-IG053_11	30	136	74	1.8	0.0599	0.0025	0.4518	0.052	375.3	56.7	368.5	10.4
Y1-IG053_8	30	428	268	1.6	0.0611	0.0036	0.4554	0.035	382.4	83.0	343.8	24.9
Y1-IG053_5	30	282	130	2.2	0.0612	0.0015	0.4632	0.034	382.7	33.8	357.4	13.2
Y1-IG053_24	30	378	273	1.4	0.0615	0.0025	0.4475	0.029	385.0	59.6	348.9	18.8
Y1-IG053_4	30	374	148	2.5	0.0626	0.0025	0.4636	0.024	391.2	60.2	336.8	53.7
Y1-IG053_13	30	249	140	1.8	0.0686	0.0029	0.5066	0.036	427.9	75.4	385.0	15.5

*0.9=Systematic error of ^{206}Pb/^{238}U age based on Sri Lankan standard

Table C8: LA-ICP-MS U–Pb zircon data from sample Y1-AW049

					Radiogenic Ratios						Age (Ma)	
	Spot Size (µm)	**U (ppm)**	**Th (ppm)**	**U/Th**	**206Pb/238U**	**2σ**	**207Pb/235U**	**2σ**	**206/207 Pb**	**2σ**	**206Pb/238U**	**2σ**
Y1-AW049												
Y1-AW049_8	30	441	272	1.6	0.0550	0.0049	0.4191	0.050	344.9	103.2	371.6	12.0
Y1-AW049_15	30	721	421	1.7	0.0556	0.0014	0.4140	0.013	348.5	29.0	367.6	15.0
Y1-AW049_23	30	436	277	1.6	0.0556	0.0022	0.4126	0.024	349.1	47.7	371.6	32.7
Y1-AW049_18	30	171	114	1.5	0.0558	0.0035	0.3980	0.042	349.8	75.1	369.3	8.4
Y1-AW049_12	30	247	238	1.0	0.0562	0.0046	0.4158	0.046	352.3	98.0	392.9	44.0
Y1-AW049_9	30	241	120	2.0	0.0569	0.0036	0.4254	0.038	357.0	78.8	344.9	29.9
Y1-AW049_11	30	183	95	1.9	0.0570	0.0028	0.4308	0.045	357.2	61.0	357.0	22.1
Y1-AW049_13	30	682	221	3.1	0.0571	0.0025	0.4284	0.021	358.0	54.2	360.1	22.5
Y1-AW049_25	30	254	111	2.3	0.0572	0.0060	0.4173	0.068	358.5	132.2	357.2	17.1
Y1-AW049_10	30	549	164	3.4	0.0575	0.0037	0.4239	0.029	360.1	81.0	352.3	27.8
Y1-AW049_4	30	182	130	1.4	0.0587	0.0025	0.4345	0.052	367.6	55.2	358.0	15.1
Y1-AW049_6	30	637	199	3.2	0.0590	0.0014	0.4392	0.012	369.3	31.1	348.5	8.3
Y1-AW049_5	30	310	127	2.4	0.0593	0.0054	0.4409	0.050	371.6	121.6	374.6	21.8
Y1-AW049_1	30	243	182	1.3	0.0593	0.0020	0.4382	0.027	371.6	44.5	349.8	21.5
Y1-AW049_17	30	753	290	2.6	0.0598	0.0036	0.4459	0.030	374.6	81.5	411.5	30.1
Y1-AW049_24	30	159	92	1.7	0.0602	0.0033	0.4484	0.049	376.6	75.9	378.0	25.6
Y1-AW049_20	30	85	51	1.7	0.0604	0.0042	0.4612	0.077	378.0	96.6	382.7	48.9
Y1-AW049_21	30	830	153	5.4	0.0612	0.0081	0.4421	0.061	382.7	187.2	349.1	13.7
Y1-AW049_7	30	208	90	2.3	0.0628	0.0073	0.4835	0.074	392.9	172.8	376.6	20.2
Y1-AW049_19	30	164	128	1.3	0.0659	0.0050	0.5000	0.064	411.5	124.0	358.5	36.9

*0.9=Systematic error of ^{206}Pb/^{238}U age based on Sri Lankan standard

Table C9: LA-ICP-MS U–Pb zircon data from sample 10CY-035

					Radiogenic Ratios						Age (Ma)	
	Spot Size (µm)	**U (ppm)**	**Th (ppm)**	**U/Th**	**206Pb/238U**	**2σ**	**207Pb/235U**	**2σ**	**206/207 Pb**	**2σ**	**206Pb/238U**	**2σ**
10CY035												
10CY-035_23	30	917	63	14.6	0.0174	0.0011	0.1158	0.009	111.2	7.9	296.4	9.1
10CY-035_14	30	1948	191	10.2	0.0177	0.0006	0.1193	0.004	113.1	4.0	294.0	10.3
10CY-035_10	30	1205	107	11.3	0.0183	0.0005	0.1224	0.005	117.0	3.9	287.5	17.9
10CY-035_20	30	582	8	70.9	0.0183	0.0008	0.1214	0.007	117.0	6.1	366.6	16.4
10CY-035_21	30	771	17	46.7	0.0281	0.0012	0.1950	0.010	178.6	13.6	367.3	23.8
10CY-035_4	30	647	204	3.2	0.0456	0.0029	0.3354	0.023	287.5	51.5	348.5	16.6
10CY-035_3	30	483	109	4.4	0.0467	0.0017	0.3440	0.018	294.0	30.2	304.0	12.2
10CY-035_1	30	929	111	8.4	0.0470	0.0015	0.3430	0.011	296.4	26.8	117.0	3.3
10CY-035_9	30	851	114	7.5	0.0483	0.0020	0.3553	0.016	304.0	37.0	386.4	33.3
10CY-035_25	30	841	18	46.5	0.0484	0.0041	0.3590	0.030	304.9	76.7	359.2	39.0
10CY-035_19	30	544	55	10.0	0.0495	0.0013	0.3670	0.018	311.5	24.7	363.2	14.4
10CY-035_8	30	152	77	2.0	0.0555	0.0027	0.4078	0.046	348.5	57.9	113.1	3.5
10CY-035_12	30	635	310	2.0	0.0573	0.0064	0.4286	0.049	359.2	140.0	379.9	8.6
10CY-035_24	30	2518	437	5.8	0.0574	0.0011	0.4311	0.011	360.0	24.6	311.5	7.9
10CY-035_13	30	92	66	1.4	0.0580	0.0024	0.4252	0.047	363.2	52.2	117.0	5.2
10CY-035_5	30	530	249	2.1	0.0585	0.0027	0.4371	0.022	366.6	60.0	178.6	7.6
10CY-035_7	30	1210	391	3.1	0.0586	0.0039	0.4340	0.029	367.3	87.6	111.2	7.1
10CY-035_18	30	1513	514	2.9	0.0607	0.0014	0.4522	0.011	379.9	32.7	360.0	6.8
10CY-035_11	30	527	289	1.8	0.0618	0.0055	0.4625	0.043	386.4	128.6	304.9	25.2

*1.1=Systematic error of 206Pb/238U age based on Sri Lankan standard

Table C10: LA-ICP-MS U–Pb zircon data from sample Y1-MJ075

					Radiogenic Ratios						**Age (Ma)**	
	Spot Size (µm)	**U (ppm)**	**Th (ppm)**	**U/Th**	**206Pb/238U**	**2σ**	**207Pb/235U**	**2σ**	**206/207 Pb**	**2σ**	**206Pb/238U**	**2σ**
Y1-MJ075												
Y1-MJ075_15	30	388	319	1.2	0.0172	0.0012	0.1177	0.013	110.0	8.2	110.0	7.5
Y1-MJ075_9	30	712	665	1.1	0.0176	0.0006	0.1159	0.007	112.4	4.6	112.4	4.1
Y1-MJ075_7	30	587	351	1.7	0.0177	0.0015	0.1227	0.019	112.8	10.7	112.8	9.5
Y1-MJ075_5	30	555	346	1.6	0.0180	0.0005	0.1280	0.015	114.9	3.5	114.9	3.0
Y1-MJ075_18	30	668	789	0.8	0.0180	0.0019	0.1227	0.020	115.2	13.9	115.2	12.1
Y1-MJ075_13	30	472	307	1.5	0.0189	0.0007	0.1268	0.014	120.9	5.1	120.9	4.2
Y1-MJ075_20	30	475	190	2.5	0.0191	0.0015	0.1303	0.014	122.1	11.6	122.1	9.5
Y1-MJ075_12	30	574	342	1.7	0.0233	0.0013	0.1575	0.012	148.4	11.9	148.4	8.0
Y1-MJ075_19	30	1088	90	12.1	0.0375	0.0042	0.2756	0.032	237.2	61.5	237.2	25.9
Y1-MJ075_6	30	491	68	7.2	0.0509	0.0060	0.4132	0.050	320.2	117.5	320.2	36.7
Y1-MJ075_1	30	306	183	1.7	0.0561	0.0018	0.4229	0.021	351.6	39.3	351.6	11.2
Y1-MJ075_14	30	163	99	1.6	0.0565	0.0024	0.4133	0.029	354.0	50.2	354.0	14.2
Y1-MJ075_17	30	295	128	2.3	0.0576	0.0045	0.4275	0.045	361.2	99.8	361.2	27.6
Y1-MJ075_8	30	211	121	1.7	0.0751	0.0020	0.5913	0.038	466.7	54.7	466.7	11.7
Y1-MJ075_2	30	384	38	10.1	0.2401	0.0149	3.1317	0.208	1387.2	1066.6	1520.1	46.1

*1.0=Systematic error of 206Pb/238U age based on Sri Lankan standard

Table C11: LA-ICP-MS U–Pb zircon data from sample Y1-IG073

					Radiogenic Ratios						Age (Ma)	
	Spot Size (µm)	**U (ppm)**	**Th (ppm)**	**U/Th**	**206Pb/238U**	**2σ**	**207Pb/235U**	**2σ**	**206/207 Pb**	**2σ**	**206Pb/238U**	**2σ**
Y1-IG073												
Y1-IG073_20	30	268	20	13.1	0.0516	0.0094	0.3865	0.077	324.5	187.6	376.2	13.9
Y1-IG073_09	30	375	36	10.4	0.0534	0.0027	0.3994	0.029	335.2	54.3	359.3	20.4
Y1-IG073_05	30	128	64	2.0	0.0554	0.0034	0.3979	0.046	347.7	73.7	379.4	12.1
Y1-IG073_11	30	249	59	4.2	0.0558	0.0029	0.4122	0.036	350.3	62.4	369.9	12.0
Y1-IG073_08	30	317	38	8.3	0.0559	0.0048	0.4062	0.040	350.5	101.6	347.7	21.2
Y1-IG073_24	30	77	48	1.6	0.0565	0.0041	0.4045	0.085	354.1	87.1	371.5	15.4
Y1-IG073_14	30	276	197	1.4	0.0566	0.0025	0.4232	0.028	354.7	53.2	356.4	13.6
Y1-IG073_13	30	525	81	6.5	0.0566	0.0010	0.4208	0.015	355.1	22.7	350.5	29.0
Y1-IG073_07	30	274	53	5.2	0.0568	0.0023	0.4197	0.028	356.4	48.5	335.2	16.3
Y1-IG073_22	30	242	65	3.7	0.0571	0.0010	0.4242	0.039	358.0	22.2	371.3	19.8
Y1-IG073_02	30	127	49	2.6	0.0573	0.0033	0.4208	0.065	359.3	73.3	350.3	17.7
Y1-IG073_12	30	197	42	4.7	0.0574	0.0018	0.4236	0.034	359.7	40.3	359.7	11.2
Y1-IG073_19	30	311	58	5.4	0.0574	0.0011	0.4267	0.023	360.0	25.2	355.1	6.3
Y1-IG073_18	30	112	70	1.6	0.0580	0.0020	0.4361	0.072	363.6	42.9	354.7	15.0
Y1-IG073_16	30	115	88	1.3	0.0581	0.0023	0.4271	0.044	364.3	52.5	365.7	7.7
Y1-IG073_15	30	525	75	7.0	0.0584	0.0013	0.4331	0.016	365.7	28.5	364.3	14.4
Y1-IG073_04	30	173	192	0.9	0.0591	0.0020	0.4532	0.035	369.9	44.4	413.7	38.1
Y1-IG073_10	30	168	40	4.2	0.0593	0.0032	0.4324	0.053	371.3	73.5	363.6	11.7
Y1-IG073_06	30	180	39	4.6	0.0593	0.0025	0.4334	0.032	371.5	57.2	360.0	6.9
Y1-IG073_23	30	111	69	1.6	0.0599	0.0018	0.4276	0.063	374.8	39.7	324.5	57.8
Y1-IG073_01	30	332	63	5.3	0.0601	0.0023	0.4508	0.032	376.2	51.9	358.0	6.3
Y1-IG073_03	30	331	24	13.6	0.0606	0.0019	0.4456	0.022	379.4	45.5	374.8	10.6
Y1-IG073_25	30	818	210	3.9	0.0614	0.0033	0.4581	0.026	383.9	76.8	354.1	24.6
Y1-IG073_17	30	226	61	3.7	0.0663	0.0064	0.4891	0.059	413.7	158.0	383.9	20.0

*1.2=Systematic error of 206Pb/238U age based on Sri Lankan standard

Table C12: LA-ICP-MS U–Pb zircon data from sample Y1-IG071

					Radiogenic Ratios						Age (Ma)	
	Spot Size (µm)	**U (ppm)**	**Th (ppm)**	**U/Th**	**206Pb/238U**	**2σ**	**207Pb/235U**	**2σ**	**206/207 Pb**	**2σ**	**206Pb/238U**	**2σ**
Y1-IG071												
Y1-IG071_11	30	1032	42	24	0.0165	0.0003	0.1106	0.005	105.5	2.3	425.7	18.2
Y1-IG071_11	30	1491	57	26	0.0165	0.0004	0.1096	0.004	105.8	2.5	766.1	19.8
Y1-IG071_3	30	756	17	44	0.0223	0.0024	0.1528	0.020	142.3	21.9	142.3	15.4
Y1-IG071_9	30	765	7	108	0.0233	0.0009	0.1632	0.008	148.7	8.3	439.2	9.6
Y1-IG071_25	30	1084	31	35	0.0275	0.0006	0.1918	0.007	175.0	6.7	212.0	9.0
Y1-IG071_5	30	1142	28	41	0.0334	0.0014	0.2377	0.011	212.0	19.1	358.4	15.9
Y1-IG071_17	30	624	5	123	0.0410	0.0016	0.2980	0.013	259.3	24.9	321.6	7.2
Y1-IG071_14	30	673	243	2.8	0.0442	0.0035	0.3238	0.027	279.1	61.4	411.9	19.2
Y1-IG071_19	30	951	5	194	0.0502	0.0015	0.3686	0.012	315.5	28.4	148.7	5.5
Y1-IG071_7	30	1068	7	151	0.0512	0.0012	0.3831	0.010	321.6	23.2	334.5	7.7
Y1-IG071_12	30	933	8	113	0.0514	0.0018	0.3838	0.015	323.1	34.9	105.5	2.2
Y1-IG071_10	30	1123	12	93	0.0533	0.0013	0.3944	0.010	334.5	25.4	105.8	2.3
Y1-IG071_16	30	1225	5	272	0.0552	0.0016	0.4084	0.013	346.5	34.7	323.1	10.8
Y1-IG071_21	30	1139	4	308	0.0556	0.0016	0.4124	0.013	349.1	32.8	364.1	10.8
Y1-IG071_18	30	911	231	3.9	0.0564	0.0016	0.4248	0.015	353.9	34.7	279.1	21.9
Y1-IG071_6	30	1032	24	44	0.0572	0.0026	0.4227	0.020	358.4	57.3	579.6	29.2
Y1-IG071_20	30	406	40	10	0.0580	0.0015	0.4368	0.018	363.4	34.2	346.5	10.0
Y1-IG071_13	30	421	149	2.8	0.0581	0.0018	0.4269	0.016	364.1	39.3	259.3	9.7
Y1-IG071_23	30	216	183	1.2	0.0618	0.0027	0.4583	0.031	386.8	64.2	353.9	9.8
Y1-IG071_8	30	573	13	45	0.0660	0.0032	0.5206	0.026	411.9	79.1	315.5	9.0
Y1-IG071_1	30	629	59	11	0.0683	0.0030	0.5345	0.024	425.7	77.5	363.4	9.4
Y1-IG071_4	30	693	45	15	0.0705	0.0016	0.5528	0.015	439.2	42.2	349.1	9.5
Y1-IG071_15	30	685	143	4.8	0.0941	0.0050	0.7802	0.042	579.6	169.2	386.8	16.6
Y1-IG071_2	30	235	14	17	0.1262	0.0035	1.1937	0.041	766.1	151.7	175.0	3.7

*1.0=Systematic error of ^{206}Pb/^{238}U age based on Sri Lankan standard

Table C13: LA-ICP-MS U–Pb zircon data from sample Y1-IG062

					Radiogenic Ratios						Age (Ma)	
	Spot Size (µm)	**U (ppm)**	**Th (ppm)**	**U/Th**	**206Pb/238U**	**2σ**	**207Pb/235U**	**2σ**	**206/207 Pb**	**2σ**	**206Pb/238U**	**2σ**
Y1-IG062												
Y1-IG062_1	30	643	7.3	88	0.0159	0.0014	0.1060	0.014	102.0	8.9	102.0	8.8
Y1-IG062_16	30	1213	6.9	175	0.0205	0.0017	0.1389	0.012	130.6	13.7	352.8	7.2
Y1-IG062_11	30	1074	10	103	0.0229	0.0008	0.1566	0.008	145.7	7.4	356.8	14.6
Y1-IG062_24	30	1184	8	144	0.0476	0.0023	0.3482	0.019	299.5	41.5	386.1	23.1
Y1-IG062_14	30	167	48	3.5	0.0479	0.0046	0.3462	0.049	301.9	84.9	369.1	6.5
Y1-IG062_4	30	130	27	4.8	0.0563	0.0012	0.4223	0.058	352.8	25.4	369.5	20.7
Y1-IG062_5	30	788	61	13	0.0569	0.0024	0.4246	0.019	356.8	51.9	359.7	13.8
Y1-IG062_15	30	1054	41	25	0.0571	0.0012	0.4220	0.011	357.8	26.5	145.7	5.0
Y1-IG062_10	30	1284	67	19	0.0574	0.0023	0.4244	0.017	359.7	49.5	371.1	11.4
Y1-IG062_23	30	1865	119	16	0.0580	0.0014	0.4331	0.011	363.3	31.1	365.3	6.6
Y1-IG062_25	30	1221	52	24	0.0582	0.0011	0.4321	0.012	364.4	25.0	301.9	28.1
Y1-IG062_13	30	1635	97	17	0.0583	0.0011	0.4340	0.011	365.3	24.3	357.8	7.4
Y1-IG062_21	30	122	31	3.9	0.0584	0.0031	0.4308	0.067	365.6	69.1	130.6	10.5
Y1-IG062_7	30	1382	67	21	0.0589	0.0011	0.4390	0.009	369.1	23.9	370.9	12.2
Y1-IG062_9	30	113	52	2.2	0.0590	0.0034	0.4434	0.059	369.5	76.4	365.6	18.9
Y1-IG062_17	30	1219	54	23	0.0592	0.0020	0.4398	0.017	370.9	45.4	363.3	8.5
Y1-IG062_12	30	1395	63	22	0.0593	0.0019	0.4426	0.017	371.1	42.4	299.5	13.9
Y1-IG062_6	30	240	51	4.7	0.0617	0.0038	0.4628	0.039	386.1	89.4	364.4	6.9

*0.9=Systematic error of 206Pb/238U age based on Sri Lankan standard

Table C14: LA-ICP-MS U–Pb zircon data from sample Y1-AW038

					Radiogenic Ratios						**Age (Ma)**	
	Spot Size (µm)	**U (ppm)**	**Th (ppm)**	**U/Th**	**206Pb/238U**	**2σ**	**207Pb/235U**	**2σ**	**206/207 Pb**	**2σ**	**206Pb/238U**	**2σ**
Y1-AW038												
Y1-AW038_14	10	1386	29	48	0.0163	0.0005	0.1085	0.004	104.4	3.4	104.4	3.2
Y1-AW038_6	10	933	27	34	0.0174	0.0009	0.1169	0.006	111.1	6.3	111.1	5.6
Y1-AW038_2	10	1014	28	36	0.0158	0.0009	0.1051	0.006	100.8	6.0	100.8	5.9
Y1-AW038_8	10	923	24	39	0.0164	0.0009	0.1090	0.006	104.8	6.3	104.8	6.0
Y1-AW038_24	10	1091	29	38	0.0181	0.0010	0.1211	0.007	115.5	7.0	115.5	6.1
Y1-AW038_21	10	526	23	23	0.0161	0.0010	0.1083	0.007	102.7	6.6	102.7	6.4
Y1-AW038_26	10	1342	31	43	0.0174	0.0011	0.1165	0.007	111.0	7.5	111.0	6.8
Y1-AW038_22	10	1340	23	59	0.0185	0.0011	0.1234	0.008	117.9	7.9	117.9	6.7
Y1-AW038_23	10	929	23	40	0.0176	0.0011	0.1176	0.007	112.2	7.8	112.2	6.9
Y1-AW038_13	10	1013	23	45	0.0180	0.0011	0.1200	0.008	114.7	7.9	114.7	6.9
Y1-AW038_17	10	1259	30	42	0.0180	0.0012	0.1206	0.008	114.7	8.8	114.7	7.7
Y1-AW038_9	10	662	15	44	0.0171	0.0015	0.1145	0.010	109.2	10.2	109.2	9.3
Y1-AW038_1	10	587	28	21	0.0156	0.0022	0.1061	0.015	99.8	14.2	99.8	14.2
Y1-AW038_25	10	987	28	36	0.0165	0.0007	0.1219	0.036	105.3	4.7	105.3	4.5
Y1-AW038_12	10	635	27	24	0.0168	0.0006	0.1247	0.038	107.6	4.2	107.6	3.9
Y1-AW038_18	10	1117	39	28	0.0158	0.0022	0.1450	0.134	100.9	13.9	100.9	13.8

*1.3=Systematic error of ^{206}Pb/^{238}U age based on Sri Lankan standard

Table C15: LA-ICP-MS U–Pb zircon data from sample Y1-IG070

					Radiogenic Ratios						Age (Ma)	
	Spot Size (μm)	**U (ppm)**	**Th (ppm)**	**U/Th**	**206Pb/238U**	**2σ**	**207Pb/235U**	**2σ**	**206/207 Pb**	**2σ**	**206Pb/238U**	**2σ**
Y1-IG070												
Y1-IG070_25	30	711	8	91	0.0160	0.0006	0.1052	0.010	102.4	3.7	108.0	4.0
Y1-IG070_2	30	1868	81	23	0.0164	0.0005	0.1099	0.004	104.9	3.5	104.9	3.4
Y1-IG070_22	30	483	17	28	0.0165	0.0008	0.1054	0.011	105.5	5.6	107.0	3.3
Y1-IG070_7	30	795	17	48	0.0165	0.0004	0.1154	0.011	105.8	2.9	108.3	2.3
Y1-IG070_24	30	1091	38	29	0.0166	0.0005	0.1111	0.007	105.9	3.6	111.5	3.5
Y1-IG070_8	30	1089	44	25	0.0166	0.0007	0.1085	0.010	106.0	4.9	105.8	2.7
Y1-IG070_16	30	553	16	34	0.0166	0.0006	0.1079	0.009	106.1	4.2	106.0	4.6
Y1-IG070_9	30	440	17	26	0.0166	0.0004	0.1131	0.016	106.2	2.6	106.2	2.4
Y1-IG070_18	30	1119	45	25	0.0167	0.0005	0.1105	0.006	106.5	3.5	108.8	3.1
Y1-IG070_15	30	849	22	39	0.0167	0.0005	0.1099	0.009	106.5	3.3	106.5	3.1
Y1-IG070_21	30	1900	83	23	0.0167	0.0005	0.1130	0.006	106.7	3.5	106.1	3.9
Y1-IG070_3	30	976	37	27	0.0167	0.0005	0.1120	0.006	107.0	3.5	106.5	3.3
Y1-IG070_1	30	1306	40	33	0.0169	0.0006	0.1131	0.007	108.0	4.3	108.1	4.1
Y1-IG070_20	30	684	25	27	0.0169	0.0007	0.1115	0.009	108.1	4.5	106.7	3.3
Y1-IG070_5	30	1425	23	62	0.0169	0.0004	0.1190	0.009	108.3	2.4	105.5	5.3
Y1-IG070_23	30	1167	33	35	0.0169	0.0008	0.1136	0.008	108.3	5.6	108.3	5.2
Y1-IG070_11	30	1232	41	30	0.0170	0.0005	0.1157	0.005	108.8	3.4	105.9	3.4
Y1-IG070_6	30	1224	16	76	0.0174	0.0006	0.1159	0.006	111.5	3.9	102.4	3.6

*0.9=Systematic error of 206Pb/238U age based on Sri Lankan standard

Table C16: LA-ICP-MS U–Pb zircon data from sample Y1-AE033

					Radiogenic Ratios						Age (Ma)	
	Spot Size (µm)	**U (ppm)**	**Th (ppm)**	**U/Th**	**206Pb/238U**	**2σ**	**207Pb/235U**	**2σ**	**206/207 Pb**	**2σ**	**206Pb/238U**	**2σ**
Y1-AE033												
Y1-AEO33-5R	10	2050	16	129	0.0157	0.0007	0.1048	0.005	20.7	0.6	100.5	4.3
Y1-AEO33-10R	10	1922	14	136	0.0159	0.0003	0.1059	0.004	20.7	0.7	101.7	1.8
Y1-AEO33-11C	10	832	8	100	0.0159	0.0014	0.1065	0.010	20.6	0.4	101.8	8.9
Y1-AEO33-12R	10	1869	12	154	0.0160	0.0005	0.1063	0.004	20.7	0.5	102.2	3.4
Y1-AEO33-3C	10	1423	10	142	0.0160	0.0006	0.1054	0.005	20.9	0.5	102.3	4.0
Y1-AEO33-15R	10	2121	11	189	0.0160	0.0005	0.1068	0.005	20.7	0.6	102.3	2.9
Y1-AEO33-2R	10	1865	11	166	0.0161	0.0008	0.1066	0.006	20.8	0.5	102.8	4.8
Y1-AEO33-13R	10	1940	11	180	0.0162	0.0005	0.1087	0.005	20.5	0.6	103.5	3.2
Y1-AEO33-3R	10	1803	14	127	0.0162	0.0006	0.1076	0.004	20.7	0.5	103.6	3.5
Y1-AEO33-16R	10	2128	10	204	0.0162	0.0006	0.1071	0.006	20.9	0.8	103.7	3.6
Y1-AEO33-8R	10	810	27	30	0.0162	0.0003	0.1068	0.003	20.9	0.4	103.8	2.0
Y1-AEO33-22R	10	515	10	53	0.0168	0.0006	0.1139	0.006	20.3	0.7	107.3	3.6
Y1-AEO33-7C	10	550	12	44	0.0171	0.0002	0.1134	0.002	20.7	0.4	109.1	1.1
Y1-AEO33-4R	10	572	5	126	0.0172	0.0009	0.1252	0.019	18.9	2.8	110.0	5.5
Y1-AEO33-18R	10	851	6	148	0.0173	0.0012	0.1468	0.080	16.3	8.8	110.8	7.7
Y1-AEO33-19R	10	640	7	90	0.0174	0.0005	0.1746	0.009	13.7	0.6	111.1	3.3
Y1-AEO33-21R	10	710	5	134	0.0176	0.0006	0.1187	0.007	20.4	1.0	112.2	4.0
Y1-AEO33-14R	10	857	14	61	0.0179	0.0019	0.1488	0.043	16.6	4.5	114.3	12.2
Y1-AEO33-17R	10	1463	39	38	0.0185	0.0008	0.2745	0.048	9.3	1.6	118.1	5.3

*0.9=Systematic error of 206Pb/238U age based on Sri Lankan standard

Table C17: LA-ICP-MS U–Pb zircon data from sample 10CY-039

					Radiogenic Ratios						**Age (Ma)**	
	Spot Size (µm)	**U (ppm)**	**Th (ppm)**	**U/Th**	**206Pb/238U**	**2σ**	**207Pb/235U**	**2σ**	**206/207 Pb**	**2σ**	**206Pb/238U**	**2σ**
10CY-039												
10CY039_120	10	1028	14	71	0.0160	0.0004	0.1066	0.003	102.0	2.5	106.2	4.9
10CY039_18	10	575	12	49	0.0163	0.0007	0.1084	0.005	104.2	4.8	104.4	3.4
10CY039_2	10	568	25	23	0.0163	0.0005	0.1091	0.004	104.4	3.5	106.3	7.1
10CY039_8	10	500	7.4	67	0.0164	0.0007	0.1100	0.005	105.0	4.5	108.7	11.5
10CY039_15	10	1500	11	135	0.0165	0.0008	0.1095	0.006	105.2	5.4	106.5	9.1
10CY039_13	10	582	16	36	0.0165	0.0009	0.1109	0.006	105.8	5.9	107.5	4.2
10CY039_25	10	521	10	54	0.0166	0.0008	0.1124	0.006	106.1	5.2	106.5	4.9
10CY039_1	10	541	8.9	61	0.0166	0.0008	0.1105	0.006	106.2	5.2	105.0	4.3
10CY039_3	10	397	7.6	52	0.0166	0.0011	0.1121	0.008	106.3	7.5	106.7	7.7
10CY039_5	10	724	16	44	0.0167	0.0014	0.1112	0.010	106.5	9.6	110.0	5.5
10CY039_7	10	748	11	69	0.0167	0.0008	0.1111	0.006	106.5	5.2	107.9	4.0
10CY039_9	10	611	15	41	0.0167	0.0012	0.1118	0.008	106.7	8.2	114.5	4.4
10CY039_6	10	671	14	47	0.0168	0.0007	0.1125	0.005	107.5	4.5	105.8	5.6
10CY039_11	10	727	17	42	0.0169	0.0006	0.1126	0.005	107.9	4.3	110.5	5.8
10CY039_4	10	498	14	37	0.0170	0.0018	0.1133	0.012	108.7	12.5	105.2	5.1
10CY039_19	10	510	19	26	0.0170	0.0008	0.1177	0.009	109.0	5.5	104.2	4.6
10CY039_23	10	482	20	24	0.0172	0.0010	0.1153	0.007	110.0	6.9	109.0	5.0
10CY039_10	10	446	6	77	0.0172	0.0009	0.1151	0.006	110.0	6.1	102.0	2.5
10CY039_14	10	651	14	45	0.0173	0.0009	0.1641	0.025	110.5	6.4	110.8	6.6
10CY039_24	10	458	9	53	0.0173	0.0010	0.1156	0.007	110.7	7.2	110.0	6.3
10CY039_22	10	554	10	55	0.0173	0.0010	0.1161	0.007	110.8	7.4	110.7	6.5
10CY039_12	10	586	10	61	0.0179	0.0007	0.1196	0.005	114.5	5.1	106.1	4.9

*2.2= Systematic error of 206Pb/238U age based on Sri Lankan standard

Table C18: LA-ICP-MS U–Pb zircon data from sample Y1-AE051

					Radiogenic Ratios						Age (Ma)	
	Spot Size (µm)	**U (ppm)**	**Th (ppm)**	**U/Th**	**206Pb/238U**	**2σ**	**207Pb/235U**	**2σ**	**206/207 Pb**	**2σ**	**206Pb/238U**	**2σ**
Y1-AE051												
Y1AE051_14	10	703	25	28	0.0149	0.0006	0.0998	0.004	95.6	3.5	106.4	1.6
Y1AE051_1	10	946	52	18	0.0155	0.0006	0.1182	0.006	99.3	3.5	95.6	3.7
Y1AE051_12	10	913	57	16	0.0156	0.0007	0.1037	0.005	100.0	4.7	110.7	4.0
Y1AE051_18	10	718	23	31	0.0157	0.0009	0.1052	0.006	100.4	5.5	108.6	4.4
Y1AE051_8	10	375	7	51	0.0157	0.0009	0.1205	0.058	100.6	5.7	100.0	4.7
Y1AE051_13	10	961	56	17	0.0159	0.0009	0.1062	0.006	101.5	5.9	101.8	4.6
Y1AE051_16	10	1113	43	26	0.0159	0.0007	0.1066	0.005	101.8	4.7	101.9	5.1
Y1AE051_10	10	612	17	35	0.0159	0.0008	0.1082	0.006	101.9	5.2	110.3	5.2
Y1AE051_25	10	583	25	23	0.0160	0.0013	0.1094	0.010	102.1	8.4	100.4	5.5
Y1AE051_4	10	843	50	17	0.0162	0.0008	0.1117	0.008	103.7	5.6	108.4	5.4
Y1AE051_11	10	548	17	32	0.0163	0.0011	0.1081	0.008	104.4	7.2	104.8	5.0
Y1AE051_5	10	983	51	19	0.0164	0.0008	0.1091	0.006	104.8	5.2	99.3	3.6
Y1AE051_21	10	424	12	36	0.0164	0.0009	0.1086	0.007	104.9	6.2	101.5	5.8
Y1AE051_24	10	755	34	22	0.0166	0.0003	0.1115	0.003	106.4	1.7	104.9	6.0
Y1AE051_19	10	604	5	131	0.0169	0.0022	0.1132	0.015	107.7	14.7	103.7	5.4
Y1AE051_3	10	1170	68	17	0.0170	0.0009	0.1140	0.006	108.4	5.9	104.4	6.9
Y1AE051_22	10	557	10	58	0.0170	0.0007	0.1129	0.005	108.6	4.8	102.1	8.2
Y1AE051_7	10	746	37	20	0.0171	0.0010	0.1290	0.037	109.1	6.6	112.7	12.3
Y1AE051_23	10	691	30	23	0.0172	0.0007	0.1210	0.019	109.9	5.2	107.7	13.6
Y1AE051_15	10	1102	7	168	0.0173	0.0011	0.1221	0.020	110.3	7.7	109.9	4.7
Y1AE051_20	10	563	18	32	0.0173	0.0008	0.1146	0.006	110.3	5.8	110.3	7.0
Y1AE051_2	10	1033	44	23	0.0173	0.0006	0.1157	0.004	110.7	4.4	109.1	6.1
Y1AE051_17	10	1150	9	125	0.0176	0.0019	0.1181	0.013	112.7	13.9	100.6	5.7

*1.2=Systematic error of ^{206}Pb/^{238}U age based on Sri Lankan standard

Table C19: LA-ICP-MS U–Pb zircon data from sample Y1-AE064

					Radiogenic Ratios						Age (Ma)	
	Spot Size (µm)	**U (ppm)**	**Th (ppm)**	**U/Th**	**206Pb/238U**	**2σ**	**207Pb/235U**	**2σ**	**206/207 Pb**	**2σ**	**206Pb/238U**	**2σ**
Y1-AE064												
Y1-AE064_25	10	649	19	35	0.0147	0.0007	0.0983	0.005	94.3	4.3	94.3	4.6
Y1-AE064_22	10	548	24	23	0.0151	0.0017	0.1017	0.012	96.9	10.5	96.9	10.9
Y1-AE064_3	10	717	28	26	0.0157	0.0006	0.1054	0.005	100.4	4.1	100.4	4.1
Y1-AE064_13	10	976	30	32	0.0157	0.0011	0.1041	0.007	100.6	6.9	100.6	6.8
Y1-AE064_7	10	441	21	21	0.0158	0.0006	0.1048	0.005	100.8	4.1	100.8	4.0
Y1-AE064_2	10	680	25	27	0.0159	0.0008	0.1056	0.005	101.9	4.9	101.9	4.8
Y1-AE064_1	10	692	26	26	0.0160	0.0008	0.1056	0.006	102.0	5.4	102.0	5.3
Y1-AE064_14	10	599	31	19	0.0161	0.0009	0.1072	0.006	103.2	5.9	103.2	5.7
Y1-AE064_4	10	354	25	14	0.0161	0.0006	0.1078	0.006	103.2	3.8	103.2	3.7
Y1-AE064_16	10	411	18	23	0.0162	0.0012	0.1085	0.009	103.7	8.0	103.7	7.8
Y1-AE064_19	10	497	22	23	0.0162	0.0010	0.1070	0.007	103.7	6.9	103.7	6.6
Y1-AE064_24	10	680	33	20	0.0163	0.0007	0.1122	0.009	104.2	4.4	104.2	4.3
Y1-AE064_6	10	814	33	25	0.0163	0.0008	0.1089	0.006	104.5	5.4	104.5	5.2
Y1-AE064_18	10	423	35	12	0.0164	0.0010	0.1221	0.008	105.1	6.7	105.1	6.3
Y1-AE064_21	10	601	32	19	0.0165	0.0008	0.1102	0.006	105.2	5.4	105.2	5.2
Y1-AE064_15	10	803	33	25	0.0165	0.0006	0.1100	0.004	105.6	4.1	105.6	3.9
Y1-AE064_8	10	610	12	52	0.0165	0.0008	0.1108	0.006	105.6	5.5	105.6	5.2
Y1-AE064_10	10	428	32	13	0.0165	0.0009	0.1124	0.013	105.7	6.3	105.7	6.0
Y1-AE064_5	10	449	28	16	0.0165	0.0004	0.1101	0.004	105.8	3.0	105.8	2.8
Y1-AE064_12	10	359	23	16	0.0168	0.0009	0.1117	0.007	107.2	6.3	107.2	5.9
Y1-AE064_23	10	942	16	58	0.0177	0.0020	0.1467	0.096	113.3	14.6	113.3	12.9
Y1-AE064_9	10	625	34	18	0.0164	0.0023	0.1518	0.100	104.9	15.2	104.9	14.5
Y1-AE064_20	10	900	12	78	0.0191	0.0007	0.1287	0.005	122.1	5.2	122.1	4.2
Y1-AE064_17	10	1338	30	45	0.0453	0.0018	0.4035	0.285	285.9	32.6	285.9	11.4

*0.7=Systematic error of ^{206}Pb/^{238}U age based on Sri Lankan standard

Table C20: LA-ICP-MS U–Pb zircon data from sample Y1-IG062

					Radiogenic Ratios						Age (Ma)	
	Spot Size (µm)	**U (ppm)**	**Th (ppm)**	**U/Th**	**206Pb/238U**	**2σ**	**207Pb/235U**	**2σ**	**206/207 Pb**	**2σ**	**206Pb/238U**	**2σ**
Y1-IG052												
Y1-IG052_24	10	495.585	19.86456	24.948	0.0149	0.0009	0.0986	0.006	95.5	5.2	95.5	5.4
Y1-IG052_13	10	488.597	16.55435	29.515	0.0153	0.0007	0.1031	0.006	97.8	4.3	97.8	4.4
Y1-IG052_20	10	298.438	9.073079	32.893	0.0155	0.0007	0.1032	0.005	99.1	4.6	99.1	4.7
Y1-IG052_23	10	448.381	21.70993	20.653	0.0156	0.0011	0.1134	0.029	100.0	7.3	100.0	7.3
Y1-IG052_9	10	432.231	16.44661	26.281	0.0158	0.0011	0.1057	0.007	101.2	6.8	101.2	6.7
Y1-IG052_16	10	409.409	23.18697	17.657	0.0158	0.0005	0.1054	0.004	101.3	3.4	101.3	3.4
Y1-IG052_4	10	387.278	16.96091	22.834	0.0159	0.0006	0.1077	0.004	101.6	3.8	101.6	3.7
Y1-IG052_6	10	401.374	19.13053	20.981	0.0159	0.0009	0.1049	0.006	101.6	5.8	101.6	5.7
Y1-IG052_10	10	402.287	16.70144	24.087	0.0161	0.0010	0.1065	0.007	102.9	6.5	102.9	6.3
Y1-IG052_7	10	613.899	10.74514	57.133	0.0162	0.0006	0.1146	0.006	103.7	4.0	103.7	3.9
Y1-IG052_5	10	434.494	19.09688	22.752	0.0163	0.0007	0.1093	0.006	104.0	4.7	104.0	4.5
Y1-IG052_18	10	359.288	16.72064	21.488	0.0164	0.0011	0.1093	0.008	104.8	7.2	104.8	6.9
Y1-IG052_19	10	537.838	10.92955	49.21	0.0167	0.0005	0.1105	0.005	106.5	3.6	106.5	3.4
Y1-IG052_11	10	240.487	7.289655	32.99	0.0167	0.0010	0.1135	0.007	106.6	6.5	106.6	6.1
Y1-IG052_1	10	594.762	12.68342	46.893	0.0181	0.0006	0.1210	0.004	115.9	4.4	115.9	3.8
Y1-IG052_2	10	965.646	6.397825	150.93	0.0224	0.0044	0.1555	0.030	143.0	39.3	143.0	27.5
Y1-IG052_21	10	327.6	117.994	2.7764	0.0865	0.0046	0.7025	0.039	534.9	146.5	534.9	27.4

*1.1=Systematic error of 206Pb/238U age based on Sri Lankan standard

Table C21: LA-ICP-MS U–Pb zircon data from sample 10CY-024

					Radiogenic Ratios						Age (Ma)	
	Spot Size (µm)	**U (ppm)**	**Th (ppm)**	**U/Th**	**206Pb/238U**	**2σ**	**207Pb/235U**	**2σ**	**206/207 Pb**	**2σ**	**206Pb/238U**	**2σ**
10CY024												
10CY024_4	30	416	517	0.81	0.0143	0.0010	0.1032	0.035	19.3	5.1	101.9	5.6
10CY024_6	30	321	431	0.75	0.0158	0.0005	0.1020	0.024	21.4	2.9	102.0	3.9
10CY024_1	30	339	415	0.82	0.0159	0.0009	0.1141	0.031	21.3	2.7	105.6	8.1
10CY024_2	30	351	458	0.77	0.0159	0.0006	0.1026	0.014	19.1	6.3	91.3	6.3
10CY024_7	30	510	350	1.46	0.0159	0.0006	0.1171	0.026	21.4	4.3	108.3	4.4
10CY024_17	30	106	159	0.67	0.0160	0.0013	0.1080	0.055	21.3	4.9	100.9	3.4
10CY024_25	30	282	790	0.36	0.0163	0.0010	0.1080	0.021	18.8	4.1	102.0	3.8
10CY024_15	30	157	248	0.63	0.0164	0.0016	0.1273	0.042	20.9	4.6	106.2	4.0
10CY024_3	30	337	496	0.68	0.0165	0.0013	0.1070	0.016	19.0	4.7	106.1	4.7
10CY024_14	30	391	537	0.73	0.0166	0.0009	0.1072	0.020	24.1	18.2	107.2	12.8
10CY024_24	30	155	179	0.87	0.0166	0.0019	0.0947	0.051	19.4	3.1	117.2	21.0
10CY024_9	30	257	371	0.69	0.0166	0.0007	0.1203	0.030	18.4	13.7	108.0	12.5
10CY024_8	30	403	537	0.75	0.0166	0.0006	0.1095	0.025	18.6	5.2	110.7	7.1
10CY024_10	30	137	114	1.20	0.0168	0.0020	0.0957	0.073	21.3	3.9	105.9	5.8
10CY024_18	30	153	369	0.42	0.0168	0.0018	0.0879	0.041	17.8	5.6	104.9	9.9
10CY024_12	30	105	35	2.99	0.0169	0.0020	0.1263	0.095	20.5	3.2	108.1	8.9
10CY024_16	30	238	655	0.36	0.0169	0.0014	0.1138	0.020	20.5	10.3	102.6	8.2
10CY024_5	30	372	823	0.45	0.0169	0.0007	0.1091	0.023	26.3	12.0	107.2	11.2
10CY024_13	30	214	141	1.52	0.0173	0.0011	0.1281	0.037	20.9	8.6	120.4	11.0
10CY024_11	30	437	516	0.85	0.0183	0.0033	0.1307	0.032	24.2	12.6	106.1	11.8
10CY024_22	30	109	167	0.65	0.0189	0.0017	0.1245	0.052	20.8	3.8	104.1	6.2

*1.2=Systematic error of ^{206}Pb/^{238}U age based on Sri Lankan standard

Appendix D: Box and Whisker Plots

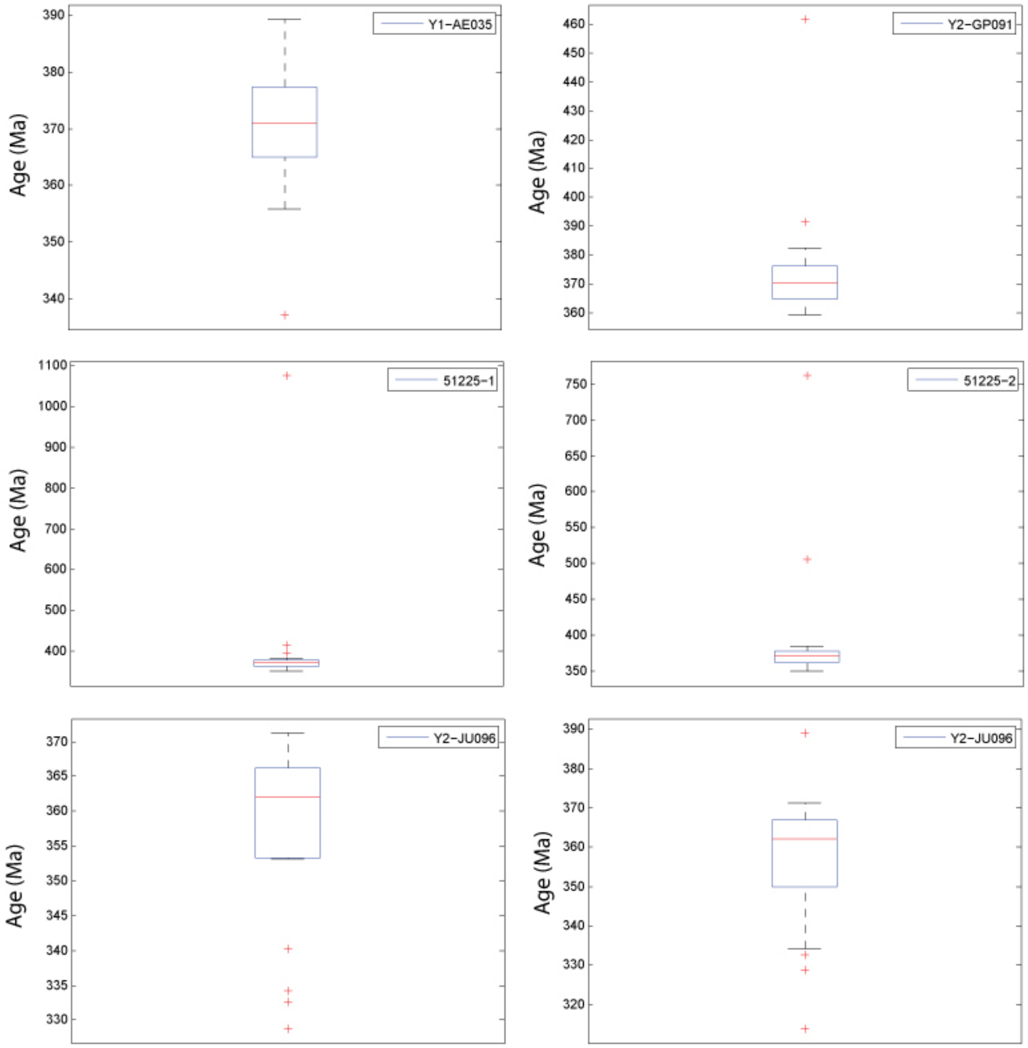

Figure D1: Box and whisker plots of zircon ages

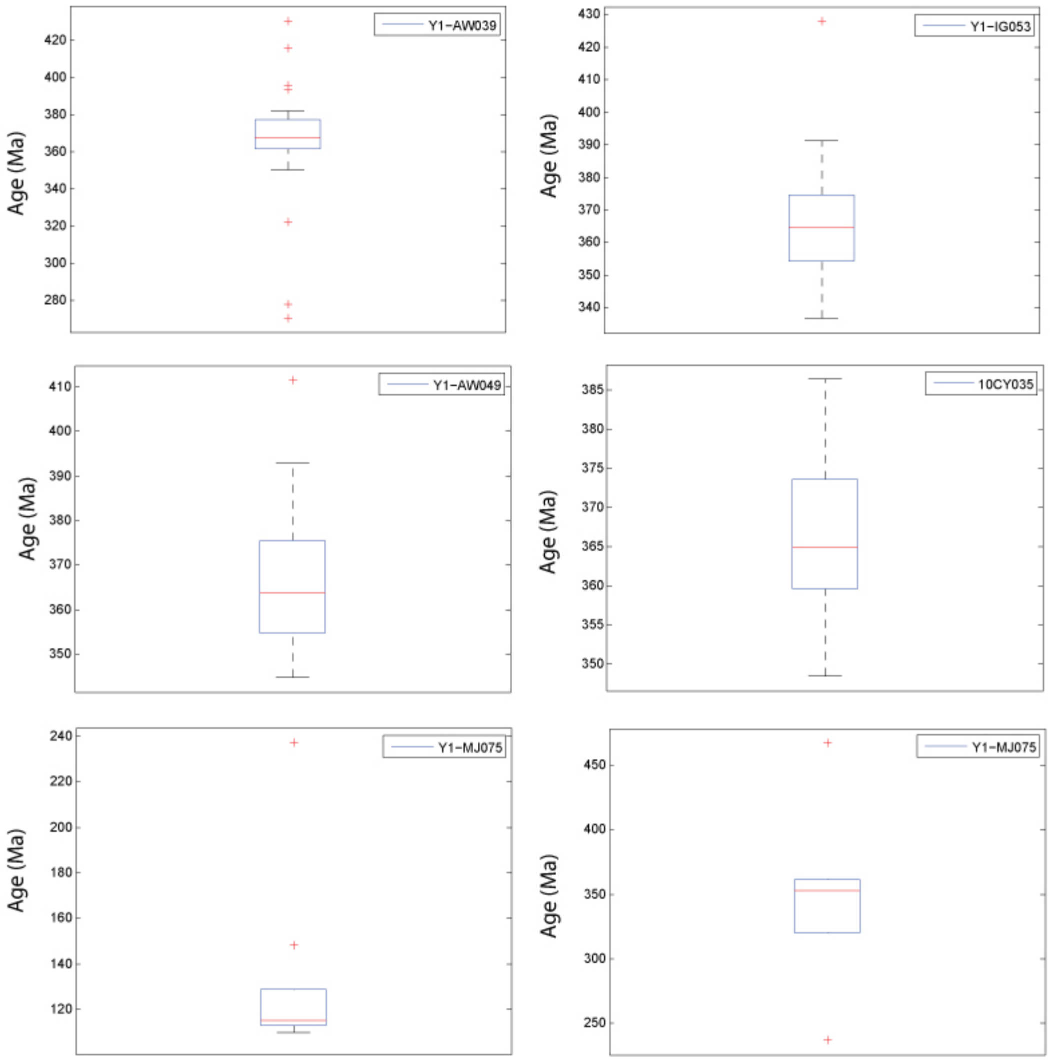

Figure D1: Continued

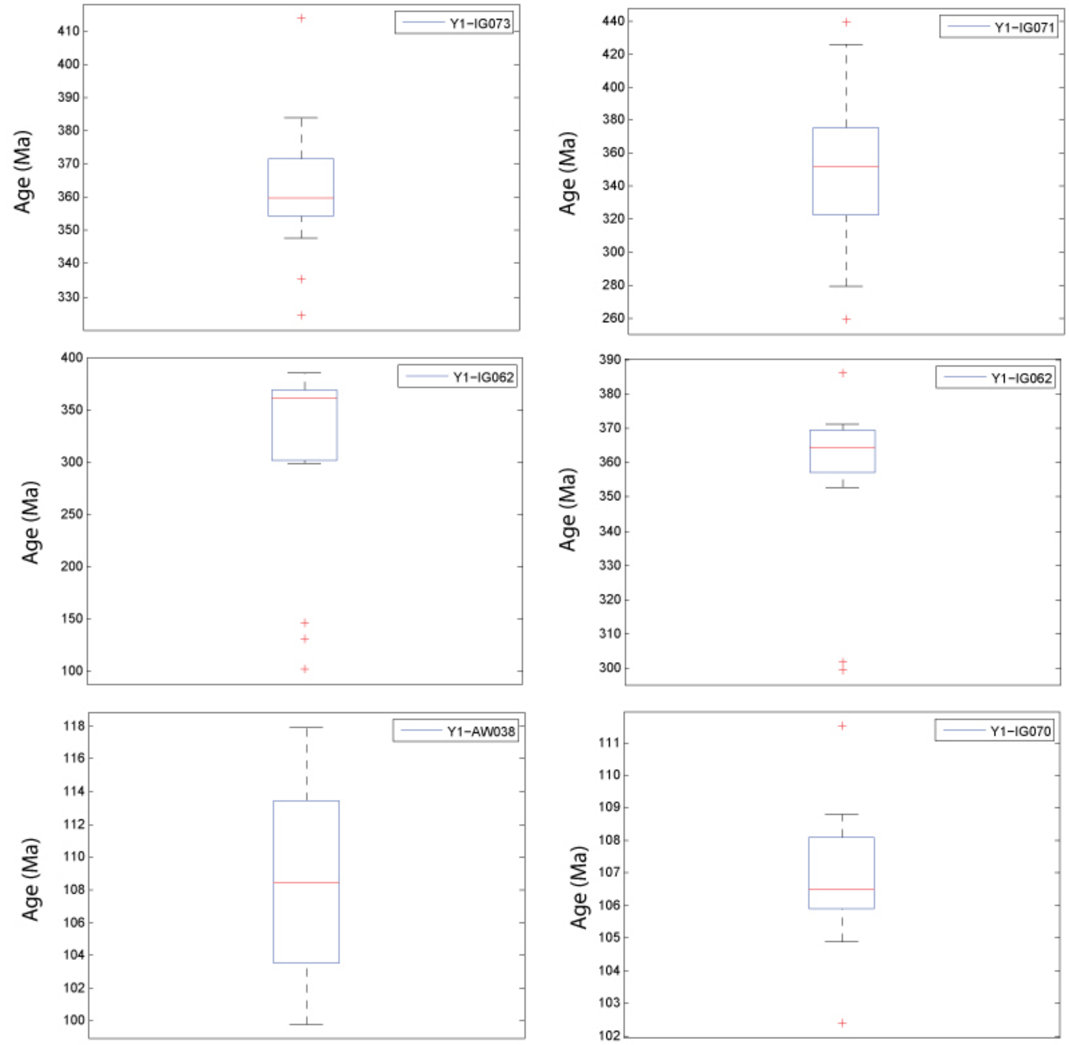

Figure D1: Continued

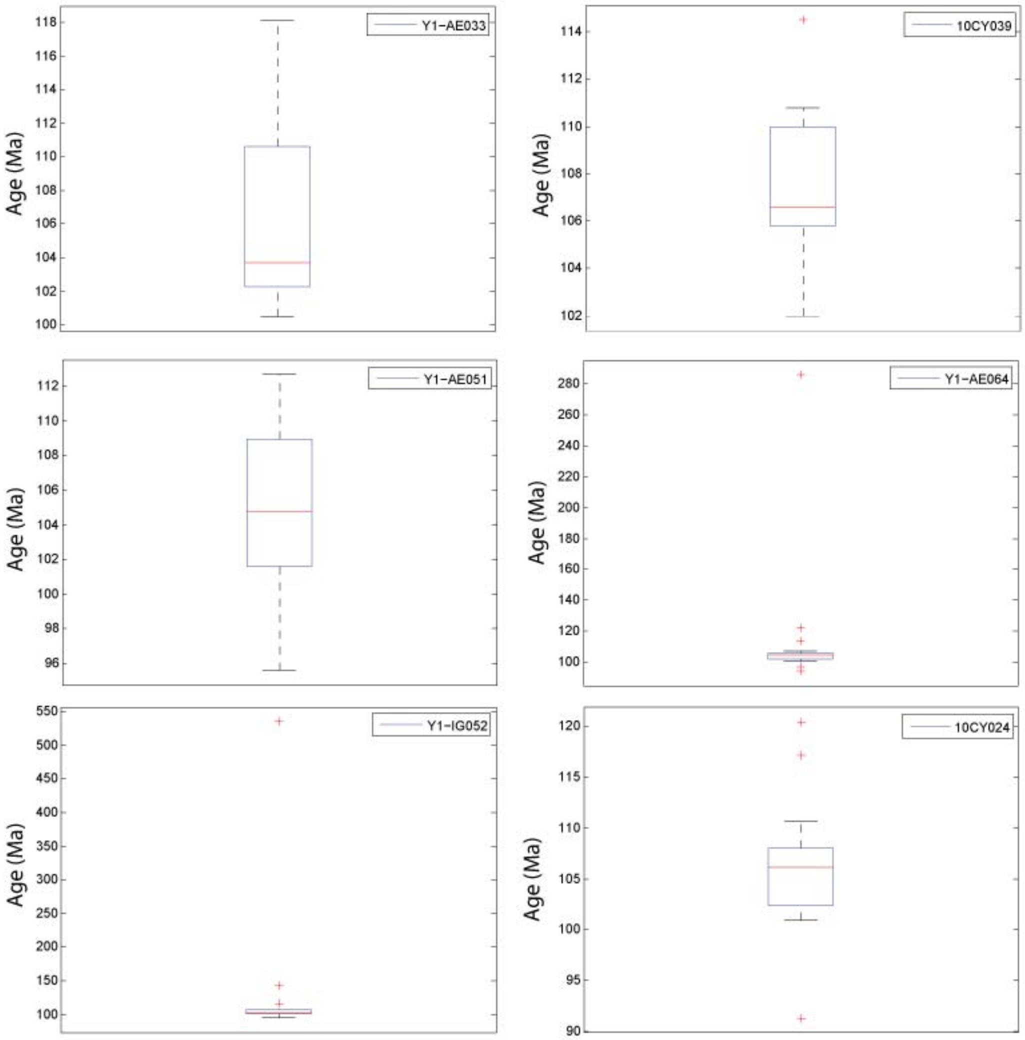

Figure D1: Continued

Appendix E: U–Pb Concordia Plots and Age Histograms

Ford Granodiorite

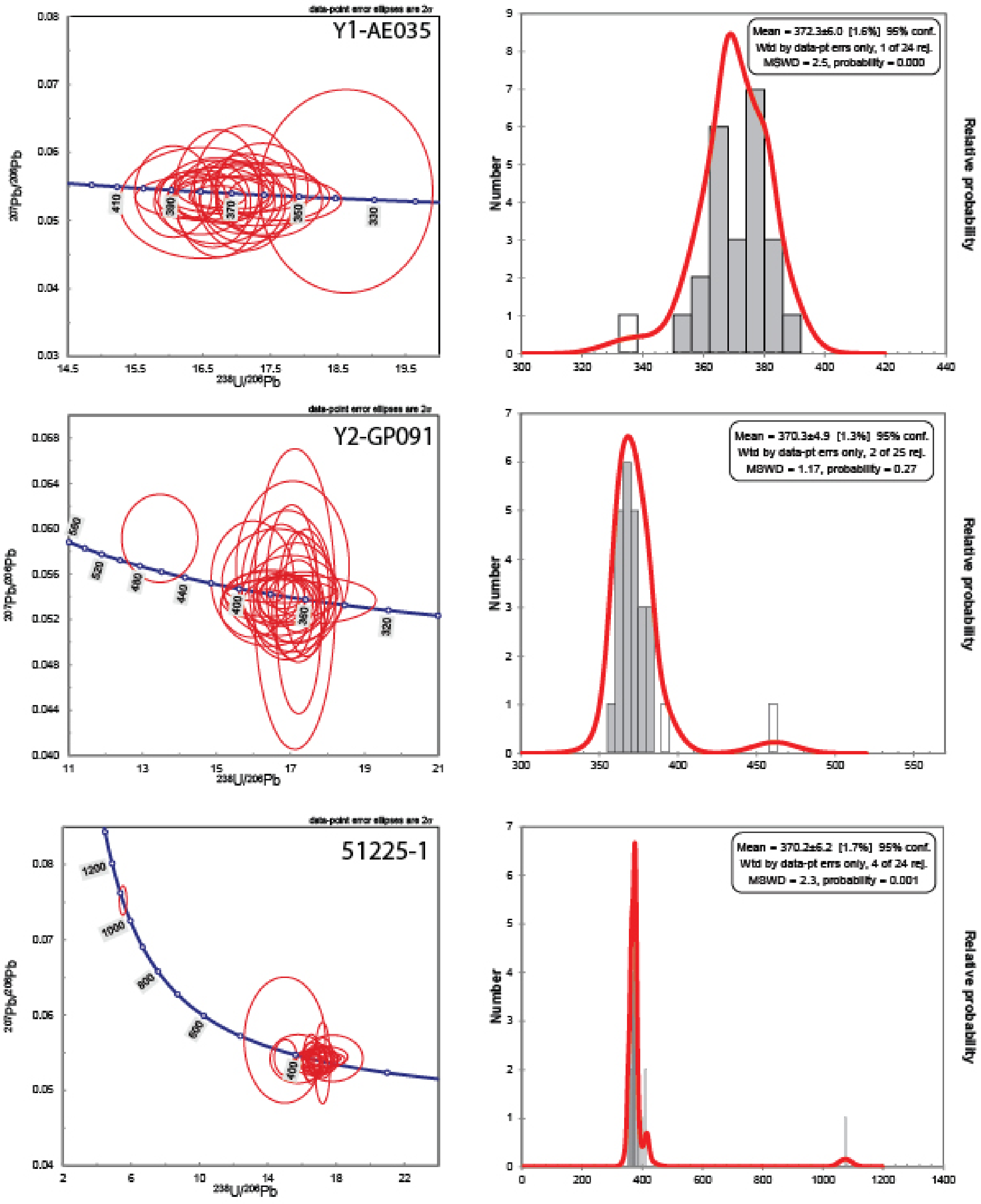

Figure E1: U–Pb Concordia plots and age histograms for Ford Granodiorite samples

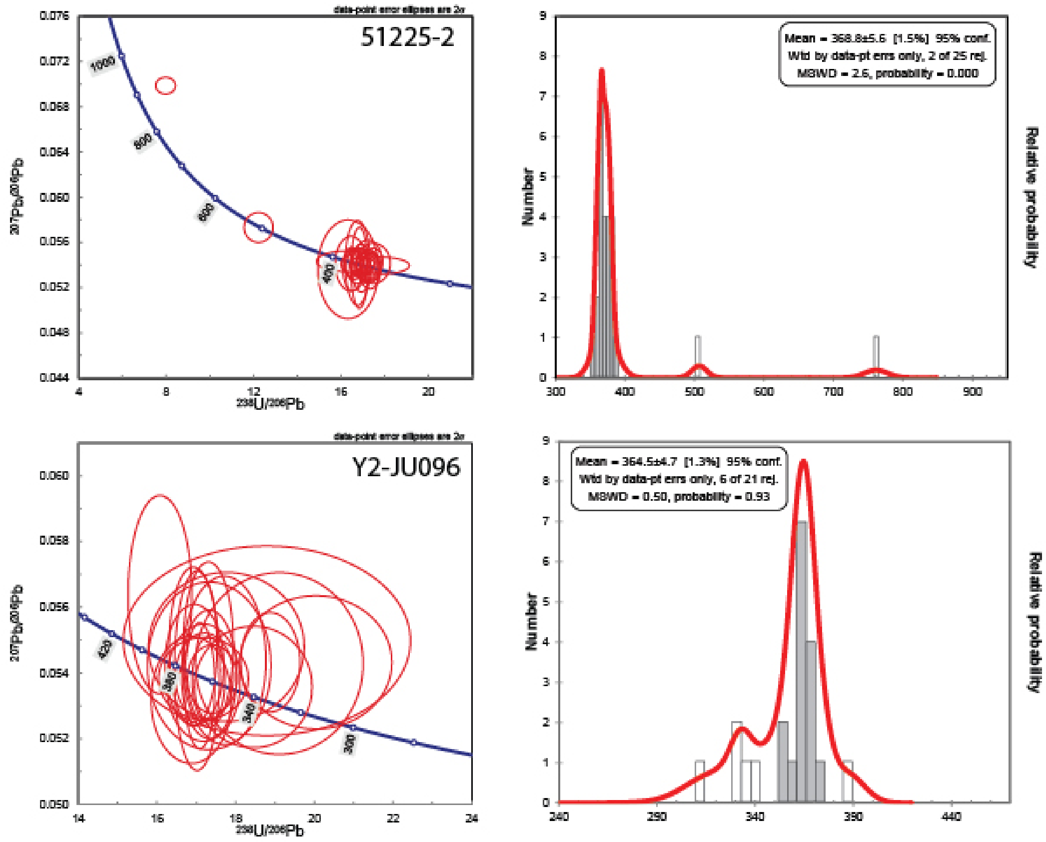

Figure E1: Continued

Devonian Orthogneiss

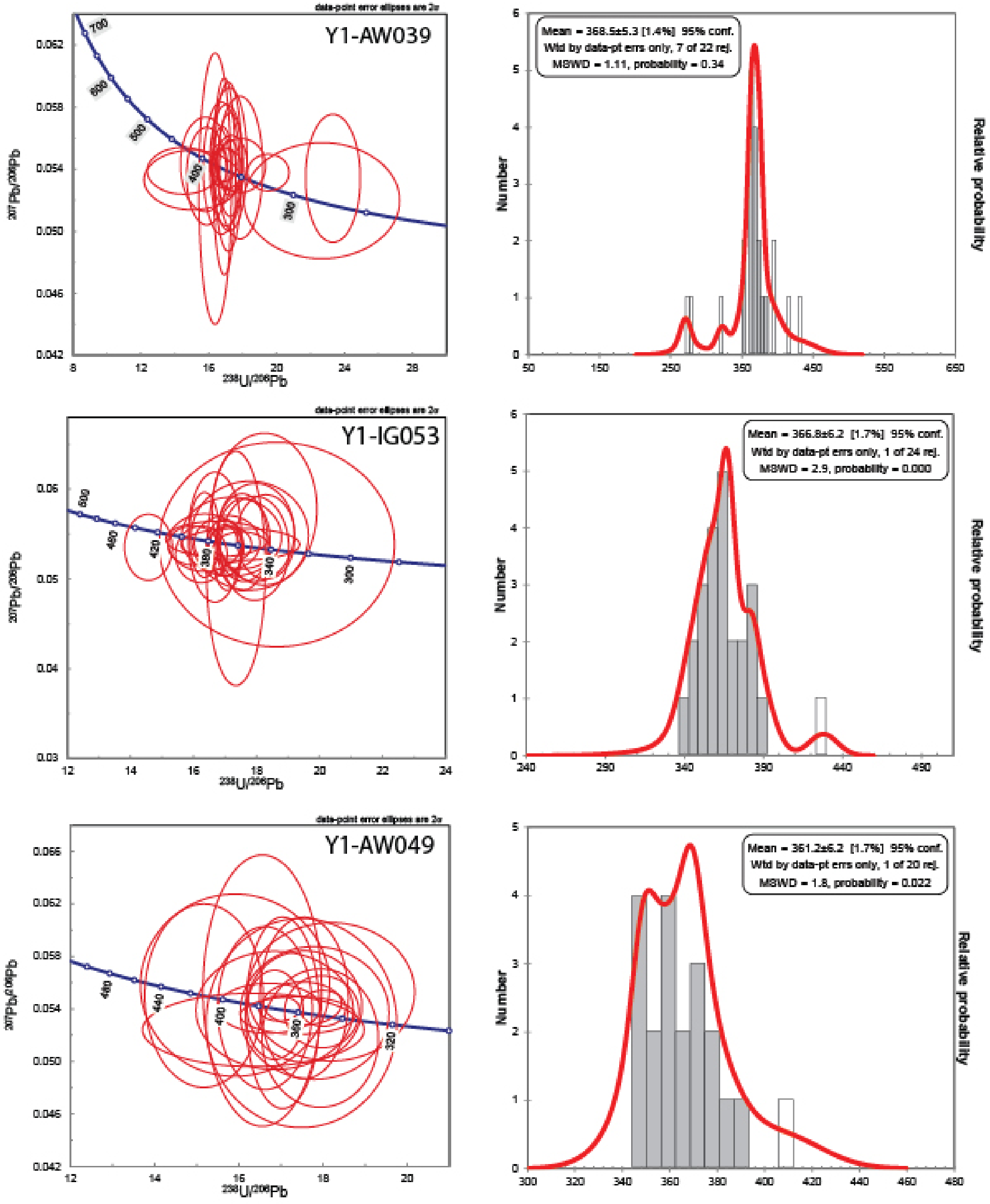

Figure E2: U–Pb Concordia plots and age histograms for Devonian orthogneiss samples

Devonian Orthogneiss

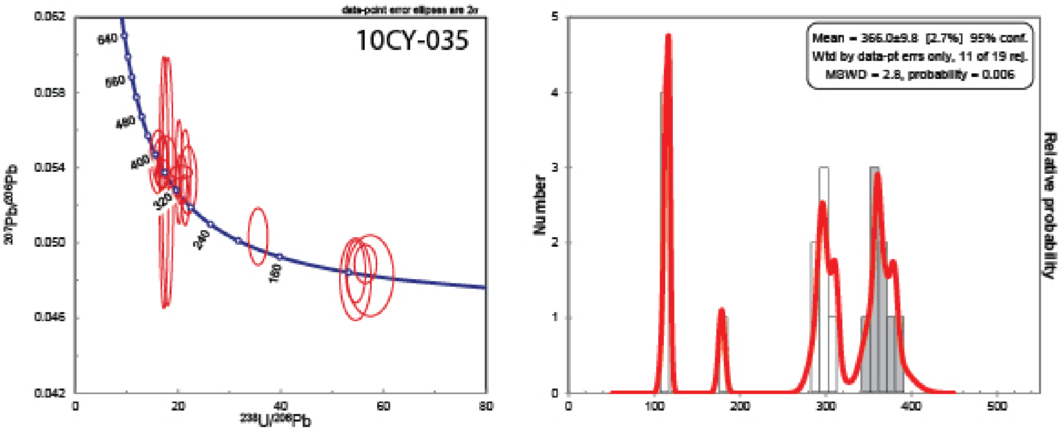

Figure E2: Continued

Cretaceous Orthogneiss

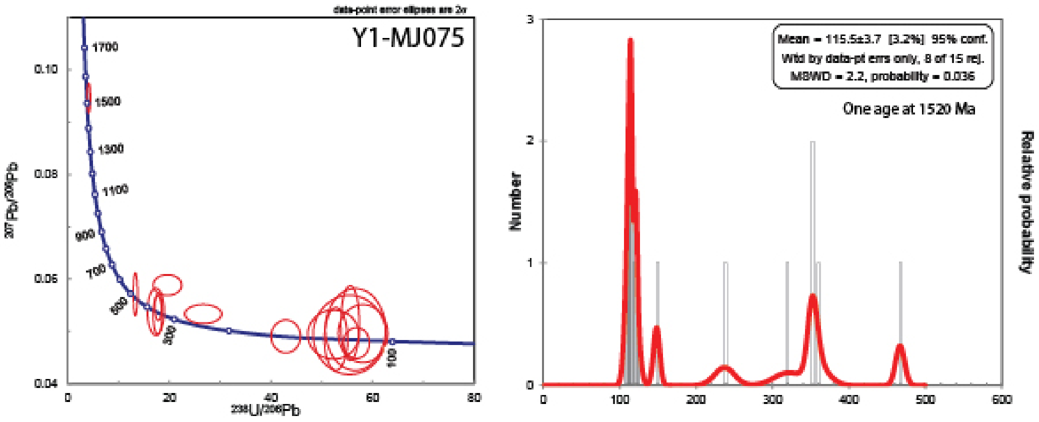

Figure E3: U–Pb Concordia plots and age histograms for Cretaceous orthogneiss sample

Devonian Diatexite

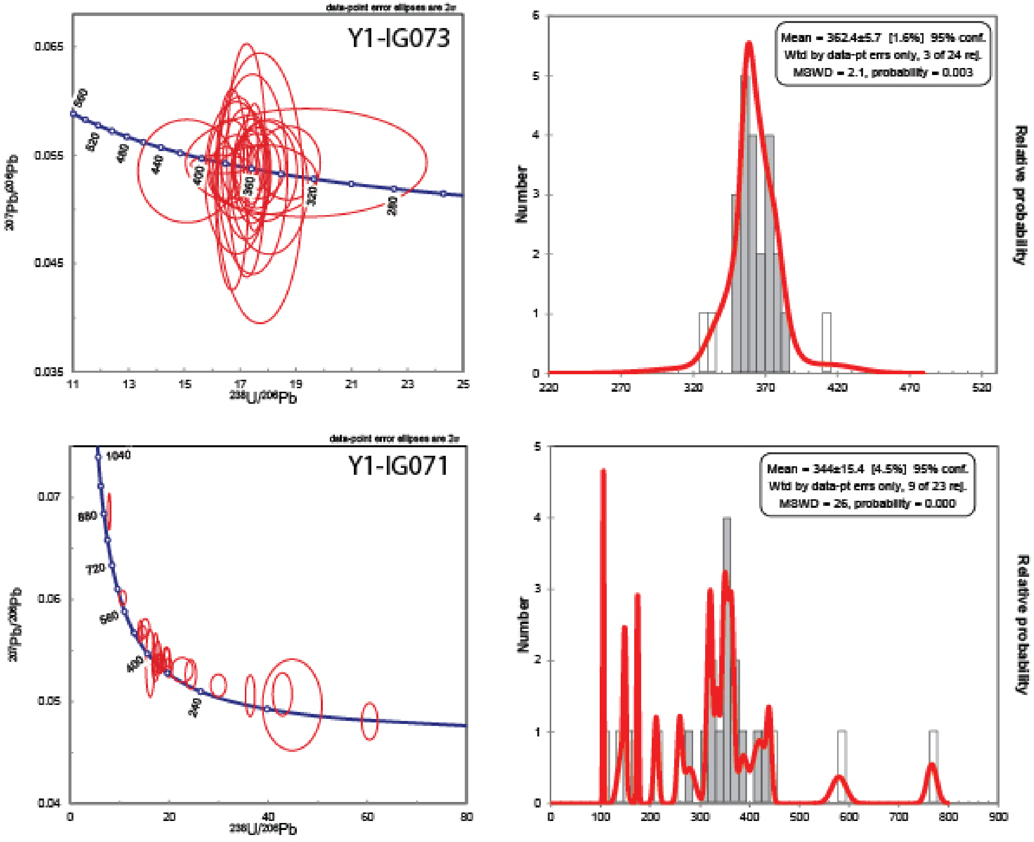

Figure E4: U–Pb Concordia plots and age histograms for Devonian diatexite samples

Devonian Granite

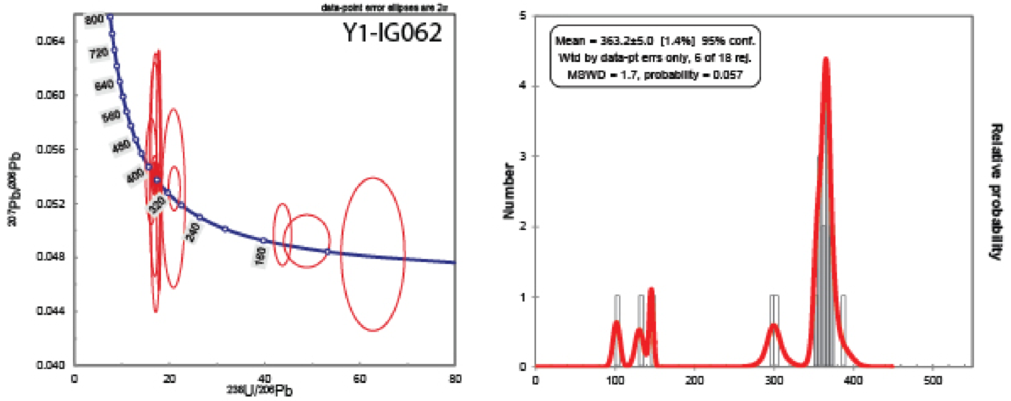

Figure E5: U–Pb Concordia plots and age histograms for Devonian granite sample

Cretaceous Granite

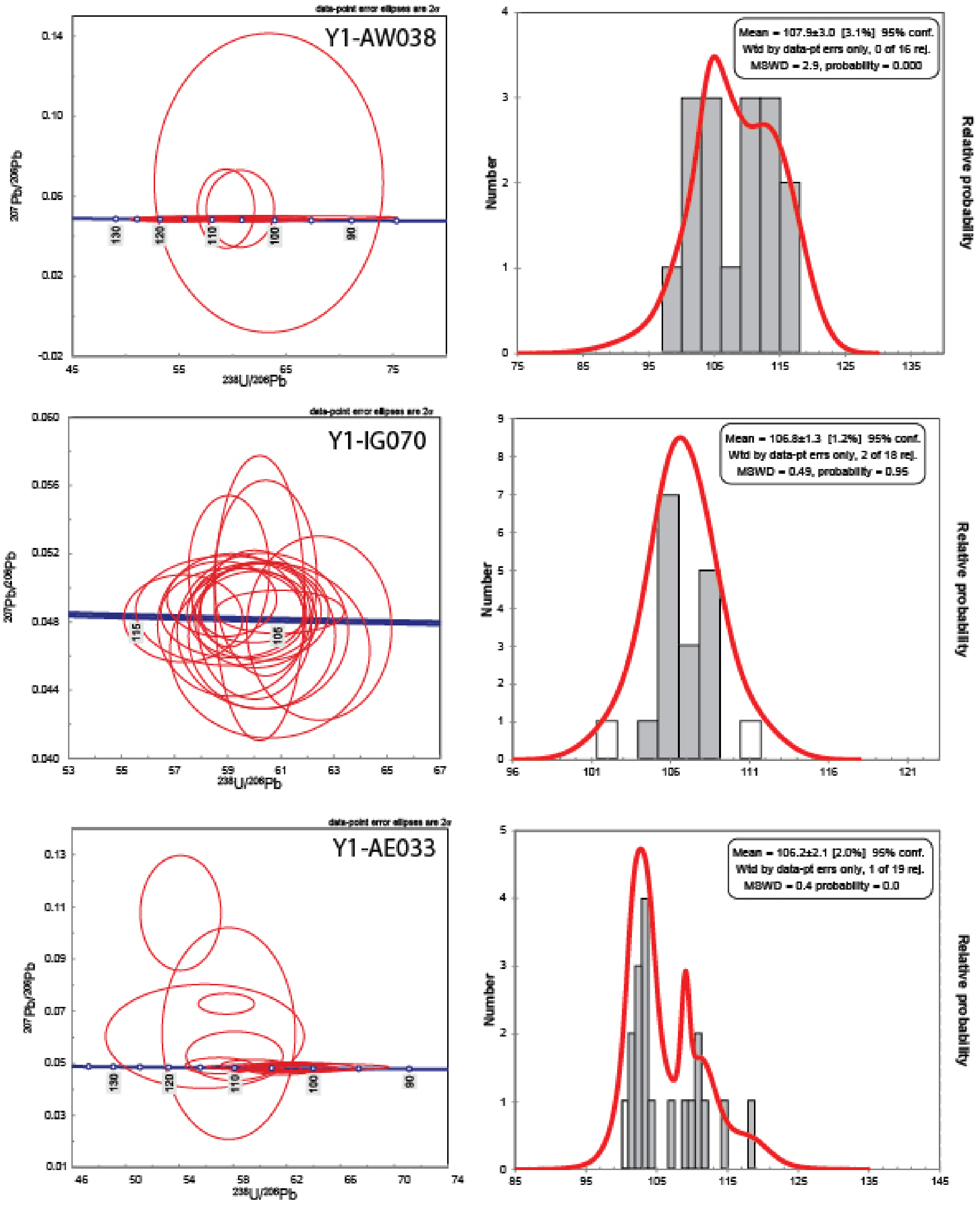

Figure E6: U–Pb Concordia plots and age histograms for Cretaceous granite samples

Cretaceous Granite

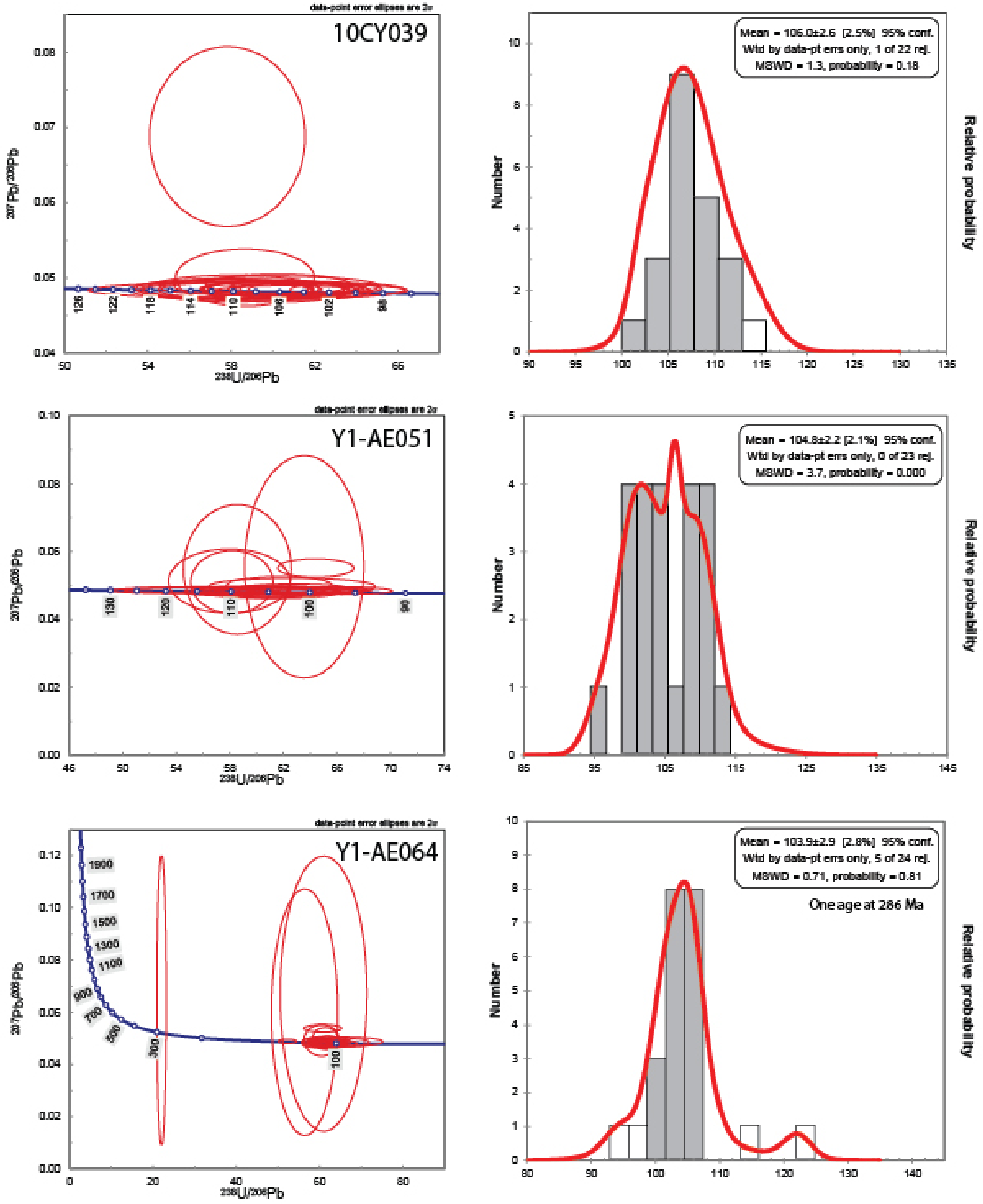

Figure E6: Continued

Cretaceous Granite

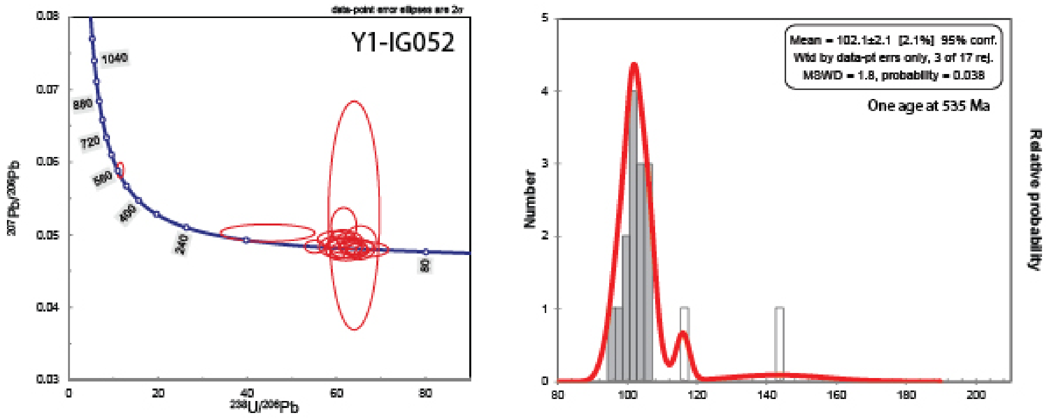

Figure E6: Continued

Cretaceous Microgranite

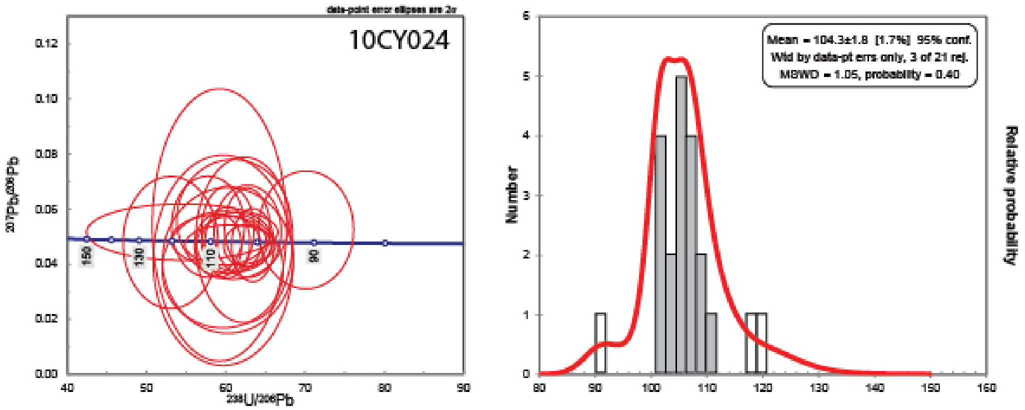

Figure E7: U–Pb Concordia plots and age histograms for Cretaceous microgranite samples

Appendix F: Standard Reproducibility

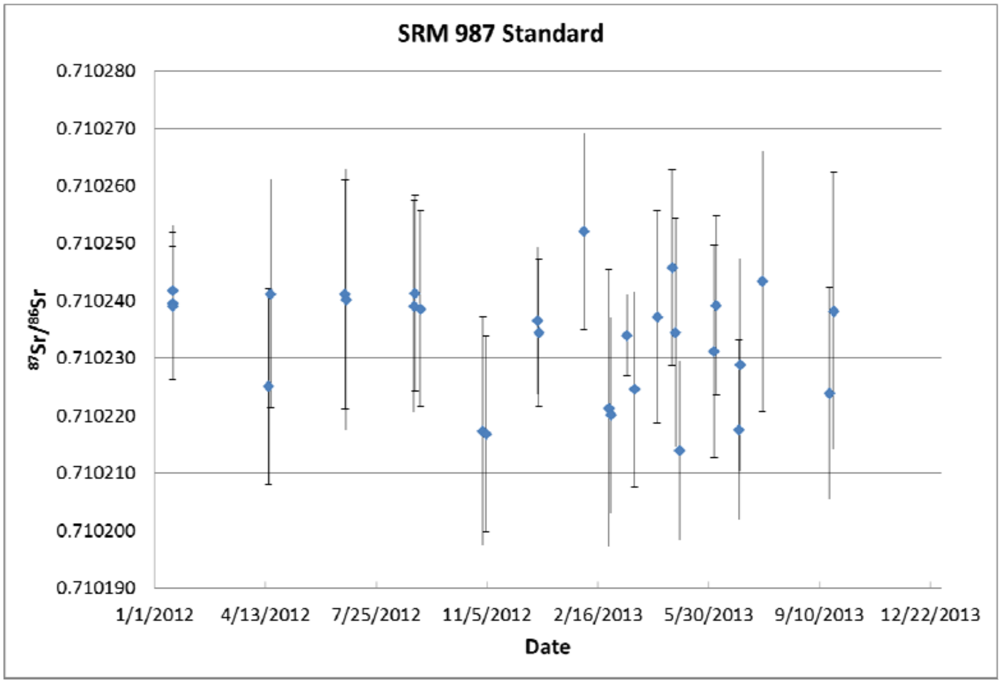

Figure F1: 390ng load of SRM 987 standard $^{87}Sr/^{86}Sr$ ratios over 12 month period. Error bars are 2σ analytical uncertainty.

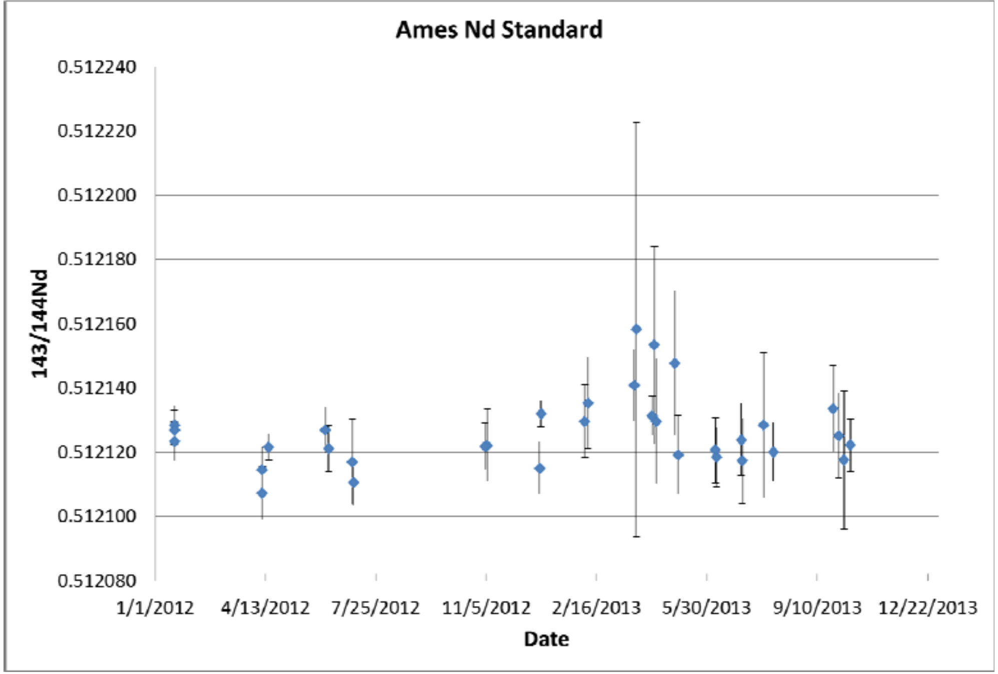

Figure F2: 1000ng load of Ames Nd standard $^{143}Nd/^{144}Nd$ ratios over a 12 month period. Error bars are 2σ analytical uncertainty.

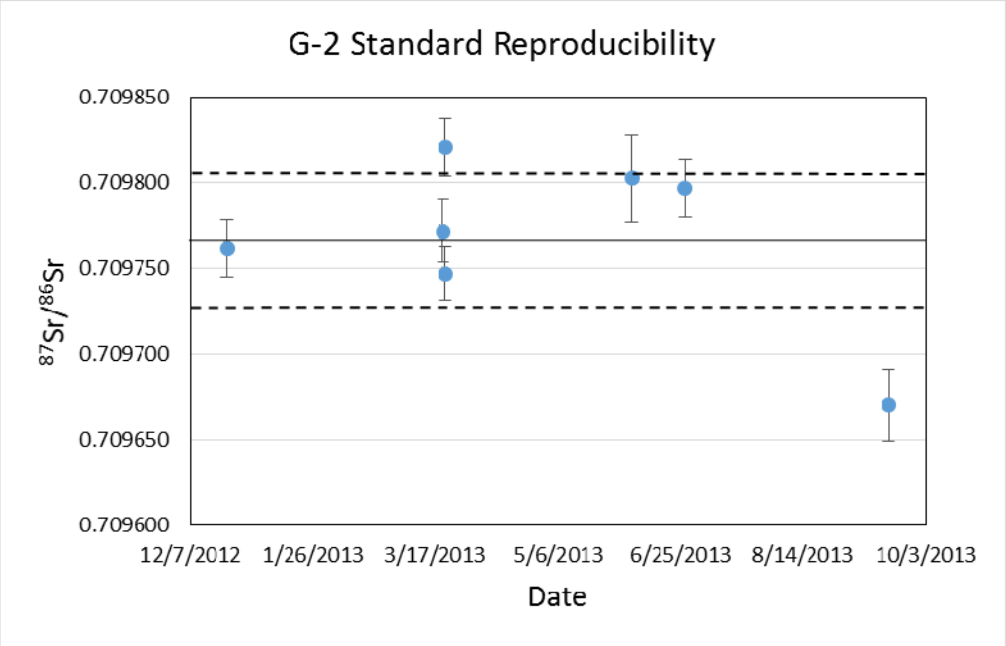

Figure F3: $^{87}Sr/^{86}Sr$ ratios of USGS standard G-2 over a period of 12 months. Solid black line is the average $^{87}Sr/^{86}Sr$ and the dashed black lines are 2 sigma standard error of the average.

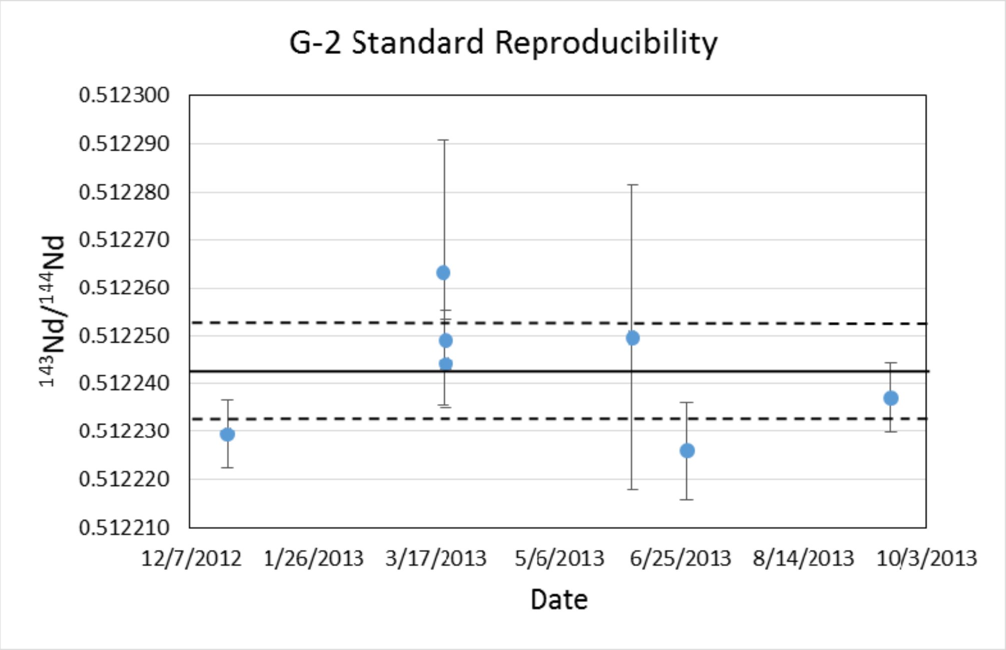

Figure F4: $^{143}Nd/^{144}Nd$ ratios of USGS standard G-2 over a period of 12 months. Solid black line is the average $^{143}Nd/^{144}Nd$ and the dashed black lines are 2 sigma standard error of the average.

Table F1: Sr–Nd isotope composition of USGS standard G-2

	Date	Rb (ppm)	2σ	Sr (ppm)	2σ	Rb/Sr	87Rb/86Rb	$^{87}Sr/^{86}Sr$	2σ	Sm (ppm)	2σ	Nd (ppm)	2σ	Sm/Nd	$^{147}Sm/^{144}Nd$	$^{143}Nd/^{144}Nd$	2σ	εNd
G-2		170[1]		478[1]		0.3556		0.709770[2]	0.000016[2]	7.2[1]		55[1]		0.1309		0.512228[2]	0.000006[2]	-8.0
G-2_1	12/22/2012	171.0		493.7		0.3463	1.002	0.709762	0.000017	7.102		52.19		0.1361	0.08226	0.512230	0.000007	-8.0
G-2_2	3/20/2013	174.2		496.2		0.3511	1.016	0.709772	0.000018	7.279		53.18		0.1369	0.08275	0.512263	0.000028	-7.3
G-2_3	3/21/2013	166.7		492.1		0.3387	0.9799	0.709821	0.000017	7.133		52.62		0.1356	0.08195	0.512249	0.000006	-7.6
G-2_4	3/21/2013	168.1		491.5		0.3419	0.9893	0.709747	0.000016	7.192		52.43		0.1372	0.08292	0.512244	0.000009	-7.7
G-2_5	6/5/2013	162.9		483.9		0.3367	0.9740	0.709803	0.000026	7.048		52.46		0.1344	0.08122	0.512250	0.000032	-7.6
G-2_6	6/27/2013	163.6		482.1		0.3394	0.9820	0.709797	0.000017	7.124		52.84		0.1348	0.08150	0.512226	0.000010	-8.0
G-2_7	9/18/2013	166.6		482.3		0.3455	0.9995	0.709670	0.000021	7.106		52.78		0.1346	0.08094	0.512237	0.000007	-7.8
Average	9/18/2013	167.6	3.0	488.8	4.4	0.3428	0.992	0.709767	0.000038	7.141	0.056	52.64	0.24	0.1356	0.08193	0.512243	0.000010	-7.7

[1] Gladney *et al.*, 1998

[2] Weis *et al*., 2006

Bibliography

Adams, C. J. (1986). Geochronological studies of the Swanson Formation of Marie Byrd Land, West Antarctica, and correlation with northern Victoria Land, East Antarctica, and South Island, New Zealand. *New Zealand Journal of Geology and Geophysics,* **29**, 345–358

Adams, C. J. (1987). Geochronology of granite terranes in the Ford Ranges, Marie Byrd Land, West Antarctica. *New Zealand Journal of Geology and Geophysics,* **30**, 54–72.

Adams, C. J. (2004). Rb–Sr age and strontium isotope characteristics of the Greenland Group, Buller Terrane, New Zealand, and correlations at the Eastern Gondwanaland margin. *New Zealand Journal of Geology and Geophysics* **47**, 189–200.

Adams, C. J., Pankhurst, R. J., Maas, R., and Millar, I. L. (2005). Nd and Sr isotopic signatures of metasedimentary rocks around the South Pacific margin and implications for their provenance. In Geological Society Special Publication (Geological Society of London), pp. 113-141.

Allibone, A.H., Turnbull, I.M., Tulloch, A.J., and Cooper, A.F. (2009). Plutonic rocks of the Median Batholith in southwest Fiordland, New Zealand: Field relations, geochemistry, and correlation. *New Zealand Journal of Geology and Geophysics*, **50**, 238–314.

Annen, C., Blundy, J.D., and Sparks, S.J. 2006. The Genesis of Intermediate and Silicic Magmas in Deep Crustal Hot Zones. *Journal of Petrology*, **47**, 505–539.

Ayres, M. and Harris, N. (1997). REE fractionation and Nd-isotope disequilibrium during crustal anatexis: constraints from Himalayan leucogranites. *Chemical Geology,* **139**, 249–269.

Barbero, L., Villaseca, C., Rogers, G., and Brown, P.E. (1995). Geochemical and isotopic disequilibrium in crustal melting: An insight from the anatectic granitoids from Toledo, Spain. *Journal of Geophysical Research*, **100**, 15745–15765.

Bea, F., Pereira, M.D., Corretgé, L.G., and Fershtater, G.B. (1994). Differentiation of strongly peraluminous, perphospherous granites – The Pedrobernardo pluton, central Spain. *Geochimica et Cosmochemica Acta*, **59**, 2609–2628.

Bea, F. (1996). Residence of REE, Y, Th and U in Granites and Crustal Protoliths; Implications for the Chemistry of Crustal Melts. *Journal of Petrology,* **37**, 521–552.

Borg, S.G., Stump, E., Chappell, B.W., McCulloch, M.T., Wyborn, D., Armstrong, R.L., and Holloway, J.R. (1987). Granitoids of northern Victoria Land, Antarctica: implications of chemical and isotopic variations to regional crustal structure and tectonics. American *Journal of Science*, **287**, 127–169.

Boyd, F.R., and Mertzman, S.A. (1987). Composition of structure of the Kaapvaal lithosphere, southern Africa: In: Magmatic Processes - Physicochemical Principles, B.O. Mysen, Ed., The Geochemical Society, Special Publication #1, pp. 13–24 .

Bradshaw, J.D., Andrews, P.B. and Field, B.D. (1983). Swanson Formation and related rocks of Marie Byrd Land and a comparison of with the Robertson Bay Group of Northern Victoria Land. In: Antarctic Earth Science (eds Oliver, R. L., James, P. R. and Jago, J. B.), pp. 274–279, Cambridge University Press, Cambridge.

Brown, M. (1994). The generation, segregation, ascent and emplacement of granite magma: the migmatite-to-crustally-derived granite connection in thickened orogens. *Earth Science Reviews*, **36,** 83–130.

Brown, M., Averkin, Y.A., McLellan, E.L., and Sawyer, E.W. (1995). Melt segregation in migmatites. *Journal of Geophysical Research*, **100**, 15655–15679

Brown, M. (2001). Crustal Melting and Granite Magmatism: Key Issues. Physics and Chemistry of the Earth Part A Solid Earth and Geodesy, **26**, 201–212

Brown, M. (2007). Crustal melting and melt extraction, ascent and emplacement in orogens: mechanisms and consequences. *Journal of the Geological Society*, **164**, 709-730.

Clemens, J.D., Stevens, G., and Farina, F. (2011). The enigmatic source of I-type granites: The peritectic connexion. *Lithos,* **126**, 174–181

Clemens, J.D. and Stevens G. (2012). What controls chemical variation in granitic magmas? *Lithos* **134–135**, 317–329.

Collins, W.J. (1996). Lachlan fold belt granitoids: products of three-component mixing. *Transactions of the Royal Society of Edinburg: Earth Sciences,* **87,** 171–181

Corfu, F., Hanchar, J.M., Hoskin P.W.O, and Kinney, P. (2003). Atlas of Zircon Textures. *Reviews in Mineralogy and Geochemistry*, **53**, 471–495.

Davy, B.W. and Wood, R.A. (1994). Gravity and magnetic modelling of the Hikurangi Plateau. *Marine Geology*, **118**, 139–151.

Davy, B.W., Hoernle, K., and Werner, R. (2008) Hikurangi Plateau: crustal structure, rifted formation, and Gondwana subduction history. *Geochemistry Geophysics Geosystems,* **9**, Q07004.

Dalziel, I.W.D. and Elliot, D.H. (1982). West Antarctica: problem child of Gondwanaland. *Tectonics*, **1**, 3–19.

Farina, F. and Stevens, G. (2011). Source controlled 87Sr/86Sr isotope variability in granitic magmas: The inevitable consequence of mineral-scale isotopic disequilibrium in the protolith. *Lithos,* **122**, 189–200.

Gehrels, G. E., Valencia, V. A., and Ruiz, J. (2008). Enhanced precision, accuracy, efficiency, and spatial resolution of U-Pb ages by laser ablation–multicollector–inductively coupled plasma–mass spectrometry. *Geochemistry Geophysics Geosystems*, **9**, 1–13.

Gladney, E.S., Jones, E.A., Nickell, E.J., and Roelandts, I. (1992) Compilation of elemental concentration data for USGS AGV-1, GSP-1 and G-2. *Geostandards Newsletter*, **16**, 111–300.

Harris, N. and Ayres, M. (1998). The implications of Sr-isotope disequilibrium for rates of prograde metamorphism and melt extraction in anatectic terrains. In: Geological Society Special Publication (Geological Society of London), pp. 171–182.

Harrison, T.M. and Watson, B.E. (1984). The behavior of apatite during crustal anatexis: Equilibrium and kinetic considerations. *Geochimica et Cosmochimica Acta,* **48**, 1467–1477.

Hirose, K. (1997). Partial melt compositions of carbonated peridotite at 3 GPa and role of CO2 in alkali-basalt magma generation. *Geophysical Research Letters*, **24**, 2837–2840.

Hogan, J.P. and Sinha, A.K. (1991). The effect of accessory minerals on the redistribution of lead isotopes during crustal anatexis: a model. *Geochimica et Cosmochimica Acta*, **55**, 335–348.

Ireland, T.R., Flöttmann, Fanning, C.M., Gibson, G.M., and Preiss, W.V. (1998). Development of the early Paleozoic Pacific margin of Gondwana from detrital-zircon ages across the Delamerian orogeny. *Geology*, **26**, 243–246.

Jaques, A. L., and Green, D. H. (1980). Anhydrous melting of peridotite at 0-15 kb pressure and the genesis of tholeiitic basalts. *Contributions to Mineralogy and Petrology*, **73**, 287–310.

Jung, S., Hoernes, S., and Mezger. (2000). Geochronology and petrogenesis of Pan-African, syn-tectonic, S-type and post-tectonic A-type granite (Namibia): products of partial melting of crustal sources, fractional crystallization and wall rock entrainment. *Lithos,* **50**, 259–287.

Kemp, A., Hawkesworth, C.J., Foster, G.L., Patreson, B.A., Hergt, J.M., Gray, C.M., Whitehouse, M.J. (2007). Magmatic and crustal differentiation history of granitic rocks from HF–O isotopes in zircon. *Science*, **315,** 980–983.

Knesel, K.M. and Davidson, J.P. (1996). Isotope disequilibrium during melting of granite and implications for crustal contamination of magmas. *Geology*, **24**, 243–246.

Koester, E., Pawley, A.R., Fernandes, L.A.D., Porcher, C.C., and Soiani, E. (2002). Experimental melting of cordieite gneiss and the petrogenesis of syntranscurrent peraluminous granites in southern Brazil. *Journal of Petrology*, **43**, 1595–1616.

Korhonen, F. J., Saito, S., Brown, M. and Siddoway, C. S. (2010a). Modeling multiple melt loss events in the evolution of an active continental margin. *Lithos*, **116**, 230–248.

Korhonen, F. J., Saito, S., Brown, M., Siddoway, C. S. and Day, J. M. D. (2010b). Multiple Generations of Granite in the Fosdick Mountains, Marie Byrd Land, West Antarctica: Implications for Polyphase Intracrustal Differentiation in a Continental Margin Setting. *Journal of Petrology*, **51**, 627–670.

Korhonen, F. J., Brown, M., Grove, M., Siddoway, C. S., Baxter, E. F., and Inglis, J. D. (2012). Separating metamorphic events in the Fosdick migmatite–granite complex, West Antarctica. *Journal of Metamorphic Geology*, **30**, 165-192.

LeMasurier, W.E.A. and Landis, C.A. (1996). Mantle-plume activity recorded by low-relief erosion surfaces in West Antarctica and New Zealand. *Geological Society of America Bulletin*, **108**, 1450–1466.

Ludwig, K. R. (2010). Isoplot/ExVersion 4.1: a GeochronologicalToolkit for Microsoft Excel. Berkeley Geochronology Center Special Publication 1a, 46 p.

Lugmair, G.W. and Marti, K. (1978). Lunar 143Nd/144Nd: differential evolution of the lunar crust and mantle. *Earth Planetary Science Letters*, **39**, 349–357.

Luyendyk, B.P. (1995). Hypothesis for Cretaceous rifting of east Gondwana caused by subducted slab capture. *Geology*, **23**, 373–376.

McDonough, W.F. and Sun, S-s. (1995). The composition of the Earth. *Chemical Geology*, **120**, 223–254.

McFadden, R.R., Siddoway, C.S, Teyssier, C., and Fanning, C.M. (2010a). Cretaceous oblique extensional deformation and magma accumulation in the Fosdick Mountains migmatite-cored gneiss dome, West Antarctica. *Tectonics*, **29**, TC4022.

McFadden. R.R., Teyssier, C., Siddoway, C.S., Whitney, D.L., and Fanning, C.M. (2010b). Oblique dilation, melt transfer, and gneiss dome emplacement. *Geology,* **38**, 375–378.

Mortimer, N., Koernle, K., Hauff, F., Palin, J.M., Dunlap, W.J., Werner, R., and Faure, K. (2006). New constraints on the age and evolution of the Wishbone Ridge, southwest Pacific Cretaceous microplates, and Zealandia–West Antarctica breakup. *Geology*, **34**, 185–188.

Muir, R.J., Ireland, T.R., Weaver, S.D., and Bradshaw, J.D. (1996). Ion microprobe dating of Paleozoic granitoids: Devonian magmatism in New Zealand and correlations with Australia and Antarctica. *Chemical Geology*, **127**, 191–210.

Mukasa, S.B. and Dalziel, I.W.D. (2000). Marie Byrd Land, West Antarctica: Evolution of Gondwana's Pacific margin constrained by zircon U-Pb geochronology and feldspar common-Pb isotopic compositions. *GSA Bulletin*, **112**, 611–627.

O'Hara, M. J., Fry, N., and Prichard, H. M. (2001). Minor Phases as Carriers of Trace Elements in Non-Modal Crystal-Liquid Separation Processes II: Illustrations and Bearing on Behavior of REE, U, Th and the PGE in Igneous Processes. *Journal of Petrology*, **42**, 1887–1910.

Pankhurst, R.J., Weaver, S.D., Bradshaw, J.D., Storey, B.C. and Ireland, T.R. (1998). Geochronology and geochemistry of pre-Jurassic superterranes in Marie Byrd Land, Antarctica. *Journal of Geophysical Research*, **103**, 2529–2547.

Patiño Douce, A. E., and Harris, N. B. W. (1998). Experimental Constraints on Himalayan Anatexis. *Journal of Petrology*, **39**, 689–710.

Pearce, J.A. and Parkinson, I.J. (1993) Trace element models for mantle melting: application to volcanic arc petrogenesis. In Geological Society of London, Special Publications, **76**, 373–403.

Rapp, R.P. and Watson, E.B. (1986). Monazite solubility and dissolution kinetics: implications for the thorium and light rare earth chemistry of felsic magmas. *Contributions to Mineralogy and Petrology*, **94**. 304–316.

Rey, P.F. and Müller, R.D. (2010). Fragmentation of active continental plate margins owing to the buoyancy of the mantle wedge. *Nature Geoscience*, **3**, 257–261.

Richard, S.M., Smith, C.H., Kimbrough, D.L., Fitzgerald, P.G., Luyendyk, B.P. and McWilliams, M.O. (1994). Cooling history of the northern Ford Ranges, Marie Byrd Land, West Antarctica. *Tectonics,* **13**, 837–857.

Rotenberg, E., Davis, D.W., Amelin, Y., Gosh, S., and Bergquist, B.A. (2012). Determination of the decay-constant of ^{87}Rb by laboratory accumulation of ^{87}Sr. *Geochimica et Cosmochimica Acta*, **85**, 41–57.

Rudnick, R. L., and Gao, S. (2003). Composition of the Continental Crust. (H. D. Holland and K. K. Turekian, Eds.)Treatise on Geochemistry, 1(1), 1-64.

Saito, S., Brown, M., Korhonen, F.J., McFadden, R.R., and Siddoway, C.S. (2013). Petrogenesis of Cretaceous mafic intrusive rocks, Fosdick Mountains, West Antarctica: Melting of the sub-continental arc mantle along the Gondwana margin. *Gondwana Research*, **23**, 1567–1580.

Sambridge, M. S., and Compston, W. (1994). Mixture modeling of multi-component data sets with application to ion-probe zircon ages. *Earth and Planetary Science Letters*, **128**, 373–390.

Sawka, N.W. (1988). REE and trace element variations in accessory minerals and hornblende from the strongly zoned McMurry Meadows Pluton, California. *Transactions of the Royal Society of Edinburgh: Earth Sciences*, **79**, 157–168.

Sawyer, E.W. (1998) Formation and evolution of granite magmas during crustal reworking: the significance of diatexites. *Journal of Petrology*, **39,** 1147–1167.

Sawyer, E.W., Cesare, B., and Brown, M. 2011. When the Continental Crust Melts. *Elements*, **7**, 229–234

Siddoway, C.S. and Fanning, C.M. (2009). Paleozoic tectonism on the East Gondwana margin: Evidence from SHRIMP U–Pb zircon geochronology of a migmatite–granite complex in West Antarctica. *Tectonophysics*, **477**, 262–277.

Siddoway, C.S., Richard, S.M., Fanning, C.M., and Luyendyk, B.P. (2004). Origin and emplacement of a middle Cretaceous gneiss dome, Fosdick Mountains, West Antarctica, in Whitney, D.L., et al., eds., Gneiss domes in orogeny*:* *Geological Society of America Special Paper*, **380**, 267–294

Siddoway, C.S., Sass, L.C., III, and Esser, R. (2005). Kinematic history of Marie Byrd Land terrane, West Antarctica: Direct evidence from Cretaceous mafic dykes, in Vaughan, A.P.M., et al., eds., Terrane processes at the margin of Gondwana: *Geological Society of London Special Publication*, **246**, 417–438.

Skjerlie, K.P., Patiño Douce, A.E., and Johnston, A.D. (1993). Fluid absent melting of a layered crustal protolith: implications for the generation of anatectic granites. *Contributions to Mineralogy and Petrology,* **114**, 365–378.

Solar, G.S. and Brown, M. (2001). Petrogenesis of migmatites in Maine, USA: Possible source of peraluminous leucogranite in plutons? *Journal of Petrology*, **42**, 789–823.

Storey, B.C., Leat, P.T., Weaver, S.D., Pankhurst, J.D., and Kelley, S. (1999). Mantle plumes and Antarctic–New Zealand rifting: Evidence from mid-Cretaceous mafic dykes. *Journal of the Geological Society of London*, **156**, 659–671.

Tulloch, A.J., Beggs, M., Kula, J., Spell, T., and Mortimer, N. (2006). Cordillera Zealandia, the Sisters Shear Zone and their influence on the early development of the Great South Basin, paper presented at New Zealand Petroleum Conference, Wellington.

Tulloch, A.J., Ramezani, J., Kimbrough, D.L., Faure, K. and Allibone, A.H. (2009). U–Pb geochronology of mid-Paleozoic plutonism in western New Zealand:

Implications for S-type granite generation and growth of the east Gondwana margin. *Geological Society of America Bulletin*, **121**, 1236–1261.

Vailleros, A., Buick, I.S., and Stevens, G. (2011). Isotopic variations in S-type granites: an inheritance from a heterogeneous source? *Contributions to Mineralogy and Petrology*, **163**, 243–257.

Watt, G.R., Burns, I.M., and Graham, G.A. (1996). Chemical characteristics of migmatites: accessory phase distribution and chemical evidence for fast melt segregation rates. *Contributions to Mineralogy and Petrology*, **125**, 100–111.

Watt, G.R. and Harley, S.L. (1993) Accessory phase controls on the geochemistry of crustal melts and restites produced during water-undersaturated partial melting. *Contributions to Mineralogy and Petrology*, **114**, 550–566.

Weaver, S.D., Bradshaw, J.D. and Adam, C.J. (1991). Granitoids of the Ford Ranges, Marie Byrd, Land, Antarctica. In: Geological Evolution of Antarctica (eds Thompson, M.R.A., Grame, J.A. and Thompson, J.W.), pp. 345–351, Cambridge University Press, Cambridge.

Weaver, S. D., Adams, C. J., Pankhurst, R. J. & Gibson, I. L. (1992). Granites of Edward VII Peninsula, Marie Byrd Land: anorogenic magmatism related to Antarctic–New Zealand rifting. *Transactions of the Royal Society of Edinburgh: Earth Sciences*, **83**, 281–290.

Weaver, S.D., Storey, B.C., Pankhurst, R.J., Mukasa S.B., DiVenere, V.J., and Bradshaw, J.D. (1994). Antarctica-New Zealand rifting and Marie Byrd Land lithospheric magmatism linked to ridge subduction and mantle plume activity. *Geology,* **22**, 811–814.

Weis, D., Kieffer, B., Maerschalk, C., Barling, J., de Jong, J., Williams, G.A., Hanano, D., Pretorius, W., Mattielli, N., Scoates, J.S., Goolaerts, A., Friedman, R.M., and Mahoney, J.B. (2006). High-precision isotopic characterization of USGS reference materials by TIMS and MC-ICP-MS. *Geochemistry Geophysics Geosystems*, **7**, Q08006

Yakymchuk, C., Siddoway, C.S., Fanning, C.M., McFadden, R., Korhonen F.J., and Brown, M. (2013a). Anatectic reworking and differentiation of continental crust along the active margin of Gondwana: a zircon Hf–O perspective from West Antarctica. *Geological Society, London, Special Publications*, **383**.

Yakymchuk, C., Brown, M., Ivanic, T.J.m and Korhonen F.J. (2013b). Leucosome distribution in migmatitic paragneisses and orthogneisses: a record of self-organized melt migration and entrapment in a heterogeneous partially molten crust. *Tectonophysics*, **603**, 136–154.

Yang, J.H., Wu, F.Y., Wilde, S.A., Xie, L.W., Yang, Y.H., and Liu, X.I. (2007). Tracing magma mixing in granite genesis: in situ U–Pb dating and Hf-isotope analysis of zircons. *Contributions to Mineralogy and Petrology,* **153**, 177-190.

Zeng, L., Asimow, P.D., and Saleeby, J.B. (2005a). Coupling of anatectic reactions and dissolution of accessory phases and the Sr and Nd isotope systematics of anatectic melts from a metasedimentary source. *Geochimica et Cosmochimica Acta*, **69**, 3671–3682.

Zeng, L., Saleeby, J. B., and Asimow, P. (2005b). Nd isotope disequilibrium during crustal anatexis: A record from the Goat Ranch migmatite complex, southern Sierra Nevada batholith, California. *Geology*, **33**, 53–56.

Zeng, L., Saleeby, J. B., and Ducea, M. (2005c). Geochemical characteristics of crustal anatexis during the formation of migmatite at the Southern Sierra Nevada, California. *Contributions to Mineralogy and Petrology*, **150**, 386–402.